Objects interacting with a solidification front

Sidhanth Tyagi

To cite this version:

Sidhanth Tyagi. Objects interacting with a solidification front. Chemical Physics [physics.chem-ph]. Université Paris sciences et lettres, 2020. English. NNT : 2020UPSLS025 . tel-03934732

HAL Id: tel-03934732
https://pastel.hal.science/tel-03934732v1

Submitted on 11 Jan 2023

PSL
UNIVERSITÉ PARIS

THÈSE DE DOCTORAT
DE L'UNIVERSITÉ PSL

Préparée à Ecole Supérieure de Physique et de Chimie Industrielles
de la Ville de Paris et Saint-Gobain Research Provence

Objects interacting with a solidification front

Objets en interaction avec un front de solidification

Soutenue par
Sidhanth TYAGI
Le 12 Octobre 2020

École doctorale n°397
Physique et chimie des matériaux

Spécialité
Physico-chimie

Confidentielle jusqu'au 01-01-2023

Composition du jury :

Charles-André GANDIN DR CNRS, MINES ParisTech	*Président du Jury*
Dirk AARTS Professeur, University of Oxford	*Rapporteur*
Nathalie MANGELINCK-NOËL DR CNRS, IM2NP AMU	*Rapportrice*
Robert STYLE Chef de groupe, ETH Zurich	*Examinateur*
Cécile MONTEUX DR CNRS, ESPCI Paris	*Directrice de thèse*
Sylvain DEVILLE DR CNRS, Université de Lyon	*Directeur de thèse*
Caroline TARDIVAT Directrice LSFC, Saint-Gobain	*Invitée*

ESPCI PARIS | PSL

Acknowledgements

This thesis would not have been possible without the support and assistance of numerous people.

First and foremost I would like to thank my supervisors, Sylvain Deville and Cécile Monteux, whose expertise and guidance were invaluable in formulating the research questions and methodology. Your insightful and constructive feedback pushed me to sharpen my thinking and brought my work to a higher level. The different experiences I had over the past three years inculcated a sense of critical thinking and I am grateful to my supervisors for giving me this opportunity.

I would like to acknowledge Saint-Gobain for funding this wonderful collaboration. I would particularly like to single out my manager at Saint-Gobain Research Provence, Caroline Tardivat. Caroline, I want to thank you for your patient support and for all of the resources I was given to further my research. I highly appreciated attending the workshops and conferences which gave me a broader perspective of my research.

I would also like to thank my colleagues at Saint-Gobain NorPro, Patrick Nguyen and Nicole Rives, for introducing me to the domain of research and supporting me for this PhD position. You provided me with the opportunity that I needed to choose the right direction and I admire your positive and generous attitude.

In addition, I would like to thank Helene Huynh, for developing the preliminary experiments on freezing of foams. Your perseverance and adaptability made the internship a delightful affair. At ESPCI Paris, I would like to thank Mathilde Reyssat, for her initial aid on testing the microfluidic setup. At ILM Lyon, I would sincerely like to thank Cécile, Christophe, and Rémy, for their guidance and consistent help on the diffusiophoresis experiments. At LSFC, I want to extend my gratitude and thankfulness to Helena, Stéphane, Daniel, and Michaela, for their scientific and technical guidance.

I take this opportunity to also thank all the jury members for graciously accepting to review this dissertation. Your valuable comments, discussions, and interpretation helped me in improving the contents of my research.

I thank Mangesh, Hassan, and Maxime, for the squash, badminton, volleyball, fitbox, skiing and whatnot sporting as well as fun activities we performed together. Débora and Nanju for being always there to discuss and support me whenever I needed motivation. Some other colleagues and friends that I would like to thank are Laura (and her pool), Michael (and the hikes), Pierre-Alexis, Corinne, Théo, Benjamin, Julie, Paolo, Kevin, Quentin, Lucas, Daniel, Baptiste, Alexey, Zane, Félix, Dymtro, Basic-Fit, and others who I might have forgotten. I could not have completed this thesis without your support, stimulating ideas (aka jokes), as well as delightful distractions to rest my mind outside of my research.

Finally, I would like to thank my family for their encouragement, wise counsel, and sympathetic ear. You are always there for me.

Contents

Introduction

Materials form an integral part of the human society. The importance of materials is such that the human civilization is often divided into ages according to the materials that dominate in the society. The exploration and evolution of materials by mankind started with the Stone Age, and progressed with the Bronze and Iron Age. Today, we have entered into the revolutionary era of *engineered materials*, where plastics and silicon have prevailed in the past two decades. As the world population continues to rise, the demand for novel and more extravagant materials has become a hallmark of our modern industrialized society. The global expansion, therefore, puts an ever increasing demand on the production of materials with improved physical, chemical, and mechanical properties.

The present approach to material science and engineering is based on the recognition that a material's property (intrinsic or extrinsic) depends on its complex structure. To understand a material, it is therefore necessary to know the material structure at different length scales, such as the atomic-, microscopic-, or macroscopic-scale. A control of the material structure at these diverse scales, where the fabrication route or processing technique plays a major role, aides in the construction of novel hybrid materials. The use of ice-templating or freeze-casting for the design of *engineered materials* has been a topic of interest recently. The process has seen a surge of interest in the past decades, and represents a unique phenomenon at the intersection of several domains extending beyond the realms of materials science. The basic idea of freeze-casting or ice-templating is the solidification of a suspension to create architectured porosity from the directionally growing solid crystals. The process results in the formation of a green body (before sintering) having a macro-porous structure owing to the sublimation of the solvent crystals after their solidification. Therefore, in the interest of improving properties of freeze-cast materials, an understanding of the suspension solidification phenomenon is very essential.

Solidification, also known as freezing, is the process where a liquid melt undergoes phase transition to form a solid phase. Historically, solidification was used extensively for metal casting and welding processes, but in this modern age it applies to commercially manufactured polymers, ceramics, and even natural biological systems. Great strides have been made in understanding many aspects of solidification. Theoretical models have been developed to simulate actual solid crystal structures, and experiments have been designed and carried out to shed light on the crystal growth. However, a fundamental question still partly unanswered in the solidification of suspensions or alloys is the development of the microstructure in the presence of secondary objects, such as particles or bubbles, in the melt. This phenomenon is also at the core of ice-templating, where ceramic, metallic, or polymer particles dispersed in the solution interact with a solidification front. This is important as the segregation and redistribution of the suspended particles by the advancing front determines the material microstructure. Hence, our present study represents a continuation of the work initiated in LSFC (Saint-Gobain Research Provence), on ice-templating, freezing of colloids, and new architectured materials.

The interaction of foreign objects suspended in a liquid melt with an approaching solid-liquid front is of special interest in nature and in engineering sciences. This phenomenon was initially investigated by geologists and civil engineers studying the interaction of soil particles with an ice-water interface to explain the formation of ice-lenses and frost-heaving. Presently, this subject garners interest in the research of cryopreservation of biological cells, food preservation, ice growth, metallurgy, single-crystal growth, and freeze-casting. The process is hence encountered in a plethora of situations with significant applications in materials science, physics, or biology. The objects (soft or hard) can have diverse outcomes owing to their confrontation with the solidifying front. The front can engulf the object, trapping it into the growing crystal, or the front can repel the object, pushing it ahead of itself.

The presence of foreign objects can have a strong influence on the properties of the solidified crystal. In particular, the spatial distribution of the objects, among other parameters, determines the structural and functional properties of the material. It is desired, for example, that the reinforcing second-phase ceramic particles be homogeneously distributed in metal-matrix composites. This can be achieved by an instantaneous engulfment of the objects by the solid-liquid interface. In other words, the objects should be oblivious to the presence of an approaching front. In contrast, the fabrication of porous materials by freeze-casting relies on the complete segregation or clustering of particles by the solidification front. Here, particles must be rejected by the growing crystal and collected between the arms (dendrites) of the solidification front. In single-crystal growth, the rejection of dissolved impurities (gases) and second-phase particles is critical for obtaining pure materials. Therefore, the solidification front should act as a purifying interface (for a partition ratio less than 1), and segregate the impurities at the crystal periphery to eliminate them easily by polishing. Thus, in all of these domains, control of the microstructure resulting from solidification is essential.

The objective of our study is to perform directional solidification experiments to comprehend the mechanisms responsible for the development of a solidification microstructure in the presence of foreign objects. This works focuses on the role of solute on these phenomena, which has been largely underestimated so far. We analyse the interaction of spherical soft objects (droplets and bubbles) and rigid particles (polymers, ceramics, and metals) with an advancing ice-water interface. Our custom cryo-confocal microscopy setup enables a rapid $2D$ and $3D$ imaging of the growth of ice crystals, the liquid phase, and the dynamics of objects encountering the solidification front. We characterise and report on the role of solutes while experimentally depicting the evolution of the local solute segregation. In particular, we analyse the impact of solute concentration and their influence on the interface geometry, object dynamics, and the solidified microstructure. We further analyse the fundamental mechanisms of interactions when soft deformable objects are hit by a solidification front. We progress towards more realistic systems by employing a high volume fraction of objects as compared to the isolated systems. Finally, we compare our experimental observations with the past theoretical models to elucidate the different features and propose mechanisms for the contrasting phenomena.

Chapter 1

State of the art

1.1 Introduction

The interaction of objects with a moving solid-liquid interface has been studied both experimentally and theoretically. The first systematic measurements for particle engulfment by an ice-water interface were conducted by Corte [1]. He used particles of different size and shapes to study the influence of an increasing growth rate on the particle capture. The observation of particle pushing by a growing crystal instigated studies to deduce a critical velocity (V_c), the growth rate below which a particle is pushed ($V_{sl} < V_c$) and above which the particle is engulfed ($V_{sl} > V_c$) by the growing solid [2]. The theoretical derivation of the critical velocity (V_c) has been treated by numerous studies and the approaches differ mainly in the approximations used. The studies mainly deal with smooth, spherical, and rigid particle of radius R moving ahead of a planar front at a distance of $d << R$ in *steady-state* directional solidification. A schematic drawing representing an object in the vicinity of a solid-liquid interface with the related parameters is shown in Fig.1.1.

In this thesis, an emphasis is placed on experimental studies. A detailed background is, however, presented so that the important principles governing the interaction of objects with solidification fronts can be clearly established. I first try to highlight some of the most important theoretical models, which allows us to further understand the isolated object behaviour in the vicinity of a solid-liquid interface. A comprehensive review of the governing equations, the advantages, and the limitations of each predictive model invoked is presented. I discuss the essential mechanisms and parameters influencing the object-front interaction

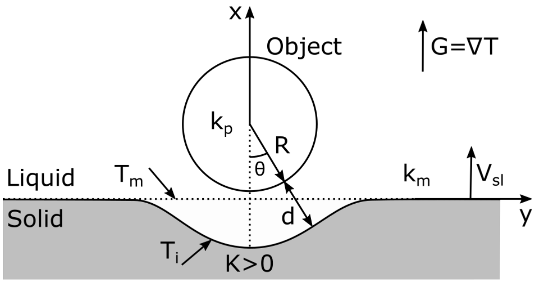

Figure 1.1: Object interacting with a moving solidification front: principles. Model sketch, where d is the particle-front gap, $G = \nabla T$ is the temperature gradient, κ is the interfacial front curvature (here > 0 for concave geometry), k_p, k_m are the thermal conductivity of the particle and melt respectively, R is the object radius, T_m is the absolute melting temperature, T_i is the solid-liquid interfacial temperature, and V_{sl} is the solidification velocity.

during directional solidification. The impact and role of solutes (or impurities) on modifying the interactions is also explored. I further analyse the experimental techniques employed previously in conducting similar directional solidification studies, and discuss the correlations of the experimentally observed features to the predicted theoretical behaviour. Finally, the complex nature of realistic systems having multiple objects is compared to the ideal isolated object-front interactions.

1.2 Theoretical models

The prediction of a critical velocity in a given system depends on the nature and magnitude of various forces acting on the particle while it is being pushed by the solidification front. At *steady-state* repulsion, the sum of these forces must be zero, and the critical velocity will be reached when the forces are no longer in equilibrium. Uhlmann *et al.* [3] were the first to present a derivation of the critical velocity in qualitative agreement with their experimental data. They extended a thermodynamic argument, involving the different surface energies to explain the stability of liquid films, to the present problem of objects interacting with a solidification front. In the case of particle engulfment, the two existing interfaces (particle-liquid and solid-liquid) should be replaced by a single interface (solid-particle). Hence, the thermodynamic criterion for a particle to be engulfed spontaneously by the solidification front is given by

$$\Delta\sigma_0 = \sigma_{sp} - (\sigma_{pl} + \sigma_{sl}) < 0 \tag{1.1}$$

where σ_{sp}, σ_{pl}, and σ_{sl} are the interfacial free energies associated with the solid-particle, particle-liquid, and solid-liquid interface respectively. In other words, the particle will be engulfed or pushed depending on the configuration with the lowest energy (see Fig.1.2).

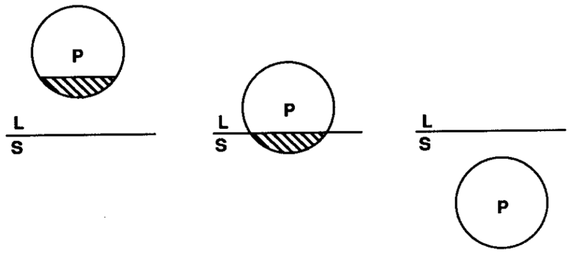

$\sigma_1 = \sigma_{SL} + \sigma_{LP}$ (*a*)

$\sigma_2 = \sigma_{SP}$ (*b*)

$\sigma_3 = \sigma_{SP} + \sigma_{SL}$ (*c*)

Figure 1.2: Change in interfacial energy when a particle interacts with a solidification front, adapted from [4].

This thermodynamic approach was used extensively by Omenyi and Neumann [5, 6]. However, the approach had two significant drawbacks. First, the experimental measurements of the σ_{sp}, solid-particle interfacial energy, were difficult and the theoretical estimations presented various discrepancies. Second, the approach could only be used to make qualitative predictions of engulfment or rejection at infinitely small growth rates ($< 1\ \mu m \cdot s^{-1}$) [7].

1.2.1 Repulsive interfacial force

Uhlmann *et al.* [3] refined this thermodynamic criterion by assuming that the change in interfacial energy ($\Delta\sigma$) varied with the distance (d) between the particle and the solidification front as a power law given by

$$\Delta\sigma = \Delta\sigma_0 \left(\frac{d_0}{d}\right)^n \tag{1.2}$$

where $\Delta\sigma$ is the interfacial energy at distance d, $\Delta\sigma_0$ is as given in Eq.1.1, d_0 is the minimum possible separation distance between the particle and the solid (corresponding to contact) and equal to a few molecular diameters, and n is a positive number chosen equal to 4 or 5 (see Fig.1.3).

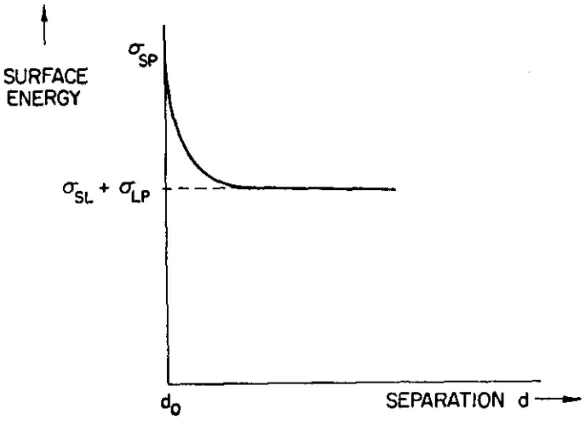

Figure 1.3: Interfacial energy varying with the distance (d) between the particle and the solidification front, adapted from [3].

This change in interfacial energy was assumed as the driving force for the flow of liquid material (melt) in the particle-front gap. The diffusion of liquid was deemed necessary to maintain a stable liquid film, thereby preventing particle-solid contact and hence, particle engulfment. Hence, the repulsive force preventing the particle engulfment arises from the need to maintain a stable liquid film, which avoids the contact between a particle and an approaching solidification front. An expression for the repulsive force due to interfacial energy can then be determined as [3, 8]

$$F_\sigma = 2\pi R \Delta\sigma_0 \left(\frac{d_0}{d}\right)^n \tag{1.3}$$

1.2.2 Attractive viscous force

The attractive force, favoring engulfment of the particle, arises from the viscous drag due to fluid flow around the particle. This force tends to push the object towards the solidification front moving at a velocity V_{sl}. The attractive force was approximated by Uhlmann *et al.* [3] from the viscous drag on a sphere of radius R and at a distance $d (<< R)$ from the planar interface, using the derivation of Carrier [3];

$$F_\eta = \frac{6\pi\eta V_{sl} R^2}{d} \tag{1.4}$$

where η is the viscosity of the melt. To define a critical engulfment velocity (V_c), Uhlmann *et al.* [3] used the maximum growth rate at a critical gap thickness (assumed a few molecular diameters) with a *steady-state* pushing configuration. Hence, the critical engulfment velocity (V_c) is obtained by balancing both forces, i.e. putting $F_\sigma = F_\eta$

$$V_c = \frac{\Delta\sigma_0 d}{3\eta R} \left(\frac{d_0}{d}\right)^n \tag{1.5}$$

The final expression is thus a function of several unknown interrelated parameters $V_c = f(d_0, n)$ and the origin of repulsive interfacial force remains unclear. Furthermore, they assumed a negligible temperature gradient (G) and an ideal planar front geometry with no front curvature ($\kappa = 0$).

1.2.3 Thermal Conductivity & Interfacial Curvature

The simplified approach of Uhlmann *et al.* [3] assumed equal thermal conductivity of the melt (k_m), particle (k_p), and solid (k_s), thereby explaining the idealized planar front geometry. However, an object with a thermal conductivity different from the melt ($k_p \neq k_m$) will modify the local heat flow, thereby modifying the temperature isotherm locally (see Fig.1.4). As we assume the solid-liquid front to follow the isotherm for the melting point (T_m) of the matrix material, this difference of thermal conductivity can bend the front towards or away from the object, depending on whether the thermal conductivity of the object is higher or lower than the melt. Hence, if a particle has a lower thermal conductivity than the melt ($k_p/k_m < 1$), the solidification front bulges towards the object and is convex. In the opposite case ($k_p/k_m > 1$), the solidification front bends away from the particle and is concave [4, 9].

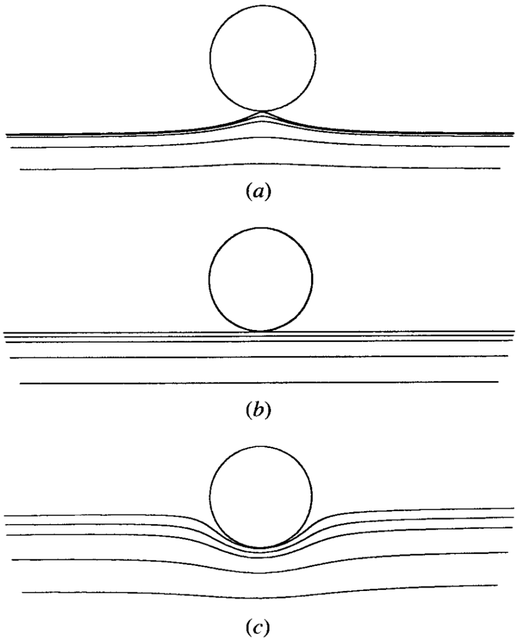

Figure 1.4: Solidification front curvature in the vicinity of a particle with a thermal conductivity mismatch with the melt (a) Convex for $k_p/k_m < 1$, (b) Horizontal for $k_p/k_m = 1$, and (c) Concave for $k_p/k_m > 1$, adapted from [4].

The shape and curvature of the solidification front is an important criterion to predict the particle behaviour in the vicinity of a solidifying interface. The curvature determines the magnitude of attractive and repulsive forces acting on an insoluble object [4, 10, 11, 12]. The approximate viscous drag force in the presence of a curvature assumed *a priori* is given by [4]

$$F_\eta = \frac{6\pi\eta V_{sl} R^2 \alpha^2}{d} \tag{1.6}$$

where $\alpha = 1$ represents a planar interface, $\alpha > 1$ is a concave interface, and $\alpha < 1$ is a convex interface. In general, the cusping of the front behind the particle increases the drag force, F_η, more than the disjoining force, F_σ. Thus, the critical velocity (V_c) may reduce drastically as compared to planar fronts [4, 8, 11, 13].

1.3 Model from Chernov *et al.*

Chernov *et al.* [10, 14] were the first to consider a distortion of the temperature field owing to the differing thermal conductivity of the particle and the melt ($k_p \neq k_m$). They assumed a paraboloidal front shape *a priori* to calculate the forces on the particle (see Fig.1.5). In addition to the rigorous treatment of the temperature field distortion, Chernov *et al.* [10, 14] also tried to explain the origin of the repulsive interfacial forces responsible for the particle pushing. They considered that the particle rejection was due to a disjoining pressure owing to the presence of van der Waals forces. They developed an approach using the non-retarded van der Waals forces varying with the liquid film thickness in the particle-front gap. Their model was relatively successful in predicting the experimental data as compared to the other models [2]. Hence, most of the theoretical studies performed subsequently to model the particle behaviour were based on their approach.

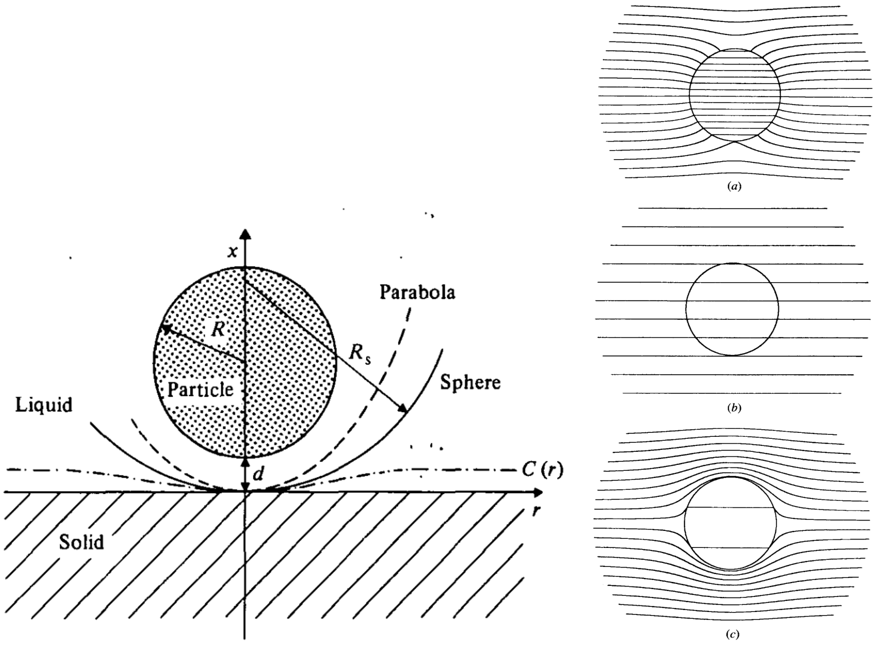

Figure 1.5: Paraboloidal front shape (left) considered *a priori* with distortion (right) of the temperature field ($k_p \neq k_m$) in the model from Chernov *et al* [10, 14], adapted from [4, 15].

1.3.1 Repulsive disjoining pressure

For pushing to occur, a thin liquid film must always be present between the solidification front and the particle, thereby allowing the crystal to grow. Derjaguin and Kussakov [16] were among the earliest to investigate the stability of thin liquid films. They found that an excess pressure adjacent to the bulk liquid was required to maintain a thin liquid film confined between two parallel plates, which they termed as the disjoining pressure. Therefore, the presence of a stable liquid film implies the existence of a disjoining pressure in the particle-front gap (d), which is essentially a jump in pressure at the two solid surfaces adjacent to the thin liquid layer [7]. The disjoining pressure depends on the liquid film thickness (d), and the type and strength of inter-molecular interactions in the system [17, 18]. The disjoining pressure (P_T) owing to dispersion (van der Waals) interactions for a thin film between two unbounded parallel flat surfaces is given as [19]

$$P_T = -\frac{A_{sw}}{6\pi d^3} \tag{1.7}$$

where A_{sw} is the Hamaker constant for the system particle-solid separated by a liquid film. For example, A_{iwp} is the Hamaker constant for the ice, water, and particle system, defined as $A_{iwp} \equiv A_{ip} + A_{ww} - A_{iw} - A_{pw}$. For the ice-water-particle system, the Hamaker constant ranges from -0.1 to -1×10^{-20} J [7]. A negative Hamaker constant corresponds to a repulsive force. The total van der Waals force on the particle is calculated by integrating P_T over the particle surface. A detailed description of the methods of computing the disjoining pressure of van der Waals origin has been provided by Patrick Aubourg [7].

1.4 Models based on Chernov's approach

The analytical model from Chernov *et al.* [10, 14] was the starting point for the development of more rigorous treatments of the solidification front shape. The progress in computing abilities and reduced cost of numerical simulations facilitated the solution of complete differential equations. Most of the previous models had relied on ad-hoc assumptions for the interface geometry and the thickness of the liquid film separating the particle from the solid. The model from Rempel *et al.* [20], built upon a similar approach as Chernov *et al.*, made significant improvements to the domain of object-front interactions. They solved explicitly for the entire shape of the front without assuming the geometry *a priori* (see Fig.1.6). Further, they employed numerical techniques to predict the particle velocity as a function of its position relative to the spatial temperature field, and approximated the fluid flow in the particle-front gap via lubrication theory.

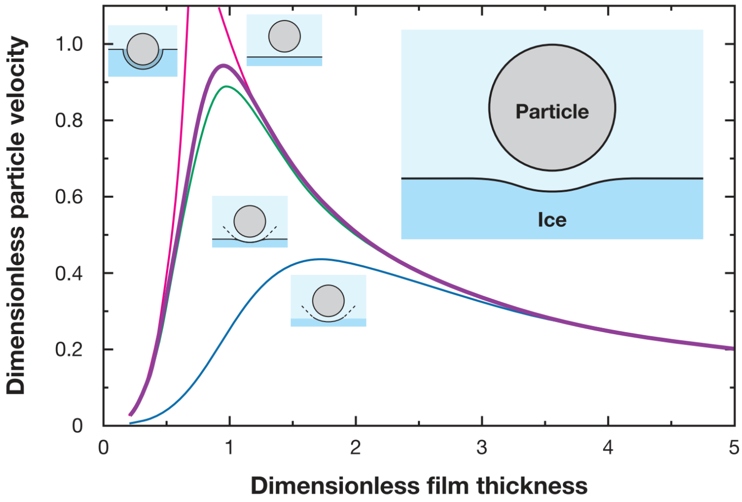

Figure 1.6: The thick purple line shows the particle behavior that is predicted by Rempel *et al.* [20], including the complete interfacial curvature, which, for large film thicknesses, is nearly identical to the results obtained when approximating the front as being planar (rightmost magenta curve). The leftmost magenta curve gives the approximate particle velocity when the thermal conductivity of the particle is assumed equal to that of the melt and the solid. The green curve displays the predictions of Chernov *et al.* [14] for the case where the interface has the form of a paraboloid intersecting with a plane, and the lowest (blue) curve is their prediction for the particle velocity when the front is modeled as a paraboloid, adapted from [21].

Similar to the approach of Chernov *et al.* [10], their model accounts for the presence of a liquid film owing to the intermolecular interactions in the gap between the particle and the solid. To solve for the temperature field during solidification in the presence of a small particle ($R \leq 100\ \mu m$) they defined an interfacial temperature T_i as

$$T_i = T_m \left(1 - \left(\frac{\lambda}{d}\right)^{\nu} - \frac{\sigma_{sl}\kappa}{L_v}\right) \tag{1.8}$$

where T_m is the absolute melting temperature, κ is the front curvature, σ_{sl} is the solid-liquid front interfacial energy, L_v is the latent heat per unit volume of the solid, d is the film thickness between the particle and the front, and λ is a disjoining pressure length scale characterising the strength of intermolecular interactions that dominate (typically λ is of order $10^{-10}\ m$). The exponent ν depends on the type of intermolecular interactions that dominate; $\nu = 3$ represents non-retarded van der Waals interactions, while $\nu = 2$ and $\nu = 4$ is used for retarded van der Waals and long-range electrical interactions [22]. To simplify their approach, Rempel *et al.* [20] considered the role of repulsive van der Waals interactions ($\nu = 3$) for the derivation of a critical velocity. Hence, they used the disjoining pressure length scale λ which can be defined by

$$\lambda = \left(\frac{A_{sw}}{6\pi L_v}\right)^{1/3} \tag{1.9}$$

The effective Hamaker constant A_{sw} can be predicted experimentally or calculated from the dielectric constants of the solid, the liquid, and the particle [20].

1.4.1 Curvature & Interfacial Undercooling

The definition of the interfacial temperature in Eq.1.8 highlights two important phenomena owing to the particle-front interactions. First, the interface curvature impacts the bulk melting temperature of the solid and reduces it by an amount proportional to the κ and the σ_{sl}. This change or lowering of the melting temperature is referred to as the Gibbs-Thomson effect or curvature undercooling. Second, the disjoining pressure caused by the intermolecular interactions also reduces the bulk melting temperature by an amount proportional to the thickness of the liquid film d. This lowering of the melting point is referred to as the interfacial undercooling. Hence, the equilibrium undercooling $T_m - T_i$ increases as the liquid film thickness is reduced, instigating the solid-liquid interface to deviate from the planar T_m isotherm, when it approaches an insoluble particle. In consequence, the interface curvature resulting from this deviation further impacts the equilibrium undercooling. Thus, the interplay between the various interactions determines the shape of the solidification front and hence, the magnitude of forces acting on the particle.

1.4.2 Premelted films

In general, the term premelted films implies the presence of a liquid below the solid bulk melting temperature, T_m, in a thin layer adjacent to another bulk phase in thermodynamic equilibrium. The formation of premelted films can be attributed to three phenomena; curvature induced premelting or the Gibbs-Thomson effect, surface or interfacial premelting, and solute or impurity induced premelting.

Curvature induced premelting or the Gibbs-Thomson effect

The curvature induced premelting, as described in section 1.4.1, is owing to the Gibbs-Thomson effect invoked by the solid-liquid interfacial curvature, κ. This phenomenon is commonly encountered in the freezing of porous media (see Fig.1.7). For example, the water present in the pores of radius R_{pore} in a frozen colloidal suspension can remain liquid and hence, be undercooled (ΔT_{GT}) to a temperature T below its bulk melting temperature T_m, given as

$$\Delta T_{GT} = T_m - T = \frac{T_m}{R_{pore}\rho_i \Delta H_f}\sigma_{iw}\kappa_g \tag{1.10}$$

where σ_{iw} is the ice-water interfacial tension, ρ_i is the density of ice, ΔH_f is the bulk enthalpy of fusion, and κ_g is a geometric prefactor that depends on the porous structure and the wetting properties ($\kappa_g = 2$ for cylindrical pores and perfect wetting).

Surface or interfacial premelting

The surface or interfacial premelting can occur when the solid is in contact with its vapour phase (called surface premelting), in contact with a similar solid interface with a different geometric orientation (called grain-boundary premelting), and in contact with a foreign substrate such as a particle (called interfacial premelting).

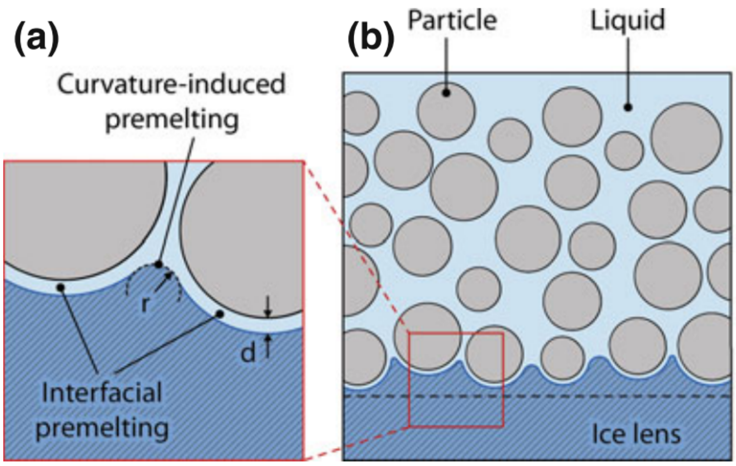

Figure 1.7: Curvature-induced and interfacial premelted films at an ice-particle-water interface, adapted from [23].

The interfacial undercooling ΔT_{IF} for a solid-liquid interface can be given as

$$\Delta T_{IF} = \frac{T_m}{L_v} P_T \tag{1.11}$$

where the disjoining pressure P_T varies as a function of the premelted film thickness d (see section 1.3.1).

The deformation of the solid-liquid interface and the presence of the liquid film which separates the particle from the solid surface are both manifestations of the phenomenon known as interfacial premelting [22, 24]. The liquid present in this film is below the bulk melting temperature T_m, and represents a disordered quasi-liquid region formed as a result of the competition between a reduction of interfacial free energy and the expense of maintaining a layer of undercooled liquid [24].

As stated previously, the thickness of the premelted film, d, depends on the equilibrium undercooling, $T_m - T_i$ (see Eq.1.8), and determines the magnitude of the repulsive disjoining pressure (see Eq.1.7) depending on the type of inter-molecular interactions considered (see Fig.1.8). The thickness of the premelted film decreases with an increasing undercooling. The flow of bulk liquid towards the solidification front to ensure crystal growth is instigated owing to the disjoining pressure through the premelted film (see section 1.3.1). Moreover, the flow depends on the geometry and thickness of the film, which depend on the surface energy and curvature as well as the strength of the inter-molecular

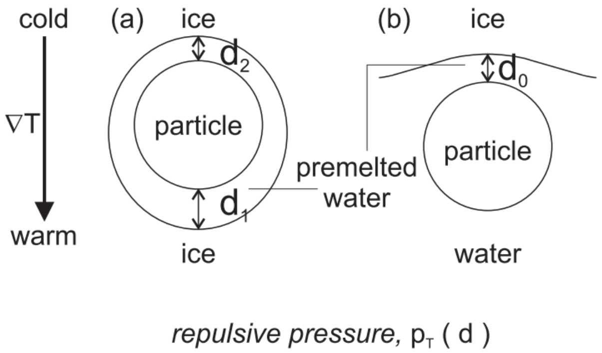

Figure 1.8: Thickness of the premelted film, d, depends on the temperature, and determines the magnitude of the repulsive disjoining pressure P_T, adapted from [25].

interactions [21].

Solute or impurity induced premelting

The addition of a solute or impurity can greatly enhance the phenomenon of premelting through a colligative effect (Raoult's law) lowering the chemical potential of the solvent. As most solids have a lower solubility for solutes as compared to the liquid phase, the solutes rejected during solidification can further enhance the chemical potential difference at the solid-liquid interface [26]. Therefore, a small amount of impurity or solute in the parent liquid can have drastic impacts owing to its segregation during solidification (see section 1.5.2). The thickness of the solute premelted films is highly sensitive to the dopant concentration and is dominated by the colligative effects at sufficiently high solute (or impurity) concentration [27]. The solute (or impurity) induced undercooling (ΔT_{SO}) on a flat substrate ($R \to \infty$) can be given as

$$\Delta T_{SO} = \frac{R_g T_m^2 N_i}{L_v d} \tag{1.12}$$

where R_g is the universal gas constant and N_i is the number of moles of solute per unit surface area of the substrate. This equation can be used in ice-water-particle systems with high solute concentrations, where the particle is larger than a micron and the equilibrium undercooling is greater than 0.05 K. Hence, an increase in the solute concentration increases the premelted film thickness.

The physics of premelting in ice has been investigated in detail owing to

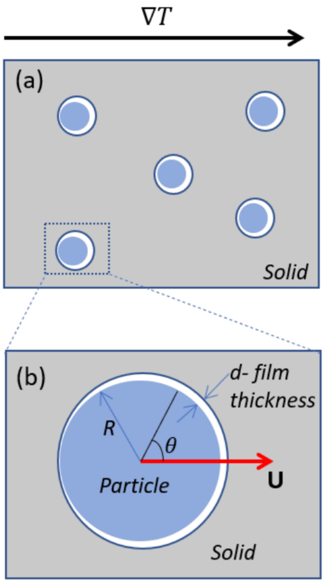

Figure 1.9: *Regelation* or migration of small particles in a solid towards the warmer side of the temperature gradient ∇T owing to a thermomolecular pressure gradient from the varying thickness of the premelted films, adapted from [27].

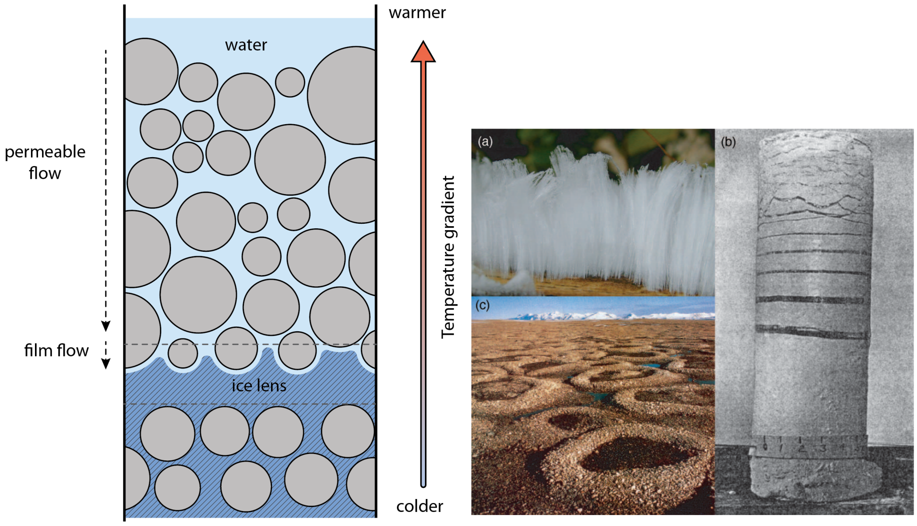

Figure 1.10: The physics of premelted films is investigated in the growth of ice lenses with various natural manifestations such as frost heave in partially frozen soils, adapted from [23, 26].

its far-reaching implications including, among other things, frost heave in partially frozen soils (see Fig.1.10), electrification of thunderclouds, and glacier motion [26]. Furthermore, the thermal gradient induced fluctuations of the premelted film are known to be at the origin of *regelation* of particles engulfed in a solid [28]. The thermal or pressure induced regelation can cause migration of small particles ($\leq 1\ \mu m$) through ice, whereby the particles translate towards the warmer side of the underlying ∇T, owing to a thermomolecular pressure gradient [29] (see Fig.1.9).

1.4.3 Model from Rempel *et al.*

Rempel *et al.* [20] calculated the repulsive interfacial (or thermomolecular) force by integrating the Lifshitz expression for disjoining pressure (see Eq.1.7) over the interfacial surface for a spherical particle. To derive the attractive viscous (or lubrication) force, they first used a lubrication approximation in the particle-front gap to find the volume flux of liquid moving in the premelted film. Subsequently, they calculated a lubrication pressure using conservation of mass since the volume of liquid solidified should be equivalent to the volume of liquid swept in the particle-front gap (premelted film) as the front moves with a velocity V_{sl}. The lubrication (or viscous) force is then calculated by integrating the lubrication pressure over the particle surface.

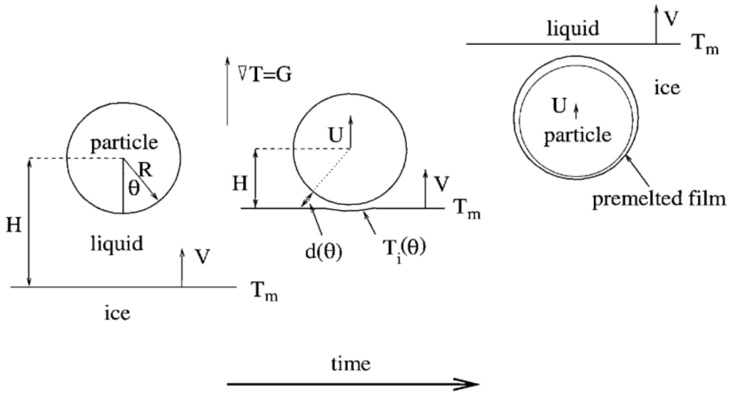

Figure 1.11: Model from Rempel *et al.* [20] accounts for the presence of a liquid premelted film owing to the inter-molecular interactions in the gap between the particle and the solid, adapted from [30].

For the critical velocity, they determined that the force is maximum at the base of the particle ($\theta = 0$) where the premelted film is thinnest (see Fig.1.11). Hence, they derived a film thickness of the order $\epsilon_s R$ near the base of the particle

($\theta = 0$), diverging towards infinity at $\theta = \pi/2$, defined as

$$\epsilon_s = \left(\frac{A_{sw}}{6\pi\sigma_{sl}R^2}\right)^{1/3} \tag{1.13}$$

Using typical values for a particle-in-water system, where $A_{sw} \approx 10^{-20}\ J$, $\sigma_{sl} \approx 10^{-2}\ J \cdot m^{-2}$ and $R \approx 10^{-6}\ m$, we get $\epsilon_s \approx 10^{-3}$ and hence, a minimum film thickness of $\approx 1\ nm$. The critical velocity, equated by a balance of thermomolecular and lubrication forces at minimum premelted film thickness ($\epsilon_s R$), is given as

$$V_c = \left(\frac{\sigma_{sl}A_{sw}^2}{6^5\pi^2\eta^3R^4}\right)^{1/3} \tag{1.14}$$

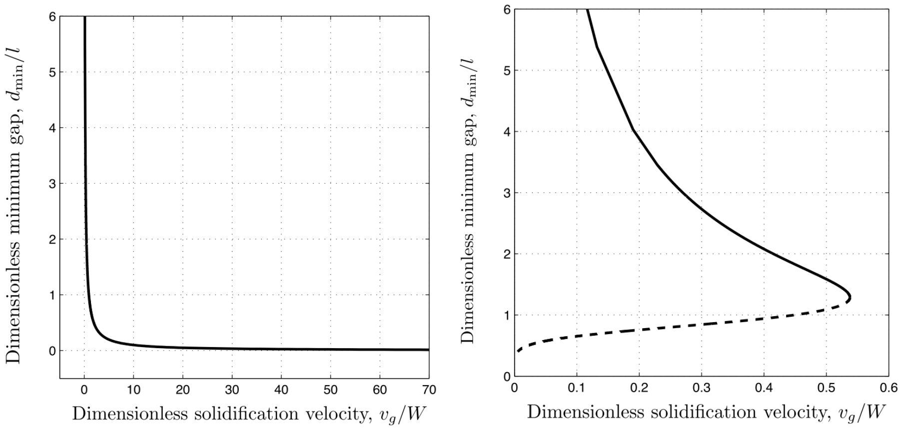

(a) (b)

Figure 1.12: Under *steady-state* conditions, the particle velocity is equal to the solidification velocity. (a) When the premelting effect is excluded from the model, the gap thickness decreases monotonically with increasing solidification velocity. A critical velocity for engulfment must be defined via an arbitrary minimum gap thickness. (b) When premelting is included, the Rempel *et al.* [20] model predicts two solution branches, with two values of gap thickness for a given solidification velocity. A critical engulfment velocity is naturally defined as the maximum solidification velocity, or limit point, of the steady-state solution branches, adapted from [31].

Hence, a solidification front moving at a velocity V_{sl} will engulf a particle if the characteristic critical velocity is $V_c < V_{sl}$. The critical velocity is a function of the particle radius ($V_c \propto R^{-4/3}$) and interestingly, independent of the temperature gradient (G). Therefore, larger particles tend to be engulfed in the solid at relatively lower growth rates as compared to smaller particles. The influence of R on V_c changes with the type of inter-molecular interactions. $V_c \propto R^{-3/2}$ for retarded van der Waals interactions, while $V_c \propto R^{-1}$ for electrical interactions was deduced by their model.

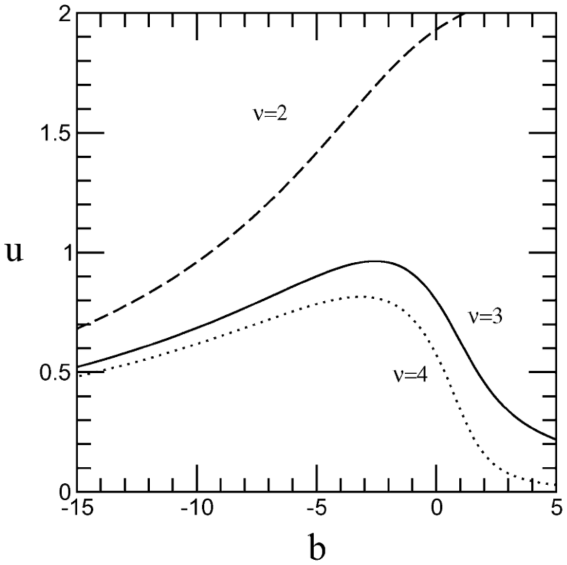

Figure 1.13: The dimensionless particle velocity (u) versus dimensionless particle height (b) varies with the type of inter-molecular interactions ν taken into account. When b is large and negative the edge of the particle is below the plane of the T_m isotherm. The exponent ν depends on the type of inter-molecular interactions that dominate; $\nu = 3$ represents non-retarded van der Waals interactions, while $\nu = 2$ and $\nu = 4$ is used for retarded van der Waals and long-range electrical interactions [22], adapted from [20].

The model from Rempel *et al.* [20] clearly highlighted the *steady-state* particle velocity as a function of the premelted film thickness. Furthermore, their results demonstrated two *steady-state* gap thicknesses corresponding to a single particle velocity. The larger of these gap sizes represented a stable pushing of the particle, while the smaller represented an unstable state eventually leading to engulfment. Finally, the model also provided a unique critical velocity, for a given set of solidification parameters, depicted by the maximum of the particle velocity-gap thickness curve [20]. Hence, the incorporation of premelting in the model circumvented the problem of inferring a critical velocity using an arbitrary minimum gap assumption (see Fig.1.12). However, the main drawback of the model was the assumption of equal thermal conductivity of the particle, the melt, and the crystal. This casts doubt on the predicted shape of the solidification front in the vicinity of an insoluble object (with $k_p \neq k_m$), as discussed previously in section 1.2.3.

1.4.4 Model from Park *et al.*

Park *et al.* [32] developed further on the analytical approach from Chernov *et al.* [10] by incorporating the role of thermal conductivity mismatch ($k_p \neq k_m$) in the numerical analysis of the particle-front interactions. Their model was similar to that from Rempel *et al.* [20] in the use of premelting effects (non-retarded van der Waals interactions) for deducing the repulsive disjoining pressure (see Fig.1.13). Moreover, they also followed a similar lubrication approximation for estimating the magnitude of attractive viscous drag forces in the particle-front gap. In contrast to Rempel *et al.* [20], they took into account the influence of bulk flow induced by the density variation upon solidification. This is important as the flow of liquid can be towards (or away) from the solid depending on whether the density of the solidified phase is larger (or smaller) than the melt. The model also included the analysis of a bubble interacting with a solidification front. The major difference between a bubble and an insoluble particle was assumed to be the effect of thermocapillary stress (Marangoni effect) owing to the variation of bubble surface tension with temperature.

The critical velocity (V_c) expression derived for a particle or bubble is given as

$$V_c = \frac{1}{6\eta R}\left(\frac{L_v A_{sw}^3 G}{(6\pi)^3 T_m}\right)^{1/4} u_{max}(\gamma, k_p/k_m) \tag{1.15}$$

where u_{max} is the maximum of the dimensionless particle velocity and γ is a dimensionless surface energy parameter defined as

$$\gamma = \frac{T_m \sigma_{sl}}{L_v G R^2} \tag{1.16}$$

The dimensionless u_{max} varies as a function of the premelted film thickness (d), particle to melt thermal conductivity ratio (k_p/k_m), and the surface energy parameter (γ). The typical values of u_{max} were estimated to be $10^{-3} \leq u_{max} \leq 10$ for a thermal conductivity mismatch of $0.01 \leq k_p/k_m \leq 100$ with the surface energy parameter in range $0 \leq \gamma \leq 100$.

The model systematically analysed the interactions of an object with an approaching solidification front. The authors highlighted the major impact of

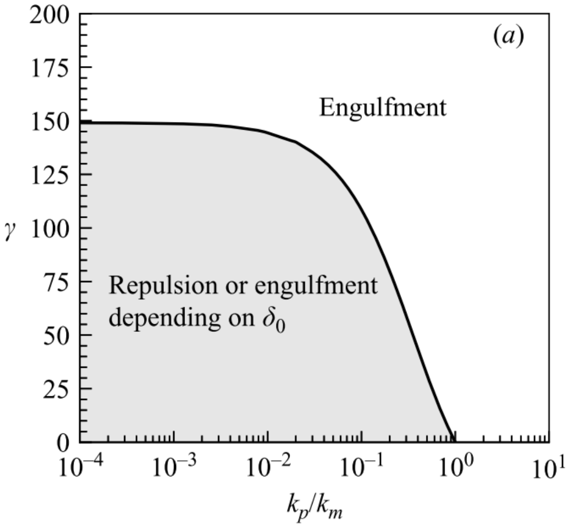

Figure 1.14: The model from Park *et al.* [32] suggested that a small particle-to-melt thermal conductivity ratio promotes repulsion, while particle engulfment is facilitated when the ratio is large, adapted from [32].

thermal conductivity mismatch ($k_p \neq k_m$) and of solid-liquid interfacial energy (σ_{sl}) on determining the shape of the solidification front. They concluded that the object behaviour is strongly influenced from the thermal conductivity mismatch between the particle and the melt ($k_p \neq k_m$). Hence, they suggested that a small particle-to-melt thermal conductivity ratio promotes repulsion, while particle engulfment is facilitated when the ratio is large (see Fig.1.14). Furthermore, the V_c deduced from their model predicts values one order different as compared to that computed from the Rempel *et al.* [20] model.

1.4.5 Model from Tao *et al.*

I will now briefly discuss one of the most recent model from Tao *et al.* [31], employing finite element methods to estimate the particle behaviour. This model uses the numerical solution approach to predict the complete shape of the solidification front in the presence of the premelted liquid layers (see Fig.1.15). The study was a detailed attempt to accurately resolve the magnitude of forces acting on a particle in close proximity to the solid-liquid interface. This is a complex problem as the solidification front does not remain planar in the vicinity of an insoluble object. The authors further made a comparison of their force magnitude estimations with those obtained from the analytical model of Rempel and

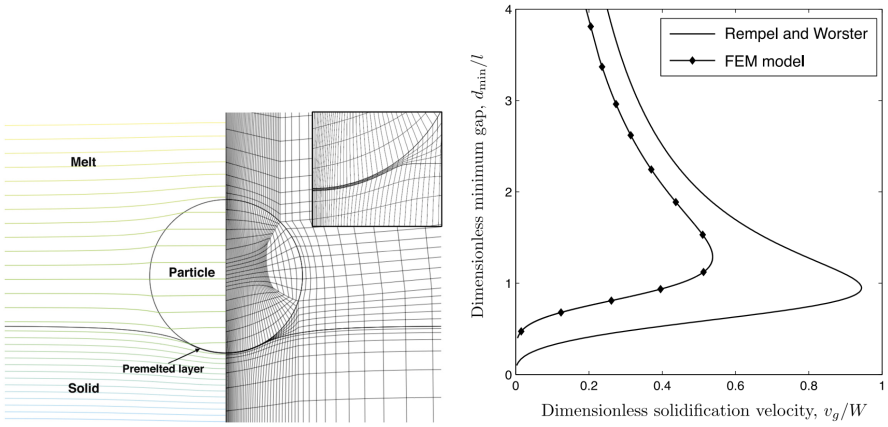

Figure 1.15: Left: The model from Tao *et al.* [31], employing finite element methods to estimate the particle behaviour. Right: A comparison of their estimations with those obtained from the analytical model of Rempel and Worster [30], adapted from [31].

Worster [30].

The major differences presented in this study as compared to the previous analytical models were the approximations used to calculate the two forces; the repulsive van der Waals force and the attractive viscous drag force. For estimating the former, the model used the Hamaker's law [33] as it takes into account the geometry of the problem (sphere-plane). The authors argued that the Lifshitz expression (see Eq.1.7) used in previous models [20, 30, 32, 34] had been derived for parallel plate geometry and hence, overestimates the repulsive forces.

To calculate the drag force, the model did not rely on the lubrication approximation and instead numerically resolved the Navier-Stokes equations for computing the flow throughout the liquid domain. Their study suggested that the lubrication approximation approach is not accurate and underestimates the drag force by 30%. Therefore, the critical velocity predicted by models employing the lubrication approximation (for drag) and/or the Lifshitz expression (for repulsion) have higher values in contrast to their model (see Fig.1.15). However, the study from Tao *et al.* [31] used simplifying assumptions such as equal thermal conductivity of the particle, the melt, and the crystal. The model also neglected the Gibbs-Thomson effect and the bulk flow produced by density change upon solidification.

1.5 Solute effects

1.5.1 Context

I have discussed so far the interaction of objects with a solidification front in a pure solution. In real-life systems, the probability of encountering a pure melt is rare and solutes (or impurities) are often present. The addition of solute to a solvent may be desired and hence, their presence enhances the mechanical and/or physical properties of the solidified material. Additives, referred to as cryoprotectants, are frequently used to reduce damage inflicted to biological cells during their freezing at extremely low temperatures (ranging between -5 and $-15\ °C$) [35]. Polymers, referred to as dispersants, are generally added to the slurry in freeze-casting to prevent flocculation of the suspended ceramic particles and hence, ensure a homogeneous solidified structure [36].

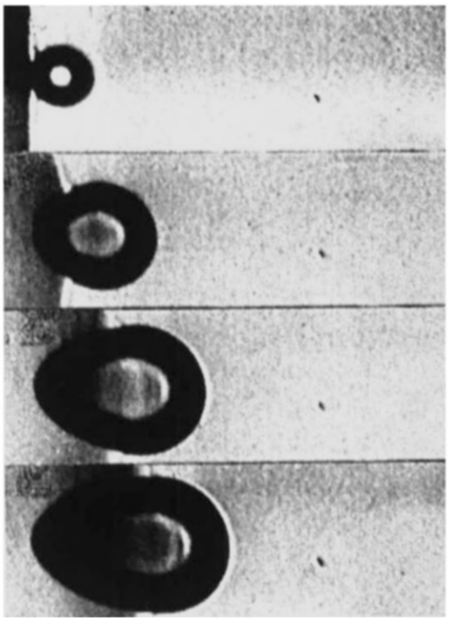

Figure 1.16: Rejection of impurities during solidification (such as dissolved gases) can lead to the undesired nucleation and growth of bubbles at the solid-liquid interface, adapted from [15].

In contrast, the presence of solutes (or rather impurities) in certain situations is deleterious to the properties of the solidifying material. The dissolved gases (especially H_2 and N_2) in molten metals can instigate the formation of porosity or blow holes (see Fig.1.16), thereby serving as stress-concentration sites and inducing premature material failure [37]. Inclusions of SiC arising during solidification of multi-crystalline silicon (mc-Si) reduce the solar cell efficiency and can lead to wafer rupture [38].

I will now discuss some of the mechanisms at play owing to the presence of solutes during solidification. This will help us to further understand the impact of solute when objects interact with an advancing solid-liquid interface. The list of solute mechanisms discussed is not exhaustive as the solutes can impact several other parameters including the suspension viscosity, solid-liquid interfacial tension, preferred crystal growth direction, solutal convection, premelted film rheology, however, these phenomena remain highly complex to investigate [23].

1.5.2 Solute Diffusion

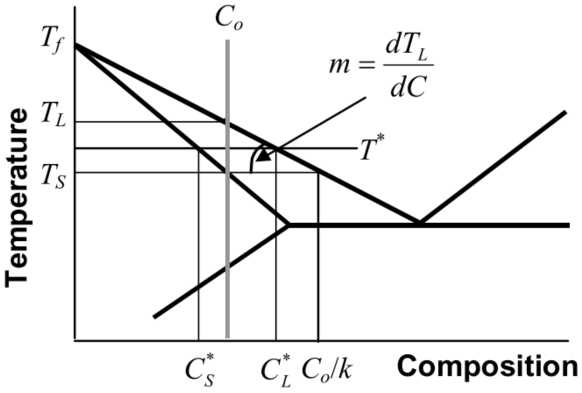

Figure 1.17: Binary phase diagram representing solidification for a solution starting at the liquidus temperature (T_l) and terminating at the solidus temperature (T_s). The solute rejected by the growing solid phase creates a diffusion field in the remaining liquid phase. Reproduced with permission from [39].

A major distinguishing parameter in solidification of pure and impure solutions is the melting temperature. A pure melt solidifies (or freezes) at a constant temperature, while an impure solution solidifies over a range of temperature. The solidification for a solution starts at the liquidus temperature (T_l) and terminates at the solidus temperature (T_s) (see Fig.1.17). In general, the solubility of a solute is less in the solid phase than in the liquid phase. For example, O_2 gas is more soluble in water as compared to ice [40]. As solidification progresses, the solute is rejected by the growing crystal, thereby corresponding to an increasing concentration of solute in the remaining liquid [41] (see Fig.1.18). For steady-state planar growth, where the transport of solute takes place by diffusion only, the concentration field of solute in the liquid is given by

$$C_L = C_0 + C_0 \left(\frac{1 - K_0}{K_0} \right) exp \left[\frac{-V_{sl}}{D} x \right] \tag{1.17}$$

where C_L is the concentration, C_0 is the bulk concentration in the liquid far from the interface, D is the solute diffusion coefficient, x is the distance from the interface, and K_0 is the partition coefficient. This diffusion model from Tiller *et al.* [41] has simplifying assumptions where the diffusion in solid is negligible, the value of K_0 stays constant during solidification, and the convection in liquid is neglected. However, we suggest that the model can be used to avoid complex calculations in *steady-state* directional solidification at small growth rates with a constant temperature gradient.

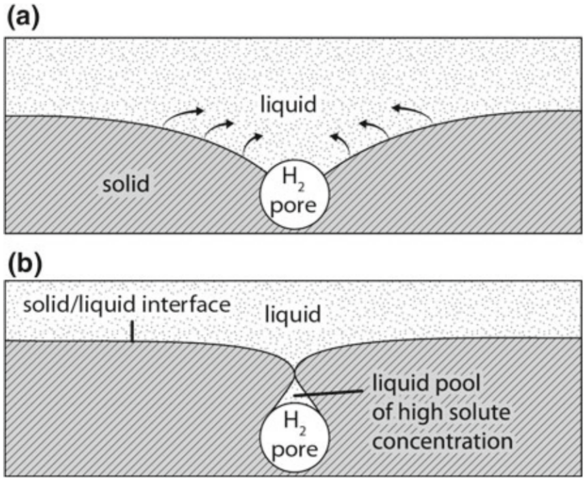

Figure 1.18: Schematic representation of the comet tail-shaped segregation region in front of the hydrogen pore: (a) Solute diffusion towards the sample centre-line before complete engulfment, and (b) at the time of complete engulfment, a liquid pool of high solute concentration is engulfed, adjacent to the hydrogen bubble, adapted from [42].

1.5.3 Constitutional Undercooling

During solidification in the presence of objects, the segregation of solutes at the interface is enhanced further by the approaching objects obstructing their diffusion field [12]. Since growth from solutions depends on the concentration

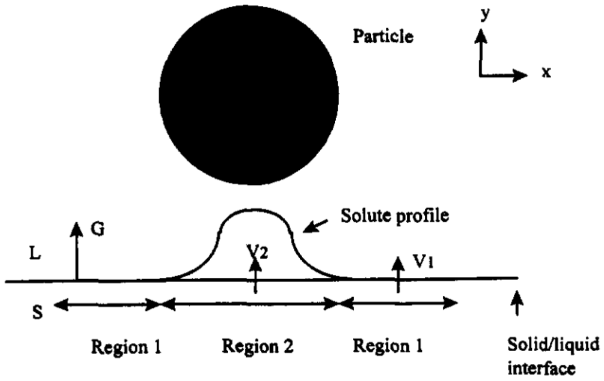

Figure 1.19: The segregation of solutes at the interface is enhanced further by the approaching objects obstructing their diffusion field, thereby invoking higher solute concentration behind the foreign objects. Adapted from [12].

gradient of solutes, the liquidus temperature of the melt in the vicinity of the front differs from the liquidus temperature of the bulk liquid far from the front. As the solute segregates, the liquidus temperature further decreases. This change in liquid composition alters its transformation temperature, referred to as constitutional undercooling [41]. Hence, in other words it is a colligative effect of freezing point depression instigated by the solute segregation and enhanced further between the objects and the solidification front (see Fig.1.19).

1.5.4 Front morphology

In directional solidification, the advancing solid-liquid front can have predominantly three morphologies; planar, cellular (or columnar), and dendritic (see Fig.1.20). The constitutional undercooling owing to the solute segregation, in addition to the growth rate and the temperature gradient, determines the front morphology. In general, a high thermal gradient has a stabilising effect, while a solute concentration gradient has a destabilising effect on a *steady-state* planar front [15]. The planar to columnar front transition is instigated by a growing instability, defined by models such as the Mullins-Sekerka (see Fig.1.21), where the constitutional undercooling is a necessary criterion [43]. The growth of single crystals requires a planar interface, while casting and welding microstructures are formed under conditions which give rise to cellular and dendritic interfaces [44]. The spatial distribution of the objects in the solidifying material depends on the advancing front morphology [45]. The solute rejection hence plays a major role in

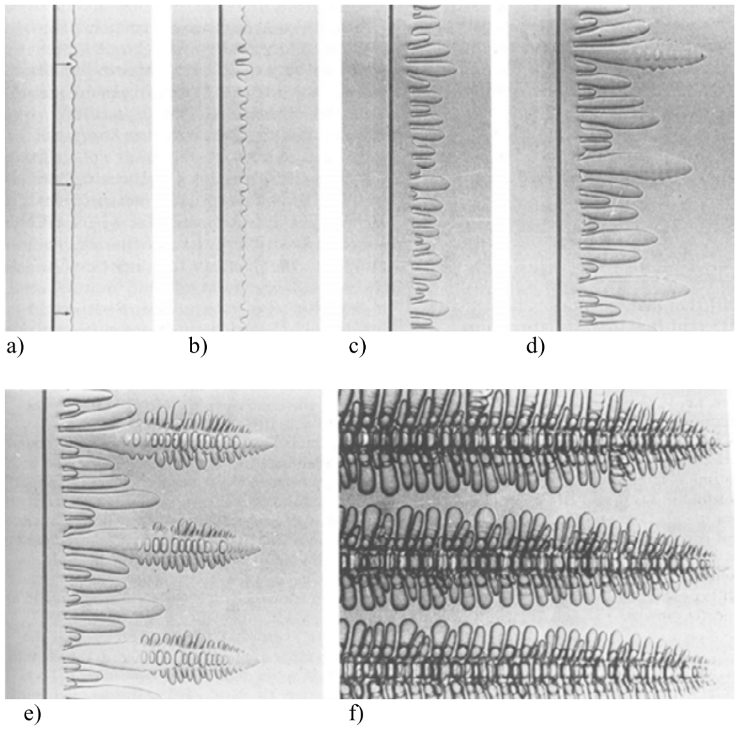

Figure 1.20: Progressive destabilisation of a planar front morphology (a) leading to a dendritic microstructure (f) during directional solidification, adapted from [39].

determining the final solidification microstructure and the segregation patterns.

1.5.5 Solute segregation

The solute segregation between the object and an approaching solidification front gives rise to solute induced premelted films (see section 1.4.2). This local solute enrichment is of particular importance in understanding several mechanisms that can occur at the solid-liquid interface. The nucleation and growth of bubbles at the front is instigated when the concentration of gases rejected by the growing solid exceeds a certain solubility limit value [40] (see Fig.1.16). These bubbles can be subsequently engulfed in the crystal leading to macroporosity defects [42]. The rejection of additives during the freezing of biological cells can lead to elevated solute gradients in the remaining liquid. As most biological cells are made of water, they can undergo membrane rupture (or cryoinjury), when subjected to such high osmotic stress owing to the local solute concentration [15, 46].

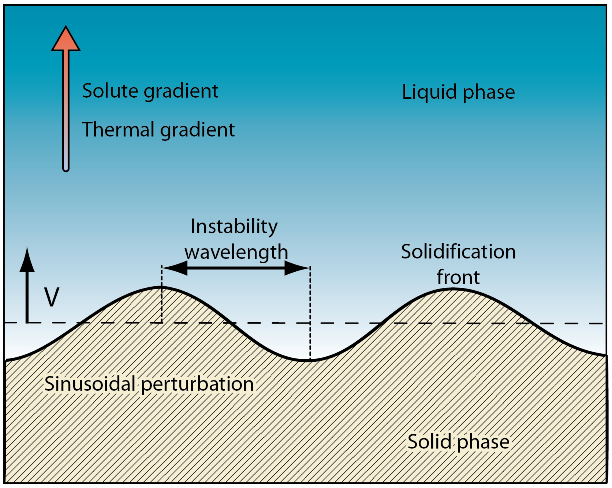

Figure 1.21: Schematic depicting the formation of Mullins-Sekerka type instability promoted by constitutional undercooling in the liquid ahead of the solid-liquid interface, adapted from [23].

1.5.6 Theoretical models incorporating solute effects

I will now discuss the theoretical models studying the interaction of a foreign object with a solidification front in the presence of solute effects. Most theoretical studies, as shown in section 1.2, only consider solidification of pure materials, whereas many real-life situations of interest involve the solidification of solutions or alloys. Although the solute effects have widespread applicability, yet only a few models have investigated this scenario. In contrast to pure melt models, the solute models need to incorporate the impact of constitutional undercooling owing to the rejected solute segregation. Hence, the solute models essentially need to solve for the thermal and solute concentration field in the particle-front gap to accurately estimate the solidification front shape.

The earliest model solving for a coupled temperature and solute field in the presence of a particle was derived by Pötschke & Rogge [8]. Their approach for estimating the force equilibrium was similar to Chernov *et al.* [14], using the non-retarded van der Waals interactions for the repulsive force and the viscous drag for the attractive force. They numerically solved for the solute concentration in the particle-front gap and calculated the corresponding liquidus temperature from the equilibrium phase diagram. They further utilised the liquidus temperature as isotherms and predicted the interfacial curvature. To determine a critical velocity, they fitted a function to their numerical solutions using an intermediate range of parameters for R, η, D $etc\ldots$ and estimated it as

$$V_c \approx 0.053R^{-1}\left(\frac{A_{sw}GDK_0}{\eta|m|C_0}\frac{k_p}{k_m}\right)^{1/2} \tag{1.18}$$

where $|m|$ represents the absolute value of the liquidus slope. The model was one of the first attempts at solving the complex problem of solute field concentration and hence, had several simplifying assumptions. The authors notably ignored the Gibbs-Thomson undercooling induced by the solid-liquid interfacial energy (σ_{sl}).

Sasikumar & Ramamohan [11] performed a rigorous treatment of the temperature field distortion using numerical methods. The study followed a similar approach of using intermolecular interactions to calculate the force equilibrium. The model tried to predict the shape of the front using the solute concentration, curvature undercooling, and constitutional undercooling contributions. However, the authors did not provide a critical velocity scaling and only presented qualitative arguments stating that $V_c \propto C_0^{-1}$. The authors deduced that the critical velocity for solutions is much lower as compared to pure melts. They further suggested that the particle engulfment in solutions by a planar front may not be likely as the front tends to destabilise before approaching the V_c. Thus, the front destabilisation velocity (planar to cellular transition) can be lower than the V_c. However, no theoretical proof was provided for these conclusions.

Kim & Rohatgi [12] tried to predict the shape of the front from the ratio of diffusion coefficient of solute to the growth rate (D/V_{sl}). The authors estimated the force equilibrium using a similar approach as Pötschke & Rogge [8]. However, the model does not provide any scaling for the critical velocity and made qualitative predictions for the shape of the solidification front. The model predicted a concave front curvature at low growth rates ($\leq 10\ \mu m \cdot s^{-1}$) owing to the extensive constitutional undercooling in the particle-front gap. The model also, similar to previous studies, concluded that the critical velocity for alloys or solutions was much smaller than for pure melts.

Kao *et al.* [34] performed a systematic analysis of the behaviour of objects in solidifying binary alloys. They considered a force equilibrium in the presence of ionic solutes in solution, given as

$$F_\sigma + F_\eta + F_g + F_{DL} = 0 \tag{1.19}$$

where F_σ is the repulsive force from van der Waals interactions, F_η is the attractive

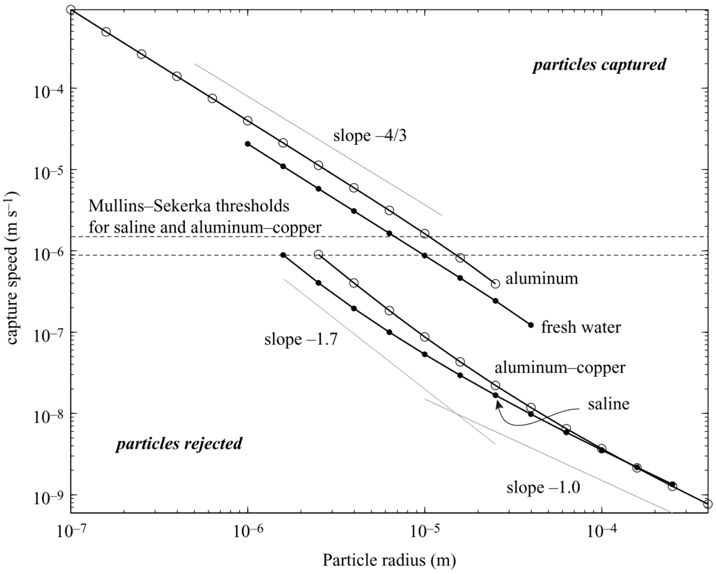

Figure 1.22: The capture or rejection of particles as a function of particle radius and solidification front speed. Systems above and to the right of the lines (mentioning slope) display particle capturing behaviour, while systems below and to the left display particle-pushing behaviour. There is a significantly sized region where particles may be pushed in a pure system but captured in a binary system. Reproduced from the model of Kao *et al.* [34].

force from the viscous fluid drag, F_g is the buoyancy force, and F_{DL} is the double-layer repulsion force from the ionic solutes. The critical velocity scaling provided by the model in a simplified form can be expressed as

$$V_c \propto R^{-1.30} G^{0.35} \sigma_{sl}^{0.30} A_{sw}^{0.35} \eta^{-0.35} D^{0.65} \tag{1.20}$$

Interestingly, the authors deduced that the ionic double layer force was too weak and did not impact the object behaviour. The authors suggested that the double layer had little effect as their length scales were much smaller compared to the van der Waals premelting distances used in their calculations. In agreement with the previous solute models, the V_c derived for binary alloys was an order lower than the corresponding pure melts (see Fig.1.22). The authors suggested that the lower values of V_c were due to the increased particle-front gap induced by the constitutional undercooling. Therefore, the repulsive van der Waals was assumed to be considerably reduced owing to the increased particle-front separation.

A different approach towards modelling of solute effects was adapted by

Chang *et al.* [35]. Here, the authors investigated the interaction of biological cells with an advancing solidification front to emulate cryopreservation. In this level-set model, the numerical simulations calculate the force on a particle without assuming a specific geometry for the problem, thereby improving the scope, range, and accuracy of the predictions. Therefore, the authors estimated the repulsive van der Waals forces between multiple surfaces with arbitrary geometries. Furthermore, the drag forces in the model were computed by a step method to avoid analytical solutions of the lubrication approximation. The model is hence rich in terms of the object behaviour predicted and requires much less approximations in contrast to analytical models. However, the study does not provide a systematic influence of the various solidification parameters on the particle behaviour and remains limited to two-dimensional systems.

Other level-set models, studying the interaction of particles with solidification fronts in presence of impurities, have been developed by Catalina *et al.* [42] and Yang *et al.* [47]. These models investigated the interplay between the particle-melt thermal conductivity mismatch ($k_p/k_m \neq 1$) and the role of solute on the shape of the interfacial curvature (concave or convex). The studies deduced that the diffusion of solute plays an important role on the solidification front shape, whereas the thermal conductivity ratio (k_p/k_m) does not affect it. Thus, a concave curvature of the front has been predicted theoretically in the presence of solute.

Hence, the major conclusions of the theoretical models incorporating solute effects can be summarized as follows. The solutes are rejected by the growing crystal and segregate in the particle-front gap. This scenario applies to the systems where the solutes are less soluble in the solid phase in contrast to the liquid phase i.e. the partition coefficient $K_0 << 1$. The segregated solutes induce constitutional undercooling in the solute premelted films owing to their local enrichment, thereby rendering the solidification front concave. The concave geometry of the front facilitates the engulfment of the foreign objects at lower growth rates ($V_c^{solution} < V_c^{pure\ melts}$) owing to the increased drag force (see section 1.2.3) and reduced repulsive van der Waals force. The ionic nature of solute has no impact on the force equilibrium and therefore, the double-layer forces can be neglected. However, all of these conclusions are theoretical in nature.

1.6 Experimental Results

I have presented till now an overview of the theoretical models developed over the years for pure melts and solutions. A plethora of analytical and numerical approaches predicting the outcome (engulfment or repulsion) of a foreign object interacting with an advancing solidification front were also discussed. I will now try to highlight the experimental studies conducted to understand the object behaviour during solidification and their subsequent correlation(s) to the theoretical models. To clearly distinguish the context and the domain where the mentioned studies were performed, I will discuss the results of hard and soft objects separately. Although a number of theoretical models have been derived, yet the experimental verification of these models remain extremely limited [2, 15].

1.6.1 Experimental techniques

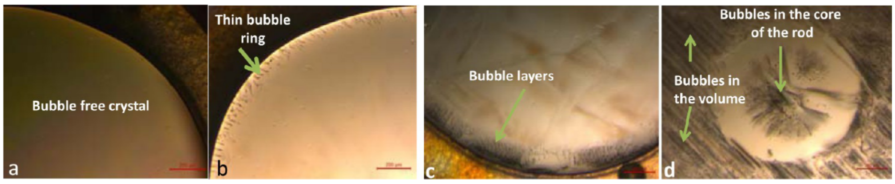

Figure 1.23: Bubbles' distribution in the cross section of the sapphire rod crystal as a function of the growth rate (V_{sl}) **(a)** $V_{sl} = 0.25\ mm \cdot min^{-1}$**, (b)** $V_{sl} = 1\ mm \cdot min^{-1}$**, (c)** $V_{sl} = 1.5\ mm \cdot min^{-1}$**, and (d)** $V_{sl} = 2.5\ mm \cdot min^{-1}$**, reproduced from [48].**

Solidification with objects is a complex phenomenon, where multiple interdependent parameters influence the object-front interaction. An important primary step is to observe, directly or indirectly, these interactions to improve their understanding. The typical features owing to these interactions include the front curvature (concave or convex), object behaviour (engulfment or repulsion), front morphology (planar, cellular, or dendritic), object spatial distribution, object deformation (or not), and premelted films. The essential factors affecting the solidification features are the growth rate V_{sl}, temperature gradient G, particle size R, and the solute concentration C_0. These factors or parameters need to be regulated efficiently to comprehend their systematic impact on the features obtained (see Fig.1.23).

Complex nature of interactions

The solidification features vary in their time and space scales over different orders of magnitude. For example, the liquid premelted film is supposed to be of $\approx 10\ nm$ thickness, while the particle size can typically vary from 10 to 100 μm. The typical time scale of interest depends on the crystal growth rate ($1 \leq V_{sl} \leq 40\ \mu m \cdot s^{-1}$) and the duration over which an object interacts with the interface ($0 \leq t \leq 100\ s$). Thus, the major problem associated with studying solidification arises from the need of high space and temporal resolution in conjunction with the corresponding need of attaining the matrix melting temperatures ($\approx -10 \leq T_m \leq 1000\ °C$). Therefore, the choice of the experimental observation technique depends largely on the features which needs to be analysed.

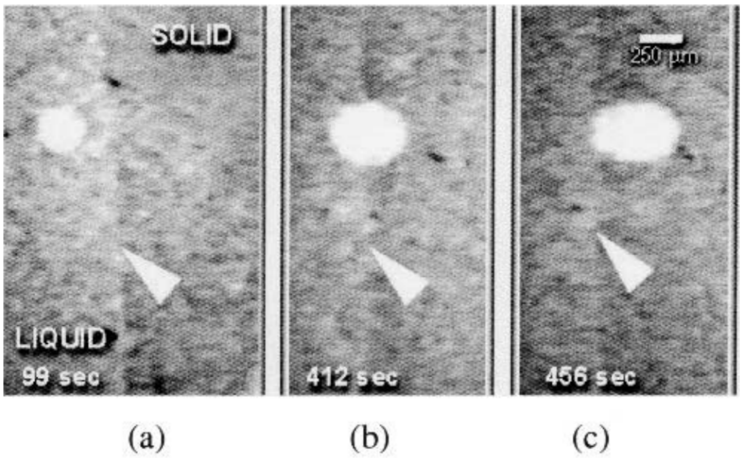

Figure 1.24: X-ray transmission microscopy in a liquid aluminium matrix to study the interaction and development of gas porosity with a moving solidification interface. The arrow points to the solidification front, reproduced from [42].

Tools used in metallurgy

In metallurgy, a significant number of studies performed in the past have relied on the post-solidification analysis to predict the object behaviour during solidification of particle-reinforced-composites [9, 49]. Therefore, the initial observations were mostly qualitative and limited to the specific system utilised for the experiments. Subsequently, the use of low melting point organic analogues (see section 1.6.2) facilitated the *in situ* observation of object-front interactions

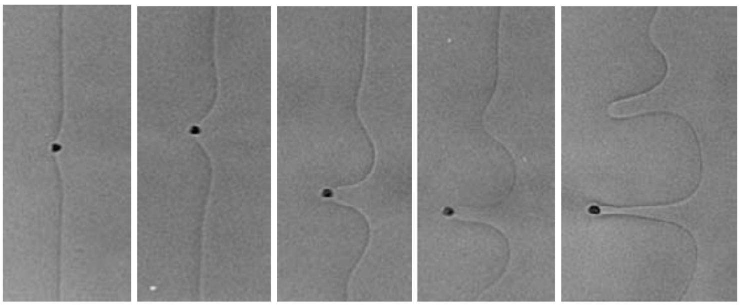

Figure 1.25: Use of optical microscopy with low melting point organic analogues to understand object-front interactions. A SiC particle interacting with the solid-liquid interface in a succinonitrile matrix, adapted with permission from [39].

with the aid of an optical microscope [7, 50, 51, 52]. More recently, the *in situ* investigations at high temperatures have been performed for aluminium alloys using an X-ray transmission microscope (XTM) [42, 53]. The main limitations include the spatial resolution at the particle level, high energy x-ray induced artefacts [54], and the visualization of solute segregation (see Fig.1.24,1.25).

Tools used in biology

In cryobiology, the interaction of biological cells with an ice-water front have been often investigated using cryo-microscopy [15, 55]. The device is essentially an optical microscope combined with a freezing stage to facilitate imaging of a solidifying aqueous suspension. The advantages include resolution of the extracellular ice growth and the cellular reactions to the surrounding environment.

Körber *et al.* [57] employed a spectrophotometer in their cryo-microscopy setup to determine the redistribution of solutes (cryo-additives) and the resulting concentration profiles photometrically or densitometrically. A direct visualization of the solute segregation, however, remained evasive. Further progress in this field has been through the design of computer operated slow cooling stages and the use of high optical resolution CCD cameras [56]. This facilitates an accurate control over the applied crystal growth rate and the imposed temperature gradient (see Fig.1.26). However, the imaging is still limited to *2D*.

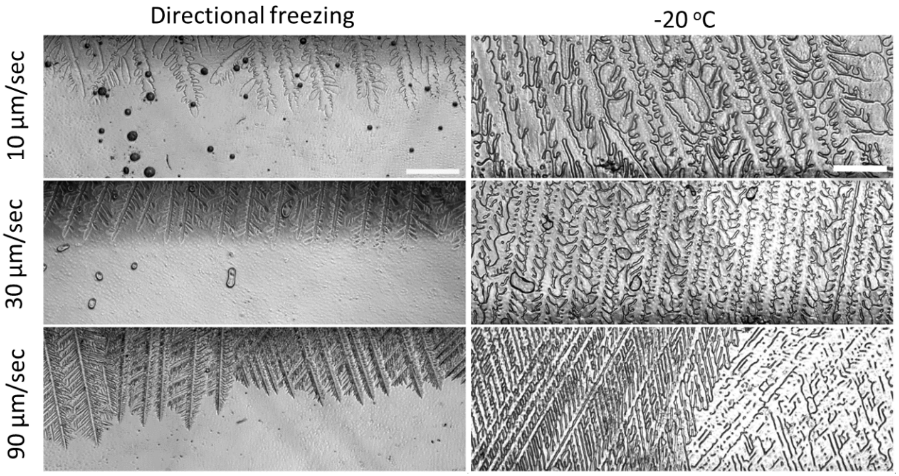

Figure 1.26: Directional solidification of an aqueous (10% DMSO) suspension to evaluate the freeze-thaw viability of biological cells. Ice crystal morphology as a function of the ice front propagation. Left: during the process of freezing. Right: Frozen sample at $-20\ °C$. Scale bar indicates $400\ \mu m$. Adapted with permission from [56].

Tools used in our study

I shall now briefly recapitulate the development and the advantages of the cryo-confocal technique used in this thesis. In contrast to an optical microscope, a confocal microscope consists of an additional pinhole (specimen-detector) and hence, displays only the signal coming from a single focal plane (see Fig.1.27). This makes the image sharper, avoids blur from out-of-plane components, and allows 3D reconstruction by acquiring optical slices at different depths along the sample thickness.

Marcellini *et al.* [58] developed a procedure to follow *in-situ* the time-lapse growth of ice crystals in *3D*. The imaging of the aqueous suspension was performed by adding a fluorophore. The ice crystals were distinguished as they reject the fluorophore during growth ($K_0 << 1$) and hence, appear black (see Fig.1.28). The addition of a second fluorophore to the dispersed objects enabled an individual as well as multiple object(s) resolution and the imaging of three phases (ice, water, and objects) simultaneously.

Dedovets *et al.* [59] developed a directional freezing stage with an individual control over the imposed temperature gradient (G) and the displacement of the sample (V_{sl}). The stage was adapted for a laser scanning confocal microscope

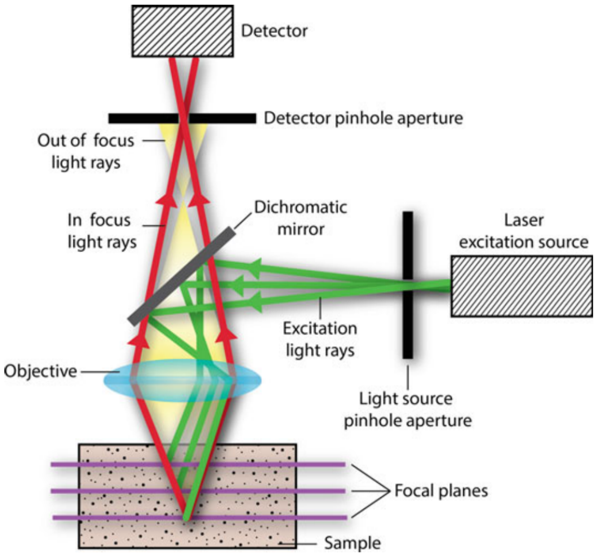

Figure 1.27: Principles of confocal microscopy. Reproduced from [23].

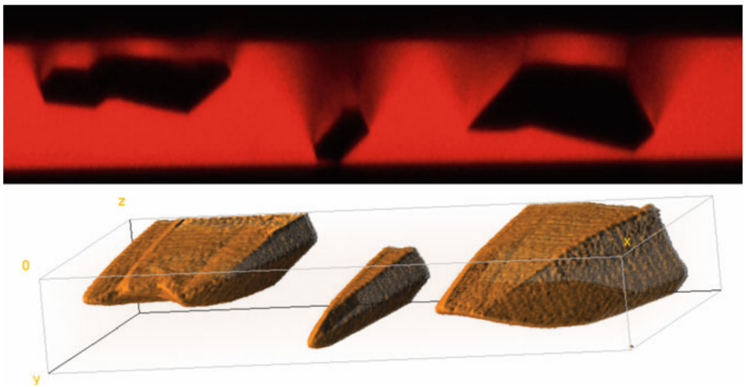

Figure 1.28: Typical confocal microscopy image of ice crystals growing in an aqueous solution that contains a fluorophore (Sulforhodamine B, here). The red corresponds to the liquid water, the black regions in the centres are the crystals. The three-dimensional reconstruction of the crystals surface is shown in the lower picture (front view). Procedure developed by Marcellini *et al.* [58].

and made use of insulating foam to avoid thermal perturbations emanating from the objective lens. This ensured a stable thermal gradient and hence, a systematic control over the essential solidification parameters (see Fig.1.29). A multi-phase imaging of freezing particle suspensions with the possibility of tracking the individual objects at a high frequency in 2D and 3D was subsequently

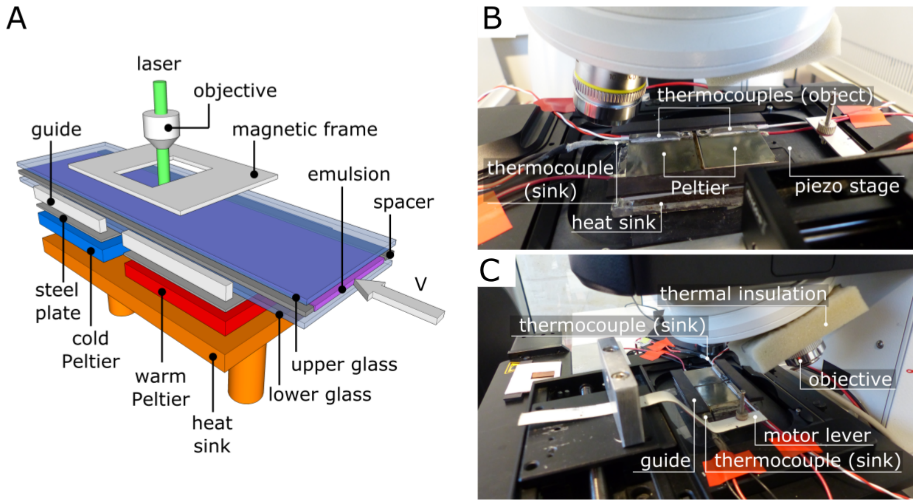

Figure 1.29: Overview of the temperature gradient stage developed by Dedovets *et al.* [59] for *in situ* operations under the confocal microscope: A constant temperature gradient is achieved in the gap between the Peltier elements. If the sample is pushed at a velocity V, a solidification front moves at a velocity $U_{front} = V$. The solidification front is thus always in the centre of the observation windows, which is useful for solidification studies. (A) 3D representation, (B and C) Photographs of front and side views. Reproduced from [59].

demonstrated [60]. The segregation of the rejected fluorophores (from ice) facilitated the resolution of the expected solute concentration profile and helped in elucidating the role of solutes in freezing oil-in-water emulsions [61]. Presently, the use of this cryo-confocal microscopy setup, as employed in this thesis, is also helping to establish and correlate the biological cell's physico-chemical environment and the cell-front interactions during their directional freezing [62] (see Fig.1.30).

1.6.2 Hard Objects (Ceramic, Metal, & Polymer Particles)

A major part of the previous studies investigating particle-front interactions has been to comprehend the development of the material microstructure. Of particular interest, the design and optimization of particle-reinforced metal-matrix-composites and single crystal growth (see Fig.1.31). The objective of these studies was primarily to deduce the particle capture (or repulsion) to elucidate the spatial distribution of objects in the solidified microstructure [2]. The desired outcome ranges from instantaneous engulfment of particles in metal-matrix-

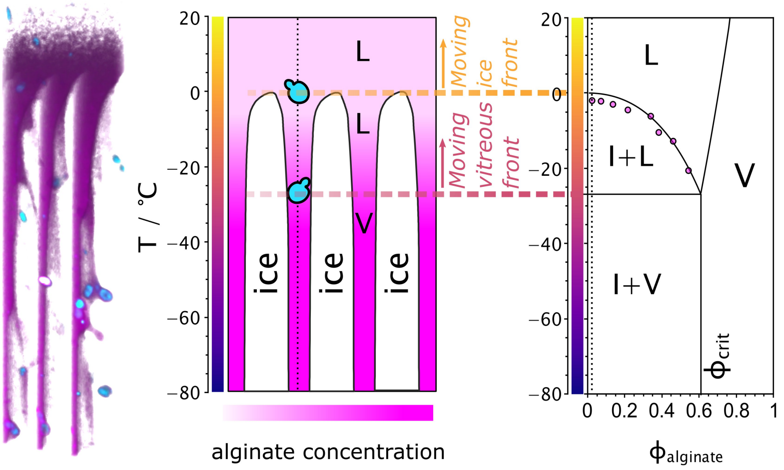

Figure 1.30: Cryo-confocal microscopy of yeast cells in alginate solution to correlate their physico-chemical environment to the cell-front interactions. Work performed by Qin *et al.* [62] using the *in situ* solidification setup developed in the lab.

composites to rejection of dissolved impurities in single crystals. Therefore, the studies have essentially focused on the estimation of the critical velocity (V_c), as a function of the various solidification parameters comprising the growth rate (V_{sl}), particle radius (R), melt viscosity (η), thermal gradient (G), and particle-melt thermal conductivity mismatch ($k_p / k_m \neq 1$).

The experimental studies on particle-front interactions have utilised different systems to study the impact of solidification parameters; particle type (e.g. latex, PMMA, SiC, Al_2O_3, Cu, Fe etc...), particle size ($3 \leq R \leq 1000\ \mu m$), growth direction (horizontal or vertical), and matrix type (e.g. Al-Si, camphor, salol, succinonitrile, water, Pb-Sn etc...) [2].

The use of organic matrices instead of metals was mainly for two reasons. First, most of the organic matrices are transparent in samples of moderate thickness and hence, the particles could be observed while they were being pushed or engulfed by the growing crystal. The other reason for the use of organic matrices is owing to their low melting point ($0 \leq T_m \leq 220\ °C$) [7], which facilitates the experiments at laboratory scale. The choice of organic matrices with a low entropy of fusion ($\Delta S_f / R_g < 2$, where R_g is the gas constant and ΔS_f is the entropy of fusion), such as camphor, succinonitrile-acetone, also presents the benefits of a macroscopically smooth interface (non-faceted growth), similar to most metals. A non-faceted growth implies that the macroscopic interface follows

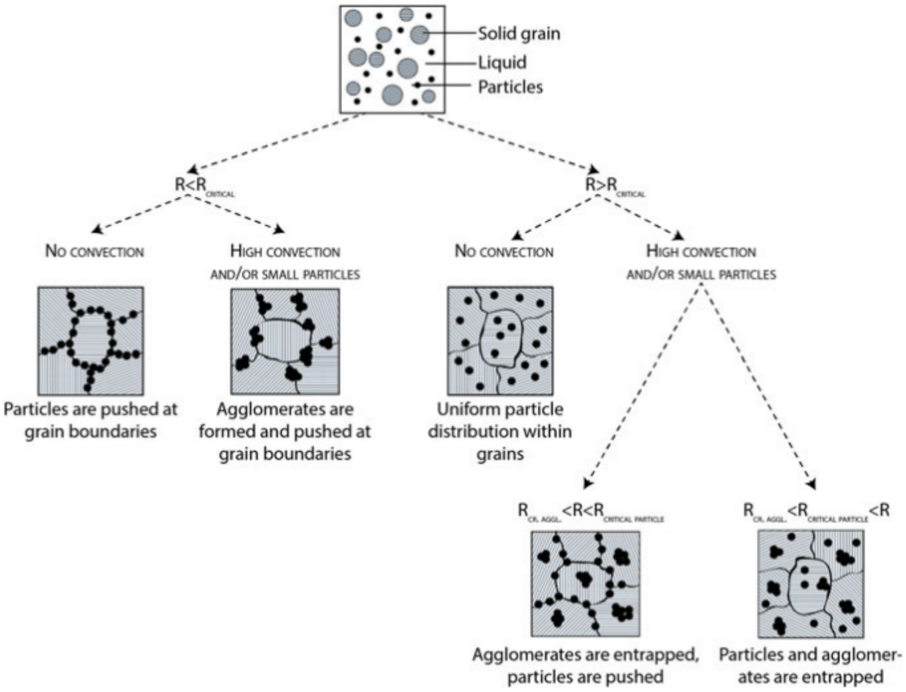

Figure 1.31: Schematic representation of the possible outcomes for the microstructure in multi-directional solidification of metal-matrix-composites, as a function of solidification rate, convection level, and particle size. A variety of solidification patterns and microstructures can be obtained. Adapted from [9].

the underlying temperature isotherms. In contrast, the use of high entropy of fusion matrices ($\Delta S_f / R_g > 2$), such as salol, thymol, can result in a macroscopically rough interface (faceted growth, e.g. needle-like). Thus, the prediction of a critical velocity (V_c) can be questionable if the front is faceted as most models are based on a macroscopically planar front [7].

A comprehensive review of the previous experimental work has been performed by Aubourg [7]. Three decades ago, Asthana & Tewari [2] did an extensive examination of the previous experimental results and the reliability of the various theoretical models in predicting the same. Both the studies have concluded that the different experimental data are difficult to compare and hence, the theoretical correlation remains suggestive rather than definitive. This implies that each theoretical model explains only a certain part of the experimental result and hence, cannot be utilised for all systems. The authors have suggested that the complex behaviour is owing to the lack of available experimental details (like growth rate, thermal gradient etc...) and unknown exact particle shape and surface finish. These parameters are essential for investigation and become critical as the forces are applied on a very limited region near the base of the particle. Furthermore, the experimental studies were unable to rigorously satisfy the assumptions of a particular theoretical model such as *steady-state* planar front, pure melts, faceted growth, etc... [2, 7]. Thus, only some qualitative conclusions could be drawn from the previous experimental observations.

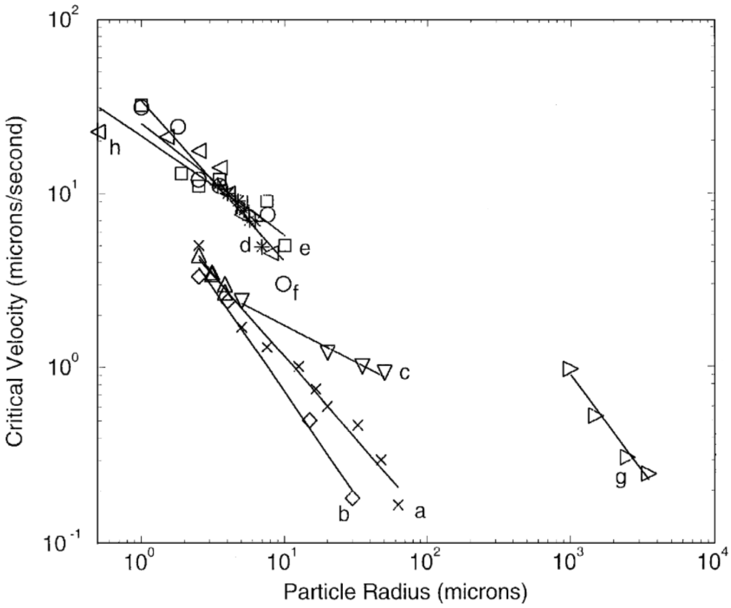

Figure 1.32: The dependence of the critical velocity on the particle radius from a number of experimental studies. A best-fit line is shown running through each of the data sets, where the slope varies from -0.8 to -1.3. The different symbols from (a) to (f) correspond to the particles in water (copper, tungsten, nylon, and latex), (g) and (h) correspond to polystyrene and silicon carbide particles in succinonitrile melt respectively. The temperature gradient varies from $200\ K \cdot m^{-1}$ to $10^4\ K \cdot m^{-1}$. Reproduced from [30].

In general, the critical velocity is a function of the size of the particle and varies approximately as $V_c \propto R^{-\alpha}$, where α varies between 1 and 3/2 (see Fig.1.32). The critical velocity is observed to be generally decreasing with an increasing melt viscosity ($V_c \propto \eta^{-x}$). The impact of thermal gradient (G) on the critical velocity could not be estimated accurately. This is mostly owing to a low sensitivity in the regulation of temperature or a lack of suitable setups. Interestingly, none of the previous experimental investigators reported the observation of a premelted film, an essential criterion for particle pushing. Finally, it was reported that a sharp transition between engulfment-repulsion at the V_c does not exist, rather the particles can be pushed for a certain distance before engulfment (see Fig.1.33). This is further referred to as the pushing-engulfment or the repulsion-trapping transition [2]. Thus, the critical velocity appears to be a range of velocities and not a unique value for a given set of solidification parameters.

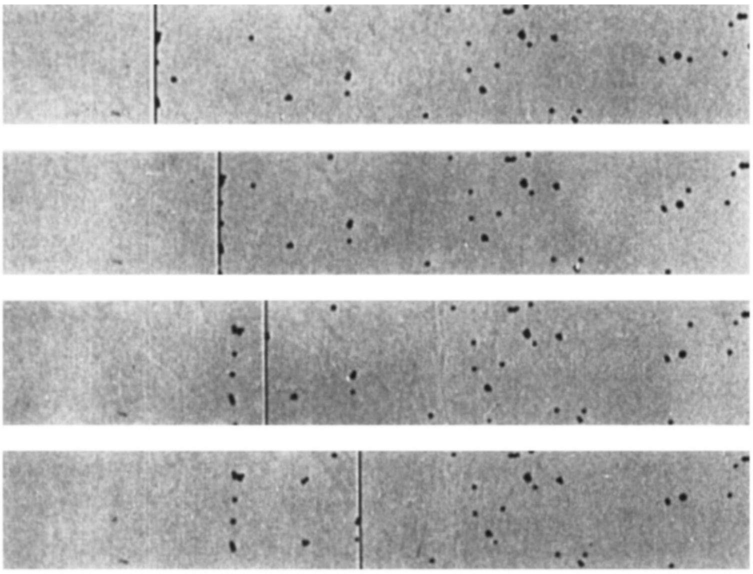

Figure 1.33: Sequence of micrographs showing a section across the observation slit as the planar ice-liquid interface propagates through a suspension of latex spheres (diameter $5.7\ \mu m$) in water. A pushing-engulfment phenomenon can be envisaged, however, the front does not seem to have a constant growth rate. Time interval between each frame is reported as $30\ s$. Reproduced from [57].

The impact of particle-melt thermal conductivity ratio (k_p/k_m) and solutes on the critical velocity presents conflicting results in the existing literature. Zubko *et al.* [63] have qualitatively reported the repulsion of thermally insulating particles ($k_p/k_m < 1$), while an engulfment of thermally conducting particles ($k_p/k_m > 1$) in the solidification of metal-matrix system. Although they did not present results on the accurately measured critical velocity for their system. In contrast, Sen *et al.* [53] have reported the engulfment of thermally insulating particles ($k_p/k_m < 1$) during the solidification of an aluminium-bubble system.

Körber *et al.* [15] have reported no impact of solute on critical velocity in water-$NaMnO_4$ solution, in contrast to the theoretically expected decrease in

V_c (from pure melts) owing to the impurity effects. On the contrary, Sekhar & Trivedi [50] have demonstrated strong impacts of impurity leading to particle trapping in the directional solidification of succinonitrile-acetone system.

1.6.3 Soft Objects (Bubbles, Cells, Droplets)

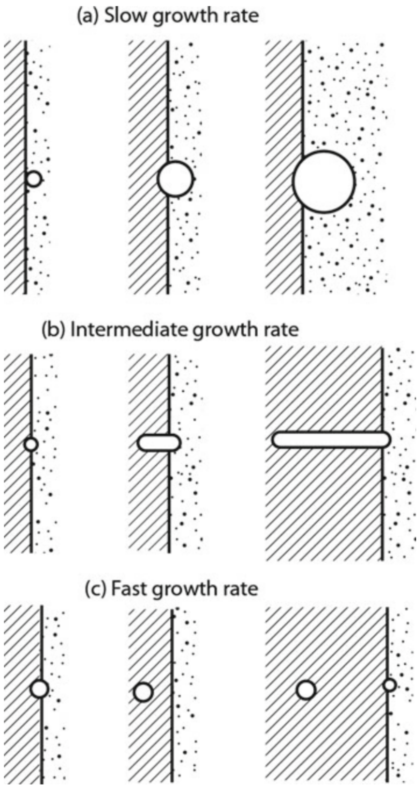

Figure 1.34: Effect of growth rate on the interaction between a bubble and an advancing solid–liquid interface. Reproduced from [64].

Soft objects by definition can deform and their shape might (or might not) change during their interaction with a solidification front (see Fig.1.34). This is an interesting situation as their deformation can divulge the unique nature and direction of forces present as well as provide insights into the corresponding solidification parameters (melt viscosity, growth rate). The domains consisting of soft objects are quite widespread and include cryopreservation of biological cells, freeze-thaw stability of food emulsions, and the growth of bubbles/pores (e.g. H_2) in solids during solidification etc.... The theoretical models discussed previously can essentially be used to describe these interactions, although, certain aspects (like deformation) require a separate investigation. I will now highlight a few examples where soft objects can be encountered and their corresponding observed behaviour while undergoing directional solidification with a planar front. An in-depth review of the mechanisms involved for each type of object is, however, not in the scope of the thesis.

Biological Cells

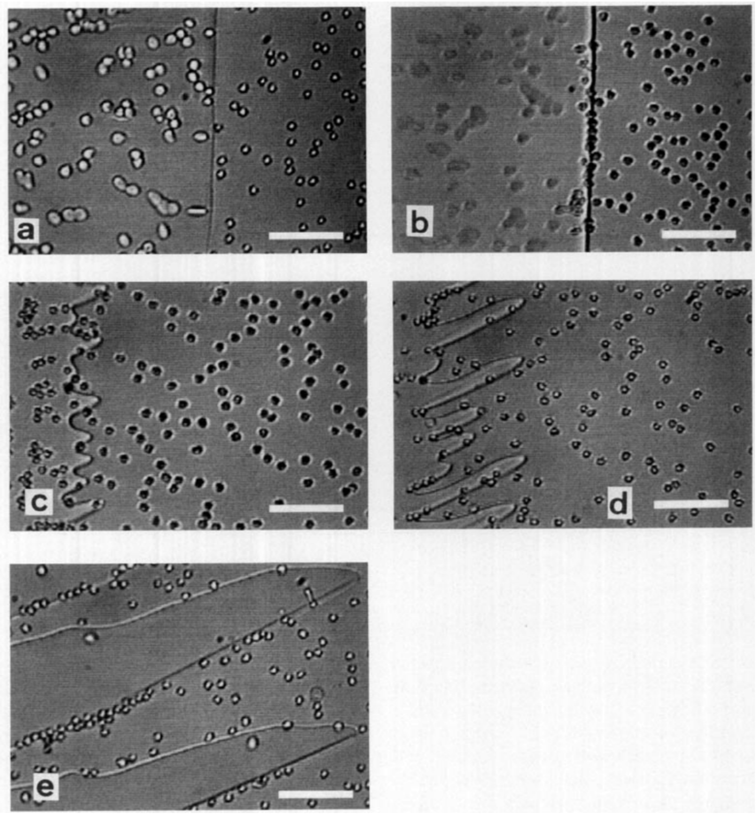

Figure 1.35: Interactions between ice crystals and red blood cells observed using cryo-microscopy. Different redistribution behaviours are observed, depending on the temperature gradient and crystal growth velocity. Adapted from [55].

To ascertain the efficiency of a cryopreservation protocol, the biological cell viability is the most important criterion [46]. The cell viability, or population of healthy/living cells when freezing and thawing, is reduced drastically owing to two damage inflicting mechanisms; intracellular ice formation and osmotic injury [65]. It is generally agreed that the primary cause of damage during freezing is chemical; related to the increased concentration of solutes (rejected during slow freezing) in the unfrozen environment [55]. The cells, mostly made of water, get dehydrated to be in equilibrium with the surrounding osmotic pressure [15, 35]. More recently, Mazur *et al.* [65] have suggested that the damage to red blood cells could also originate from the mechanical stress induced by the growing ice crystals (see Fig.1.35).

A comprehensive review of the cryopreservation field has been complied by Körber [15]. Most studies in the domain of cryopreservation have experimentally investigated the freezing rate and the optimum concentration of additives to achieve an improved freeze-thaw cell viability [55, 56]. However, a systematic study of the cell-front interactions with the impact of corresponding solidification parameters is still lacking. To this effect, a recent study by Qin *et al.* [62] has demonstrated the importance of quantifying the local solute concentration, based on the approach invoked in this thesis, to help understand the cell viability during directional freezing (see Fig.1.30).

Bubbles

The study of soft object deformation has been of particular interest in the prediction of pore shape evolution during directional solidification of crystals to avoid or control porosity defects [42]. Moreover, the science of bubble formation and subsequent trapping in ice also has climatic and geophysical applications. Since gas solubility in solid is usually much less than in the liquid, the rejected gases accumulate ahead of the solidification front. Consequently, nucleation of bubbles at the front can be invoked by the local super-saturation (see Fig.1.16).

The heterogeneous nucleation of gas bubbles on an advancing solidification front was investigated experimentally by Wei & Lee [66]. Their study tried to correlate the concentration of the rejected gases (similar to solutes) to the critical radii of heterogeneously nucleating bubbles. The shape of oxygen and carbon dioxide bubbles engulfed by a growing ice-water interface has been investigated by Wei *et al.* [67]. Their study reported an initial spherical growth and a solidification-rate controlled elongation. Yoshimura *et al.* [40] have reported the observation of egg-shaped and cylindrical oxygen bubbles with an increasing growth rate, while using an ice-water system (see Fig.1.36).

In contrast to the hard objects, the size of bubbles can change owing to the absorption of rejected gases during their interaction with a solidification front. The growth of bubbles at an ice-water interface at a high freezing rate

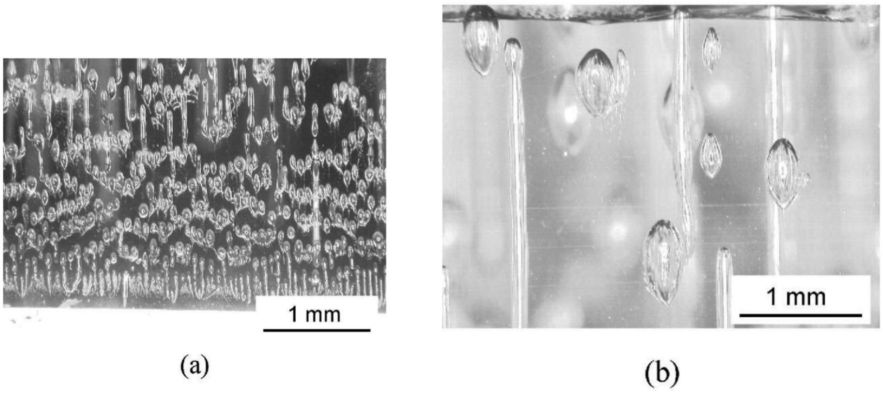

Figure 1.36: Typical shape and patterns of oxygen bubbles incorporated in ice. (a) Egg-shaped bubbles. (b) Egg-shaped bubbles and cylindrical bubbles. The bubble shape depends on the freeze front velocity and the concentration of oxygen dissolved in water. Reprinted with permission from [40].

with the presence of a premelted film has been observed by Maeno [68]. He also reported the formation of a cylindrical gas tube in ice, when the growth rate of the bubble was comparable to the imposed freezing rate. Another distinct behaviour reported in bubbles is their motion relative to the front instigated by a change in the bubble surface tension. This change can be invoked either due to the underlying temperature gradient and/or a solute concentration gradient in the vicinity of the front [32]. This thermo-solutal effect has been investigated experimentally by Wang *et al.* [69] who observed the horizontal motion of bubbles towards an ice-water front in the presence of a surfactant. However, a systematic analysis of the interaction of bubbles with an advancing solidification front is yet to be performed.

Droplets

Interaction of a liquid droplet with an advancing solidification front is commonly encountered in the freezing of emulsions. Emulsions are thermodynamically metastable systems containing droplets of one immiscible liquid dispersed in another. Most studies on the freezing of emulsions are related to food engineering and hence, investigate the resistance of food emulsions to freeze-thaw cycling [70]. The major objective in this domain is the preservation of size, shape, and distribution of the liquid droplets to ensure longevity and conserve the original taste as well as texture. Moreover, freezing helps to delay spoilage by microbial growth and enzyme activity [71].

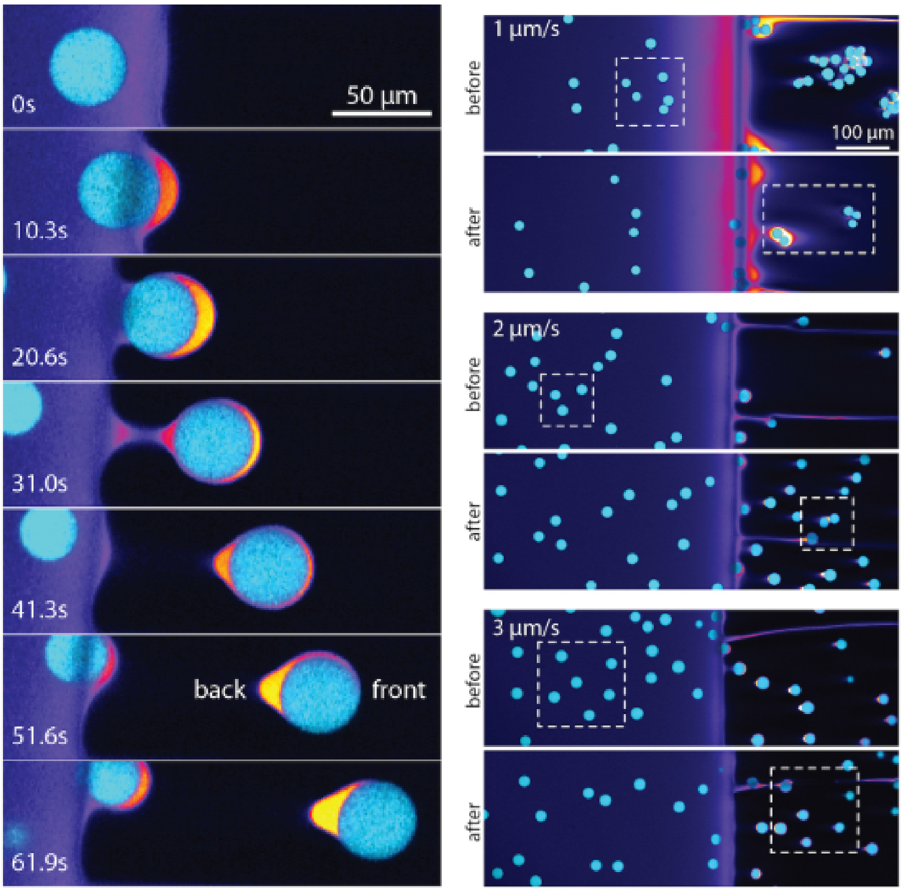

Figure 1.37: Typical interaction between an oil droplet and an ice-water solidification front. Left: Depicting the accumulation of solute and its dynamic redistribution around the droplet. Right: Impact of growth rate on the spatial distribution of droplets in the solidification microstructure. Reprinted with permission from [61].

The emulsions being meta-stable tend to demix, a process driven by the interfacial tension γ, i.e. the free energy per unit area of liquid-liquid interface. In addition, they can be destabilised upon thawing, leading to a phase separation that is highly undesirable. Thus, they often require stabilisation by surfactants or solid particles which adsorb onto the liquid-liquid interface and limit phase separation [72]. The interaction mechanisms between the droplets and the solidification front could be compared to those encountered in bubbles. The similarities arise from an expected deformation and the presence of a temperature-concentration dependent interfacial tension. However, the realistic food emulsions are quite complex and consist of several components including various solutes. Thus, fundamental work on model emulsion systems was certainly required to understand the interactions in these systems.

The directional freezing of monodisperse oil-in-water emulsions to comprehend the droplet-front interactions was performed by Dedovets *et al.* [61] in LSFC. The study observed the impact of solute (surfactant added to stabilise the emulsion) on the behaviour of oil droplets near an ice-water interface. They deduced that the development of the solidification microstructure was controlled by the solute effects; observing droplet motion at typical distances of the order of $\approx 100\ \mu m$. Therefore, the authors further suggested the presence of long-range solute forces in contrast to the short-range intermolecular forces discussed previously. Moreover, the presence of solute premelted films between the droplet and the growing ice crystal as well as in the frozen ice phase was also reported (see Fig.1.37). In conclusion, the study suggested that the freezing behaviour of oil-in-water emulsions could be a analogue of many solidification systems where objects interact with a solidification interface.

The interaction of soft objects is thus relevant to many situations and their behaviour is closely related to the description of hard objects interacting with a solidification front. Although the experimental and theoretical investigation of the soft object systems is much less developed in contrast to the hard particles. Thus, the lack of attention to this domain and the study from Dedovets *et al.* [61] was the motivation for the work carried out on freezing emulsions during this thesis.

1.7 Towards complex...more realistic...systems

The existing theories and experimental evidences have been primarily derived for isolated, hard, and smooth spherical objects, whereas most real-life applications involve multiple particles with arbitrary shapes and surface roughness. In realistic systems, the complex nature of the object interactions is increased owing to a higher concentration of the suspended particles. Furthermore, the idealistic assumptions of the theoretical models such as the non-retarded van der Waals forces, absence of solute segregation, and a *steady-state* planar front interaction are difficult to achieve practically [23]. The transition from a planar to a dendritic front morphology owing to a high particle concentration in composites has been reported theoretically [45, 73]. Progress in studying the spatial distribution, when thousands of particles interact with a solid-liquid front, has been brought about by modern advanced *in situ* imaging techniques, such as X-ray imaging [74], confocal microscopy [60], or the development of numerical modelling techniques, such as molecular dynamics [75, 76]. However, the underlying questions concerning the evolution of solidified microstructure with the associated complex front morphology remain unresolved.

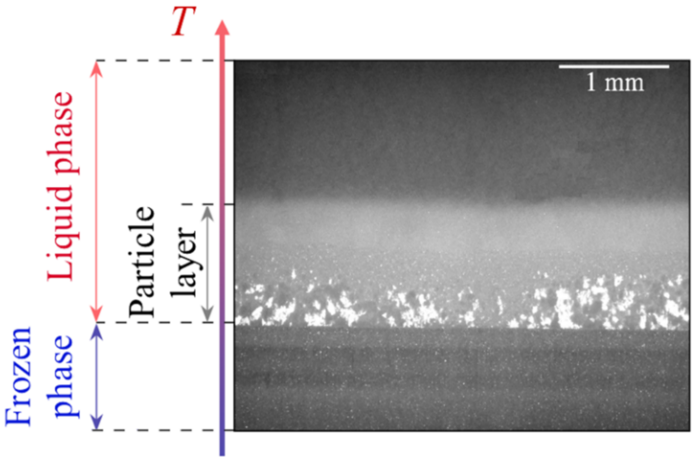

Figure 1.38: Interaction of multiple particles with a solidification front. A compacted particle layer is built-up ahead of the front at a growth rate of $3\ \mu m \cdot s^{-1}$ owing to the particle rejection. Reproduced from [77].

The complex scenario of multiple particles can be partly understood by building on the single-particle models. Isolated particles are rejected at the solid-liquid interface when the growth rate is lower than the critical velocity ($V_{sl} < V_c$). In real-life systems, the particles being pushed get accumulated ahead of the front and eventually interact with the other particles, thereby forming a dense particle layer (see Fig.1.38). The thickness of the particle layer grows until a force equilibrium, similar to isolated systems ($F_\eta = F_\sigma$), is reached. Recently, Saint-Michel *et al.* [77] have proposed a mechanical model to understand these effects of multiple particle interactions on particle trapping by a solidification front. Their study highlights the major differences in the force equilibrium when considering a multi-particle approach. The model suggests that the accumulated particle layer acts as a porous medium and offers resistance to the fluid flow resulting in an additional frictional force (F_μ), which facilitates particle engulfment. Hence, the modified force equilibrium for multiple-particles can be given as $F_\eta + F_\mu = F_\sigma$. Thus, this reinforces the importance of investigating experimentally the role of particle size distribution, particle-particle interactions and hence, the formation of agglomerates.

1.8 Current issues and challenges

In this chapter, we have seen the theoretical background explaining the different isolated object-front interaction models and the definition of the governing equations. I have invoked the various solidification mechanisms, parameters, and features, which influence the behaviour of an individual foreign object in the vicinity of an advancing solidification front. I have also presented a detailed description of the available experimental techniques and their corresponding advantages or limitations in observing the solidification features of interest. Furthermore, the accord as well as the contrasts in the experimental studies and the theoretical predictions were presented. Finally, the complex nature of the realistic systems where multiple objects can additionally interact among themselves was introduced.

The dynamics of interfaces and objects, although an essential aspect of these phenomena, remains extremely difficult to study experimentally. The typical time scale (growth rate of a few $\mu m \cdot s^{-1}$) and space resolution (particles of a few micrometers) make an *in situ* characterization almost impossible with the current approaches. To these difficulties can be added the high temperature required for most materials undergoing solidification, especially in the case of metals and single crystals. Furthermore, many of these phenomena occur in the presence of solutes (or impurities), which can segregate at the interface during the growth of a solid. The resulting solute gradients sometimes play an essential role, while their characterization *in situ* remains problematic. Moreover, the existing theories and experimental evidences have been primarily derived for isolated, hard, and smooth spherical objects, whereas most real-life applications involve multiple particles with arbitrary shapes and surface roughness.

Much of the progress in the domain of object-front interactions has been achieved through numerical simulations and post-solidification analysis [48, 78]. *In situ* experimental evidence of solidification dynamics has been facilitated using transparent analogs with optical microscopes at ambient temperatures [50, 52]. However, the use of an optical microscope does not permit three-dimensional imaging, an essential criterion to comprehend these complex phenomena. Moreover, it can be difficult to distinguish the various phases present such as the solid crystals, secondary objects, and solutes (or dopants). Recently, X-ray transmission microscopy has been employed for the *in situ* evaluation of object-front interactions at elevated temperatures [42, 53]. However, the spatial resolution remains limited and barely sufficient to image the object interactions owing to a low acquisition frequency. In addition, a visualization of the local solute segregation is still lacking. Hence, the tracking of microstructures where objects interact with an advancing solid-liquid interface in the presence of solute effects remains challenging.

1.9 Scope of the thesis

This doctoral thesis has been written as a compendium of several shorter scientific or academic papers. Therefore, the chapters 2, 3, and 4 are written to respond independently to the different aspects of the existing problems as described over the course of chapter 1.

In chapter 2, we start by studying the simplest system where an isolated object interacts with an approaching ice-water interface, using cryo-confocal microscopy. The objective is to visualize the actual front geometry when an object approaches a solid-liquid interface and correlate the findings to the existing literature. We demonstrate the complete shape of the planar front curvature, for hard particles and soft objects, having a thermal conductivity mismatch with the pure melt. We then compare our experimental data with the theoretical predictions from the Park *et al.* [32] model, and discuss the distortion of the temperature field in the vicinity of a foreign object. We further explore the role of solute and depict the modifications to the expected front geometry, using the same set of objects, owing to the solute effects. We also report on the impact of object-melt thermal conductivity mismatch for cellular front morphology. We note the dominating effect of solute and discuss its impact on the formation of a thick premelted film. We thus show experimentally the formation of a premelted film and distinguish between the object-front interactions in pure melts and in solute solutions.

In chapter 3, the interaction of spherical oil droplets with a planar ice-water interface is investigated. We demonstrate the systematic influence of three solidification parameters, namely the bulk solute concentration, the growth rate, and the object size, on monodisperse oil-in-water emulsions subjected to directional solidification. The use of soft objects is also to provide insights into the mechanisms at play when a deformable object encounters a solidification front. We first study the *in situ* solidification dynamics of the droplets in water, far from the solidification front. We measure the typical distance at which the droplets start feeling the presence of an advancing interface and their consequent displacement owing to their dynamic interaction. We compare our results and discuss the observed disparities with the previous theoretical models. We then characterise the deformation of the droplets and depict their shape evolution as they are hit by the approaching solidification front. We attempt to understand the distinct deformation regimes observed and try to relate it to the presence of a solute-enriched premelted film. As the droplets get engulfed in ice, we report on the dynamic evolution of premelted films and show a droplet deformation unlike the previous observations. The study highlights the dramatic impact of an increasing bulk solute concentration and the absence of theoretical models incorporating such effects.

Finally, in chapter 4, we try to bridge the gap between an ideal isolated object regime and the complex realistic systems, by experimentally studying the interaction of multiple objects with a solid-liquid interface. The goal is to elucidate an *in situ* development of a material microstructure in the presence of particle-particle interactions and solute effects. We use oil-in-water emulsions as a simplified model analogue system to understand the diverse interactions possible in a complex system. To perform a systematic analysis, we start with a monodisperse oil-in-water emulsion and study the influence of two solidification parameters; droplet size and bulk solute concentration. A modification of the force dynamics following the development of agglomerates, owing to the high particle concentration of the suspension, is depicted experimentally. We then discuss the current theoretical understanding of multiple-particle interactions with regards to engulfment and repulsion, by building on the predictions of the isolated object models. We further demonstrate the solidification of bimodal emulsions, where two colonies of droplets with distinct radii are mixed together. The influence of an increasing bulk solute concentration is equally investigated with bimodal emulsions. To imitate a realistic situation more closely, we finally investigate the interaction of polydisperse oil droplets and note the formation of droplet clusters. The study helps in visualizing the evolution of complex relevant microstructures, in the presence and absence of solute effects, which are difficult to predict theoretically.

Bibliography

[1] Arturo E Corte. Vertical migration of particles in front of a moving freezing plane. *Journal of Geophysical Research*, 67(3):1085–1090, 1962.

[2] R. Asthana and S. N. Tewari. The engulfment of foreign particles by a freezing interface. *Journal of Materials Science*, 28(20):5414–5425, 1993.

[3] D. R. Uhlmann, B. Chalmers, and K. A. Jackson. Interaction between particles and a solid-liquid interface. *Journal of Applied Physics*, 35(10):2986–2993, 1964.

[4] D. Shangguan, S. Ahuja, and D. M. Stefanescu. An analytical model for the interaction between an insoluble particle and an advancing solid/liquid interface. *Metallurgical Transactions A*, 23(2):669–680, 1992.

[5] SN Omenyi and AW Neumann. Thermodynamic aspects of particle engulfment by solidifying melts. *Journal of Applied Physics*, 47(9):3956–3962, 1976.

[6] SN Omenyi, AW Neumann, and CJ Van Oss. Attraction and repulsion of solid particles by solidification fronts i. thermodynamic effects. *Journal of Applied Physics*, 52(2):789–795, 1981.

[7] Patrick François Aubourg. *Interaction of second-phase particles with a crystal growing from the melt.* PhD thesis, Massachusetts Institute of Technology, 1978.

[8] Jürgen Pötschke and Volker Rogge. On the behaviour of foreign particles at an advancing solid-liquid interface. *Journal of Crystal Growth*, 94(3):726–738, 1989.

[9] Doru M. Stefanescu, B. K. Dhindaw, S. A. Kacar, and A. Moitra. Behavior of ceramic particles at the solid- liquid metal interface in metal matrix composites. *Metallurgical Transactions A*, 19(11):2847–2855, 1988.

[10] AA Chernov, DE Temkin, and AM Mel'Nikova. Theory of the capture of solid inclusions during the growth of crystals from the melt. *Sov. Phys. Crystallogr*, 21(4):369–373, 1976.

[11] R. Sasikumar and T. R. Ramamohan. Distortion of the temperature and solute concentration fields due to the presence of particles at the solidification front-effects on particle pushing. *Acta Metallurgica Et Materialia*, 39(4):517–522, 1991.

[12] J. K. Kim and P. K. Rohatgi. The effect of the diffusion of solute between the particle and the interface on the particle pushing phenomena. *Acta Materialia*, 46(4):1115–1123, 1998.

[13] L. Hadji. Morphological instability induced by the interaction of a particle with a solid-liquid interface. *European Physical Journal B*, 37(1):85–89, 2004.

[14] AA Chernov, DE Temkin, and AM Mel'Nikova. The influence of the thermal conductivity of a macroparticle on its capture by a crystal growing from a melt. *Sov. Phys. Crystallogr*, 22(6):656–658, 1977.

[15] C Körber. Phenomena at the advancing ice-liquid interface: solutes, particles and biological cells. *Quarterly reviews of biophysics*, 21:229–298, 1988.

[16] BV Derjaguin and M Kussakov. Anomalous properties of thin polymolecular films. *Acta Physicochim. URSS*, 10(1):25–44, 1939.

[17] R Lipowsky. Nonlinear growth of wetting layers. *Journal of Physics A: Mathematical and General*, 18(10):L585, 1985.

[18] Yoshinori Furukawa, Masaki Yamamoto, and Toshio Kuroda. Ellipsometric study of the transition layer on the surface of an ice crystal. *Journal of crystal growth*, 82(4):665–677, 1987.

[19] Evgenni Mikhailovich Lifshitz, M Hamermesh, et al. The theory of molecular attractive forces between solids. In *Perspectives in Theoretical Physics*, pages 329–349. Elsevier, 1992.

[20] A. W. Rempel and M. G. Worster. Particle trapping at an advancing solidification front with interfacial-curvature effects. *Journal of Crystal Growth*, 223(3):420–432, 2001.

[21] JS Wettlaufer and M Grae Worster. Premelting dynamics. *Annu. Rev. Fluid Mech.*, 38:427–452, 2006.

[22] JS Wettlaufer, MG Worster, LA Wilen, and JG Dash. A theory of premelting dynamics for all power law forces. *Physical review letters*, 76(19):3602, 1996.

[23] Sylvain Deville. *Freezing colloids: observations, principles, control, and use: applications in materials science, life science, earth science, food science, and engineering.* Springer, 2017.

[24] JG Dash, Haiying Fu, and JS Wettlaufer. The premelting of ice and its environmental consequences. *Reports on Progress in Physics*, 58(1):115, 1995.

[25] Julia Schollick. *Real space study of pattern formation in freezing colloidal suspensions.* PhD thesis, University of Oxford, 2012.

[26] J. G. Dash, A. W. Rempel, and J. S. Wettlaufer. The physics of premelted ice and its geophysical consequences. *Reviews of Modern Physics*, 78(3):695–741, 2006.

[27] Navaneeth K. Marath and J. S. Wettlaufer. Impurity effects in thermal regelation. *Soft Matter*, 16(25):5886–5891, 2020.

[28] Gregory A Zielinski and Grant R Mershon. Paleoenvironmental implications of the insoluble microparticle record in the gisp2 (greenland) ice core during the rapidly changing climate of the pleistocene–holocene transition. *Geological Society of America Bulletin*, 109(5):547–559, 1997.

[29] A. W. Rempel, J. S. Wettlaufer, and M. G. Worster. Interfacial Premelting and the Thermomolecular Force: Thermodynamic Buoyancy. *Physical Review Letters*, 87(8):088501, 2001.

[30] A. W. Rempel and M. G. Worster. Interaction between a particle and an advancing solidification front. *Journal of Crystal Growth*, 205(3):427–440, 1999.

[31] Yutao Tao, Andrew Yeckel, and Jeffrey J. Derby. Steady-state and dynamic models for particle engulfment during solidification. *Journal of Computational Physics*, 315:238–263, 2016.

[32] Min S. Park, Alexander A. Golovin, and Stephen H. Davis. The encapsulation of particles and bubbles by an advancing solidification front. *Journal of Fluid Mechanics*, 560:415–436, 2006.

[33] Hugo C Hamaker. The london—van der waals attraction between spherical particles. *physica*, 4(10):1058–1072, 1937.

[34] Justin C. T. Kao and Alexander A. Golovin. Particle capture in binary solidification. *Journal of Fluid Mechanics*, 625(September 2008):299, 2009.

[35] Anthony Chang, Jonathan A. Dantzig, Brian T. Darr, and Allison Hubel. Modeling the interaction of biological cells with a solidifying interface. *Journal of Computational Physics*, 226(2):1808–1829, 2007.

[36] Sylvain Deville. Freeze-casting of porous ceramics: a review of current achievements and issues. *Advanced Engineering Materials*, 10(3):155–169, 2008.

[37] Lifeng Zhang. Nucleation, growth, transport, and entrapment of inclusions during steel casting. *Jom*, 65(9):1138–1144, 2013.

[38] Guoping Du, Nan Chen, and Pietro Rossetto. On-wafer investigation of sic and si3n4 inclusions in multicrystalline si grown by directional solidification. *Solar energy materials and solar cells*, 92(9):1059–1066, 2008.

[39] Doru Michael Stefanescu. *Science and engineering of casting solidification*. Springer, 2015.

[40] Kenji Yoshimura, Takaaki Inada, and Shigeru Koyama. Growth of spherical and cylindrical oxygen bubbles at an ice- water interface. *Crystal Growth and Design*, 8(7):2108–2115, 2008.

[41] W. A. Tiller, K. A. Jackson, J. W. Rutter, and B. Chalmers. The redistribution of solute atoms during the solidification of metals. *Acta Metallurgica*, 1(4):428–437, 1953.

[42] Adrian V. Catalina, Subhayu Sen, Doru M. Stefanescu, and William F. Kaukler. Interaction of porosity with a planar solid/liquid interface. *Metallurgical and Materials Transactions A*, 35(5):1525–1538, 2004.

[43] W. W. Mullins and R. F. Sekerka. Stability of a planar interface during solidification of a dilute binary alloy. *Journal of Applied Physics*, 35(2):444–451, 1964.

[44] Mark Alan Eshelman. Solidification Dynamics in Binary Alloy Systems. *PhD Thesis, Iowa State University*, 1987.

[45] B. Dutta and M. K. Surappa. Directional dendritic solidification of a composite slurry: Part I. Dendrite morphology. *Metallurgical and Materials Transactions A: Physical Metallurgy and Materials Science*, 29(4):1319–1327, 1998.

[46] VL Bronstein, YA Itkin, and GS Ishkov. Rejection and capture of cells by ice crystals on freezing aqueous solutions. *Journal of Crystal Growth*, 52:345–349, 1981.

[47] Yi Yang, JW Garvin, and HS Udaykumar. Sharp interface numerical simulation of directional solidification of binary alloy in the presence of a ceramic particle. *International journal of heat and mass transfer*, 51(1-2):155–168, 2008.

[48] E. A. Ghezal, H. Li, A. Nehari, G. Alombert-Goget, A. Brenier, K. Lebbou, M. F. Joubert, and M. T. Soltani. Effect of pulling rate on bubbles distribution in sapphire crystals grown by the micropulling down (μ-PD) technique. *Crystal Growth and Design*, 12(8):4098–4103, 2012.

[49] U. Hecht and S. Rex. On the transition from pushing to engulfment during directional solidification of the particle-reinforced aluminum-based metal-matrix composite 2014 + 10 Vol Pct Al2O3. *Metallurgical and Materials Transactions A: Physical Metallurgy and Materials Science*, 28(13):867–874, 1997.

[50] J. A. Sekhar and R. Trivedi. Solidification microstructure evolution in the presence of inert particles. *Materials Science and Engineering A*, 147(1):9–21, 1991.

[51] Dongkai Shangguan and Doru M. Stefanescu. In situ observation of interactions between gaseous inclusions and an advancing solid/liquid interface. *Metallurgical Transactions B*, 22(3):385–388, 1991.

[52] H. Jamgotchian, R. Trivedi, and B. Billia. Interface dynamics and coupled growth in directional solidification in presence of bubbles. *Journal of Crystal Growth*, 134(3-4):181–195, 1993.

[53] S. Sen, W. F. Kaukler, P. Curreri, and D. M. Stefanescu. Dynamics of solid/liquid interface shape evolution near an insoluble particle - An X-ray transmission microscopy investigation. *Metallurgical and Materials*

Transactions A: Physical Metallurgy and Materials Science, 28(10):2129–2135, 1997.

[54] Sylvain Deville, Jérôme Adrien, Eric Maire, Mario Scheel, and Marco Di Michiel. Time-lapse, three-dimensional in situ imaging of ice crystal growth in a colloidal silica suspension. *Acta Materialia*, 61(6):2077–2086, 2013.

[55] Hiroshi Ishiguro and Boris Rubinsky. Mechanical interactions between ice crystals and red blood cells during directional solidification. *Cryobiology*, 31(5):483–500, oct 1994.

[56] Liat Bahari, Amir Bein, Victor Yashunsky, Vera Sirotinskaya, and Ido Braslavsky. Cryopreservation of adherent mammalian cells on substrate by slow freezing. *Cryobiology*, 80:160, 2018.

[57] Ch Körber, S. Englich, P. Schwindke, M. W. Scheiwe, G. Rau, A. Hubel, and E. G. Cravalho. Low temperature light microscopy and its application to study freezing in aqueous solutions and biological cell suspensions. *Journal of Microscopy*, 141(3):263–276, 1986.

[58] Moreno Marcellini, Cecile Noirjean, Dmytro Dedovets, Juliette Maria, and Sylvain Deville. Time-Lapse, in Situ Imaging of Ice Crystal Growth Using Confocal Microscopy. *ACS Omega*, 1(5):1019–1026, 2016.

[59] Dmytro Dedovets, Cécile Monteux, and Sylvain Deville. A temperature-controlled stage for laser scanning confocal microscopy and case studies in materials science. *Ultramicroscopy*, 195(August):1–11, 2018.

[60] Dmytro Dedovets, Cécile Monteux, and Sylvain Deville. A temperature-controlled stage for laser scanning confocal microscopy and case studies in materials science. *Ultramicroscopy*, 195(August):1–11, 2018.

[61] Dmytro Dedovets, Cécile Monteux, and Sylvain Deville. Five-dimensional imaging of freezing emulsions with solute effects. *Science*, 360(6386):303–306, 2018.

[62] Kankan Qin, Corentin Eschenbrenner, Félix Ginot, Dmytro Dedovets, Thibaud Coradin, Sylvain Deville, and Francisco M Fernandes. Unveiling cells' local environment during cryopreservation by correlative in situ spatial and thermal analyses. *J. Phys. Chem. Lett.*, 2020.

[63] AM Zubko, VG Lobanov, and V V_ Nikonova. Reaction of foreign particles with a crystallization front. *Sov. Phys. Crystallogr.*, 18(2):239–241, 1973.

[64] AK Gupta, BK Saxena, SN Tiwari, and SL Malhotra. Pore formation in cast metals and alloys. *Journal of materials science*, 27(4):853–862, 1992.

[65] Peter Mazur. Freezing of living cells: mechanisms and implications. *American journal of physiology-cell physiology*, 247(3):C125–C142, 1984.

[66] P. S. Wei, C. C. Huang, and K. W. Lee. Nucleation of bubbles on a solidification front - Experiment and analysis. *Metallurgical and Materials Transactions B: Process Metallurgy and Materials Processing Science*, 34(3):321–332, 2003.

[67] P. S. Wei, C. C. Huang, Z. P. Wang, K. Y. Chen, and C. H. Lin. Growths of bubble/pore sizes in solid during solidification - An in situ measurement and analysis. *Journal of Crystal Growth*, 270(3-4):662–673, 2004.

[68] Norikazu MAENO. Air bubble formation in ice crystals. *Physics of Snow and Ice: proceedings*, 1(1):207–218, 1967.

[69] Zhe Wang, Kusuhiro Mukai, and In Jae Lee. Behavior of fine bubbles in front of the solidifying interface. *ISIJ international*, 39(6):553–562, 1999.

[70] Supratim Ghosh and John N Coupland. Factors affecting the freeze–thaw stability of emulsions. *Food Hydrocolloids*, 22(1):105–111, 2008.

[71] M Shafiur Rahman. *Handbook of food preservation*. CRC press, 2007.

[72] Bernard P Binks and Tommy S Horozov. *Colloidal particles at liquid interfaces*. Cambridge University Press, 2006.

[73] B. Dutta and M. K. Surappa. Directional dendritic solidification of a composite slurry: Part II. Particle distribution. *Metallurgical and Materials Transactions A: Physical Metallurgy and Materials Science*, 29(4):1329–1339, 1998.

[74] Melissa Spannuth, SGJ Mochrie, SSL Peppin, and JS Wettlaufer. Particle-scale structure in frozen colloidal suspensions from small-angle x-ray scattering. *Physical review E*, 83(2):021402, 2011.

[75] Florian Bouville, Eric Maire, and Sylvain Deville. Self-assembly of faceted particles triggered by a moving ice front. *Langmuir*, 30(29):8656–8663, 2014.

[76] Stephen A Barr and Erik Luijten. Structural properties of materials created through freeze casting. *Acta materialia*, 58(2):709–715, 2010.

[77] Brice Saint-Michel, Marc Georgelin, Sylvain Deville, and Alain Pocheau. Interaction of Multiple Particles with a Solidification Front: From Compacted Particle Layer to Particle Trapping. *Langmuir*, 33(23):5617–5627, 2017.

[78] P. S. Wei and S. Y. Hsiao. Pore shape development from a bubble captured by a solidification front. *International Journal of Heat and Mass Transfer*, 55(25-26):8129–8138, 2012.

Chapter 2

Objects interacting with solidification fronts: Thermal conductivity effects

Abstract

Objects, such as droplets, bubbles, or particles, interact with a moving solidification front in several material processing routes. The consequences of this confrontation, varying from instantaneous engulfment to complete rejection of suspended objects, regulates the solidified microstructure and thus, the functional properties of the material. In this study, we utilize *in situ* cryo-confocal microscopy to investigate the interplay between thermal conductivity mismatch (of the object and the melt) and the role of solute, which both impact the geometry of the ice-water solidification front in different manners. First, we experimentally validate the theoretical predictions of physical models on the distortion of thermal fields in the presence of foreign objects. Subsequently, we report on the dominating effect of solute on the front curvature with the dynamic evolution of premelted films. In the case of cellular front morphology, we depict that particles with a lower thermal conductivity than water induce a distortion of the encircling ice crystals, thereby modifying the final microstructure of the solid. Finally, our results demonstrate that to successfully predict and control the solidification microstructure, in the presence of objects, physical models incorporating both thermal and long-range solute effects are required.

Keywords: solidification, solutes, thermal conductivity, interfacial curvature,

microstructure

2.1 Introduction

The interaction of solidification fronts with objects (droplets, bubbles, solid particles or biological cells) is a common phenomenon encountered in a plethora of situations, ranging from industrial to natural occurrences, such as the formation of sea ice, growth of single crystals, metallurgy, cryobiology, or food science. The objects (soft or hard) exhibit different types of behavior while interacting with a solidification front, from total rejection to complete or partial engulfment [1]. The dynamics of this interaction influences the solidified microstructure and the mechanical and functional properties of the materials. From homogeneous particle distribution in particle-reinforced metal matrix composites to complete rejection of inclusions or porosity management in castings and growth of single crystals, distinct outcomes may be desired depending on the application. The potential to actively govern the solidification microstructure is thus crucial.

The first experiments on the interaction of particles with a solidifying ice-water front were performed by Corte [2] for geological applications. Uhlmann *et al.* [3] established a criterion of critical velocity (V_c), for a given size of an insoluble object, to predict whether the object will be engulfed ($V_{sl} > V_c$) or rejected ($V_{sl} < V_c$), by a freezing front moving at a velocity V_{sl}. Their thin film approach to investigate the engulfment and rejection of particles considered the change in chemical potential of the liquid in the particle-front gap (repulsive) and the viscous drag forces (attractive) to deduce the particle behaviour. The analytical models, utilizing the Uhlmann *et al.* approach, derive the critical engulfment velocity (V_c) as the maximum particle velocity when the particle-front gap (d) is minimized and assumed equivalent to a few molecular diameters ($d \leq 10\,nm$) [4, 5, 6]. However, these models involve parameters such as change in interfacial energy (solid-object) which are difficult to determine experimentally, and consider idealized planar front geometry in the presence of particles [1].

Chernov *et al.* [7, 8] suggested that the particle behaviour in vicinity of a solidifying front is governed by an interplay between repulsive van der Waals and attractive viscous drag forces. Their study, assuming a paraboloid frontal shape, was the first to consider distortion of the temperature field owing to the differing thermal conductivities of the particle and the melt ($k_p \neq k_m$). They demonstrated that the shape of the solidification front plays a major role in solidification dynamics as it influences the magnitude of viscous drag forces in the gap (d) between the particle and the front, depicted by model sketch in Fig.2.1. Theoretically, the critical velocity reduces drastically for concave shaped fronts as opposed to ideal planar fronts [6, 9, 10, 11]. Hence, the approach from Chernov *et al.* is generally accepted and used in most models as the presence of a particle distorts the shape of an approaching solid-liquid front.

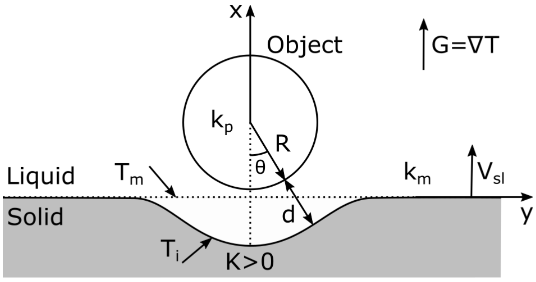

Figure 2.1: Objects interacting with a moving solidification front: principles. Model sketch, where d is the particle-front gap, G is the temperature gradient, K is the interfacial front curvature (here > 0 for concave geometry), k_p, k_m are the thermal conductivity of the particle and melt respectively, R is the object radius, T_m is the absolute melting temperature, T_i is the solid-liquid front temperature, and V_{sl} is the solidification velocity. © (2020) S. Tyagi *et al.* (10.6084/m9.figshare.12046560) CC BY 4.0 license https://creativecommons.org/licenses/by/4.0/.

Rempel *et al.* [12, 13] used the Chernov *et al.* approach and made significant improvements to the existing analytical models by including the Gibbs-Thomson effect to predict the entire shape of the front. Their model equates the repulsive disjoining forces, originating from inter-molecular interactions, to the attractive viscous forces, emanating from the fluid flow around the particle calculated using a lubrication approximation. The study formulated an analytical relationship for the critical engulfment velocity with the various process parameters such as size of particle (R), temperature gradient (G), and type of inter-molecular interactions. However, the front shape is predicted by assuming equal thermal conductivity of the particle (k_p) and melt (k_m).

A similar approach of thin-film lubrication approximation was used by Park *et al.* [14], while incorporating the effects of thermal conductivity difference ($k_p/k_m = [-1,1]$). This is important as the difference in thermal conductivity between the particle and the melt should deform the front 10^3 times more than the other parameters [14]. Moreover, the front geometry is the key to determining the forces on the particle and hence predict the particle behaviour [5, 6, 8, 10, 15]. An object with a different thermal conductivity from the melt will modify the local heat flow, thereby altering the isotherms locally. As we assume the solid-liquid front to follow the isotherm for the melting point of the matrix material, this difference of thermal conductivity can bend the front towards or away from the object, depending on whether the thermal conductivity of the object is higher or lower than the melt. The previous studies have thus often suggested that if a particle has a lower thermal conductivity than the melt ($k_p/k_m < 1$), the solidification front bulges towards the object and may repel it. In the opposite case ($k_p/k_m > 1$), the solidification front bends away from the particle and facilitates its engulfment [5, 6, 16].

The thermal conductivity ratio criterion is not extensive and has been modified in certain experimental predictions of repulsion and engulfment of foreign particles [17]. Few in-situ experimental observations exist to ratify these analytical predictions, owing to the associated small time and space scales, as well as high temperatures of solidification, especially for metals [18, 19, 20, 21, 22]. Yemmou *et al.* [19] presented the first experimental evidence of convex and concave geometries, using an ice-water system, with large ($diameter > 0.3\,cm$) Nylon and stainless steel particles. Subsequently, the real-time evolution of solidification front curvature was reported for $500\,\mu m\, ZrO_2$ particles in metal matrix composites by Sen *et al.* [21], using X-ray transmission microscopy.

The presence of solute (desired or as an impurity) in the melt may also influence the interaction between a particle and a solidification front, as solutes are rejected by the solid (with low partition coefficient) and segregate at the solid-melt interface, leading to a colligative depression of the melting temperature [7, 9, 10]. The high concentration of solute is further enhanced by the obstruction of solute diffusion away from the front in presence of an insoluble object [15]. The shape of the front conforms to the local solute concentration and hence a concave curvature is predicted by the previous studies [9, 10, 15, 23, 24]. Catalina *et al.* [22] have depicted schematically the change in shape and local solutal segregation in the presence of gas porosity using X-ray transmission microscopy with metallic systems.

Here, we study in a systematic manner the influence of the thermal conductivity of the object on the ice-water solidification front curvature using *in situ* cryo-confocal microscopy. We report on the front shape evolution using soft objects and rigid particles, representing an extensive range of thermal conductivity ratio ($0.04 \leq k_p/k_m \leq 35$). Our custom experimental setup enables us to study the solidification dynamics with a small time step size ($t = 1.7\,s$) in conjunction with rejected solutes visualization. Using laser-induced fluorescence, we depict experimentally the local solute segregation and the corresponding solidification front geometry. We suggest that solute segregation at the front overrides the effects of thermal conductivity mismatch (k_p/k_m) and hence, not only controls the front curvature but also the dynamics of particle capture. Finally, we demonstrate for the first time a distortion of ice crystals, surrounding engulfed thermally insulating particles, due to persisting local temperature gradients in the case of cellular front morphology. Thus, we report on the interplay between solute and thermal conductivity effects, in presence of foreign objects, responsible for modifying the microstructure of a solidified matrix.

2.2 Materials and methods

We perform solidification experiments with dilute aqueous dispersions of droplets, bubbles, and particles, of similar diameter $\approx 50\,\mu m$, but varying thermal conductivity ($0.04 \leq k_p/k_m \leq 35$). We regulate the solidification front velocity (V_{sl}) by translating a Hele-Shaw cell, under a confocal laser scanning microscope, along a temperature gradient (G) imposed by two Peltier modules, as shown in Fig. 2.2. The independent selection of the two parameters (V_{sl} & G) in our setup enables a uniform cooling rate and an improved control over the front morphology, compared to the setups where the sample is frozen either at a constant temperature or at a constant cooling rate. In this study, we performed the solidification experiments at a constant front velocity (V_{sl}) with a stable linear temperature gradient (G).

2.2.1 Materials

Propyl benzoate, TWEEN80, Difluoro2-[1-(3,5-dimethyl-2H-pyrrol-2-ylidene-N)ethyl]-3,5-dimethyl-1H-pyrrolato-Nboron (BODIPY), and Sulforhodamine B (SRhB) were obtained from Sigma-Aldrich. Zirconia (ZrO_2) particles (Zirmil Y from Saint-Gobain ZirPro, $50-63\,\mu m$) were provided by Saint-Gobain Research Provence. We purchased fluorescent green polyethylene ($1\,g\cdot cm^{-3}$, $45-53\,\mu m$) and stainless steel ($7\,g\cdot cm^{-3}$, $48-57\,\mu m$) microspheres from Cospheric LLC. We ordered monodisperse green-fluorescent polystyrene ($48.1\,\mu m$) and poly(methyl methacrylate) (PMMA) ($50.3\,\mu m$) from Micro Particles GmbH. Deionized water, filtered with $0.45\,\mu m$ Nylon membrane filters (VWR International), was used for the aqueous phase. The thermal and geometrical parameters which were important for our study are given in table 2.1. The material properties have values based on their typical conditions at $25\,°C$ and 1 atm.

Particle	R (m)	k_p $(W\cdot m^{-1}\cdot K^{-1})$	k_p/k_m
Air	27×10^{-6}	0.026	0.046
Polystyrene (PS)	24×10^{-6}	0.030 - 0.040	0.052 - 0.070
Propyl benzoate (PB)	28×10^{-6}	0.141	0.248
PMMA	25×10^{-6}	0.167 - 0.250	0.293 - 0.439
Polyethylene (PE)	26×10^{-6}	0.500	0.879
Zirconia (ZrO_2)	28×10^{-6}	1.7 - 2.7	2.988 - 4.745
Stainless steel (SS)	28×10^{-6}	20.0	35.149

Table 2.1: Radius (R), thermal conductivity of the materials (k_p) and their ratio with the aqueous phase (k_p/k_m), where $k_m = 0.569\,W\cdot m^{-1}\cdot K^{-1}$.

2.2.2 Sample Preparation

The oil-in-water emulsions were prepared by using a microfluidic setup (microfluidic starter kit, Micronit Microfluidics, Netherlands) with pressure controlled flow pumps (Fluigent LineUP Flow EZ) and uncoated focused flow droplet generator chips (FF_DROP), with a nozzle diameter of $50\,\mu m$. The flow rate of oil and aqueous phases were controlled using Fluigent Flow Unit S ($0-7\,\mu L\cdot min^{-1}$). The oil phase consisted of propyl benzoate with $10^{-4}\,M$ BODIPY, and the aqueous phase was a $10^{-5}\,M$ SRhB solution. The air-in-water foams were prepared by using the double syringe technique [25], with a luer adapter as connective, and a liquid fraction of 50 %. For the foams, we bubbled air through liquid perfluorohexane (C_6F_{14} 98+%, Alfa Aesar) to obtain a gas composed of air and perfluorohexane vapour. Thus, we could delay coarsening [26] and ensure the bubbles remained stable during the experimental time-scales, typically varying from 4 to 6 hours at $V_{sl} = 10^{-6}\,m\cdot s^{-1}$. TWEEN80 was used as a non-ionic surfactant and solute to avoid long-range electrostatic interactions. We used the same surfactant for stabilising both the oil-in-water emulsions and the air-in-water foams. The particle suspensions were thoroughly sonicated ($30-40\,min$) to ensure a homogeneous dispersion. The experiments in the presence of solute were carried out by adding $1\,wt.\%$ TWEEN80 to the aqueous phase. We used the same solute and concentration for all systems to ensure comparable results. The solutions were frozen in a rectangular Hele-Shaw cell ($height = 100\,\mu m$ and $volume = 100\,\mu L$), fabricated using two glass slides (Menzel, $24 \times 60\,mm$, thickness $0.13-0.16\,mm$), and sealed with nail-polish at one end to avoid evaporation. We do not observe convection effects in our experiments as they are performed in a closed Hele-Shaw cell of small thickness ($100\,\mu m$) and at low solidification velocity of $1\,\mu m \cdot s^{-1}$ with a steady linear temperature gradient of $10^4\,K \cdot m^{-1}$.

2.2.3 Freezing Stage

We performed directional freezing experiments, translating the sample along a constant linear temperature gradient of $10^4\,K \cdot m^{-1}$, using the cryo-confocal stage described previously [27]. We carried out all of the experiments at a solidification front velocity $V_{sl} = 10^{-6}\,m \cdot s^{-1}$, unless stated otherwise. The solidification front tends to appear immobile in the frame of observation, however, in the sample frame, it is the ice solidifying (along $\vec{x}$) at the velocity imposed by the pulling rate of the motor (Micos Pollux Drive VT-80 translation stage PI, USA). We modified the stage by substituting the aluminium plate with a copper serpentine sheet and discarding the silicon carbide honeycomb interface. This led to an improved stability and a more robust cooling setup. The temperature gradient was imposed with two Peltier modules and controlled using TEC-1122 Dual Thermo Electric Cooling Temperature Controller from Meerstetter Engineering, Switzerland. We can thus decouple and control independently the solidification velocity (V_{sl}) and the temperature gradient (G).

2.2.4 Imaging & Analysis

The images were acquired through a Leica TCS SP8 confocal laser scanning microscope (Leica Microsystemes SAS, Germany), equipped with $488\,nm$ (blue) and $552\,nm$ (green) lasers. We utilised the microscope at a scanning speed of $600\,Hertz$, with $1024 \times 1024\,pixels$ for imaging $775 \times 775\,\mu m$, resulting in $1.7\,s$ per frame. The high spatial resolution, coupled with rapid screening, enabled us to observe the dynamics of objects interacting with solidification fronts *in situ*. We used two photodetectors (PMT) to simultaneously image three phases :

1. BODIPY ($\lambda_{ex}\,493\,nm$; $\lambda_{em}\,504\,nm$), the dye incorporated into the oil droplets. The same emission spectrum was utilised to image the fluorescent colloids.

2. SRhB ($\lambda_{ex}\,565\,nm$; $\lambda_{em}\,586\,nm$), dissolved in water, to image the aqueous phase and the cells boundaries in ice.

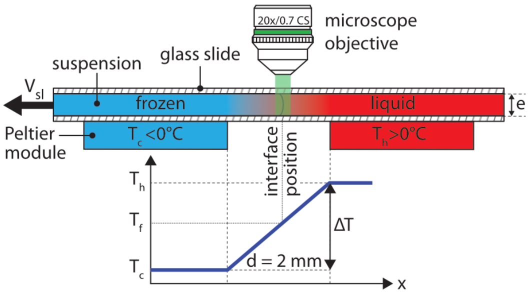

Figure 2.2: Experimental setup for *in situ* solidification experiments. A thin Hele-Shaw cell containing the particles, bubbles, or droplets in suspension is pulled at a constant velocity (V_{sl}) through a constant temperature gradient (G) established by Peltier elements. In steady state, the solidification front is thus at a constant position under the microscope objective.© (2020) S. Tyagi *et al.* (10.6084/m9.figshare.12046560) CC BY 4.0 license https://creativecommons.org/licenses/by/4.0/.

3. Ice does not fluoresce as it has very low solubility for solutes [28] and hence, appears black.

The emission spectra of the excited fluorophores was captured using a non-immersive objective (Leica HCX PL APO CS 20×). The working distance of 590 μm and an insulating foam cover facilitates the minimization of thermal perturbations on the freezing substrate. We used Fiji [29] and Python for image processing and data analysis.

2.2.5 Typical solidification parameters

Parameters	Particle in water
G ($K \cdot m^{-1}$)	1.0×10^4
T$_m$ (K)	273.15
L$_v$ ($J \cdot m^{-3}$)	3.03×10^8
σ_{sl} ($J \cdot m^{-2}$)	3.0×10^{-2}
V_{sl} ($m \cdot s^{-1}$)	1.0×10^{-6}
λ (m)	2.83×10^{-10}

Table 2.2: Typical solidification parameters for an object in front of an ice-water solidification front. L_v, σ_{sl}, and λ adapted from Park *et al.*[14]

2.3 Results and discussion

2.3.1 Thermal conductivity controls the interfacial curvature

We observe a pronounced convex curvature (Fig. 2.3A,B) when the objects have a lower thermal conductivity than water ($k_p/k_m < 1$, see Fig.2.3C) and thus, the front tends to diverge towards them as they act as thermal shields causing the temperature in the gap behind them to be successively lowered. With zirconia (ZrO_2) and stainless steel (SS) particles, we observe a concave cusping of the front (Fig. 2.3B). The relatively higher thermal conductivity of these particles compared to water ($k_p/k_m > 1$, see Fig.2.3C) enables a preferential heat flux from the melt to the front resulting in a concave depression. Thus, the differing thermal conductivities of the particle and melt result in a distortion of the isotherms away from the horizontal, which is in accordance with the previous theoretical and experimental evidence [6, 8, 16, 21]. In contrast, the presence of a polyethylene (PE) particle does not perturb the shape of the ice-water front owing to its magnitude of thermal conductivity being close to that of water ($k_p/k_m = 0.879$, see Fig.2.3B,C). From Fig.2.3B, we notice that the shape of the front in vicinity of a spherical object does not change for an air bubble, liquid oil droplet, or a solid particle. This is owing to the fact that the front curvature depends on the ice-water interfacial tension, disjoining pressure, and the particle to melt thermal conductivity ratio [14]. Hence, we do not expect the surface energy of the objects to play a major role.

These observations are in agreement with the numerical model from Park *et al.* [14]. This model is based on the computation of particle velocity close to the front ($d << R$, see Fig. 2.1) and takes into account the balance of hydrodynamic and intermolecular forces, solidification front surface energy, contrast of the particle and melt thermal conductivities, and the flow caused by the density change upon solidification. In particular, the model encompasses an asymptotic analysis in the lubrication approximation and theoretically predicts the curvature of the front as a function of γ and (k_p/k_m), shown in Fig. 2.4A, where γ is a dimensionless surface energy parameter, $\gamma = (T_m \sigma_{sl})/(L_v G R^2)$, where T_m is the bulk melting temperature at constant pressure, L_v is the latent heat per unit volume of solid, G is the applied temperature gradient, σ_{sl} is the interfacial tension between the solid front and the melt, of the order $3 \times 10^{-2}\, N \cdot m^{-1}$, and R is the radius of the spherical object. Our solidification experiments correspond to $\gamma \approx 3.5 \times 10^{-3}$.

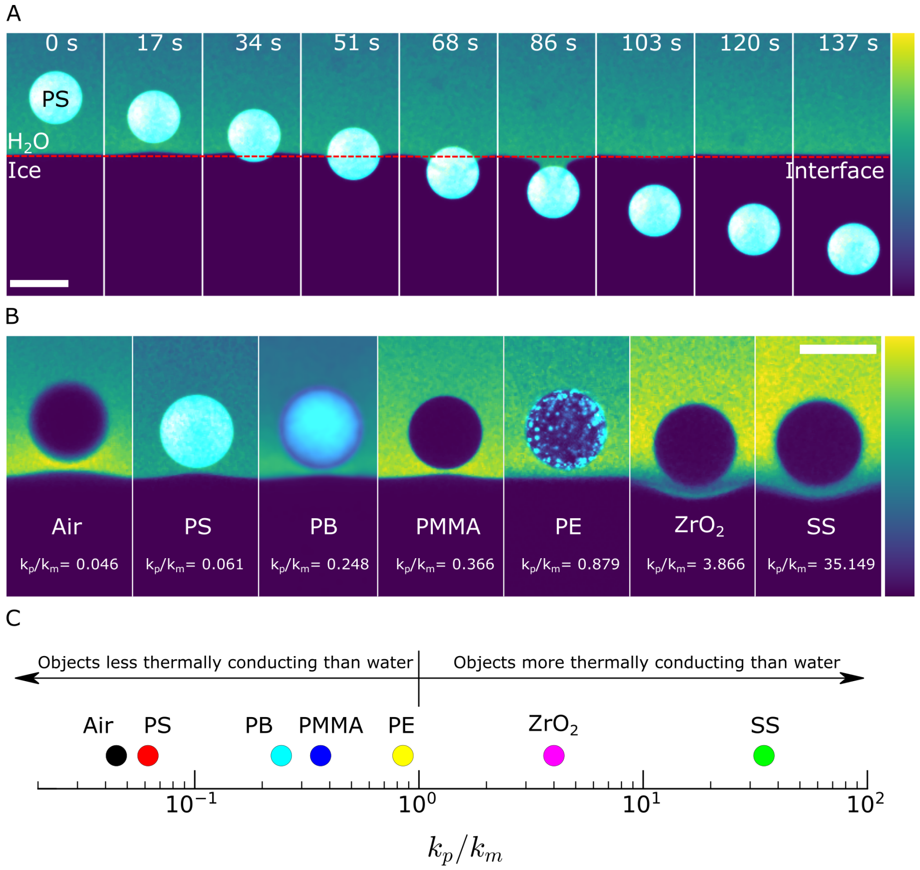

Figure 2.3: Thermal conductivity effects on interfacial curvature in absence of solute. (A) Typical time lapse for a freezing particle-in-water suspension with a polystyrene (PS) particle. The solidification front develops a bump ($t \approx 17s$) in the vicinity of the solid particle with a lower thermal conductivity than water ($k_p/k_m < 1$). PS is in cyan, water in colormap viridis (fluorescence bar) while ice is in black. (B) Air-in-water bubble, polystyrene (PS) particle, propyl benzoate (PB) droplet, and poly(methyl methacrylate) (PMMA) particle have a lower thermal conductivity than water and hence, promote a convex curvature of the solidification front. Polyethylene (PE) particle does not affect the curvature. Zirconia (ZrO_2) and stainless steel (SS) particles have a higher thermal conductivity than water and hence, result in a concave depression. We added a very small amount ($0.01 wt.\%$) of TWEEN80 to stabilise the foam and the emulsion, while no solute was present for the particle suspensions. PS, PB, and PE are in cyan, water in colormap viridis (fluorescence bar) while ice, air, PMMA, zirconia, and stainless steel are in black. Scale bar = $50 \mu m$. (C) Range (log scale) representing thermal conductivity ratio of particle to melt (k_p/k_m) used in the experiments. © (2020) S. Tyagi *et al.* (10.6084/m9.figshare.12046560) CC BY 4.0 license https://creativecommons.org/licenses/by/4.0/.

We can see from Fig. 2.4A that when $k_p/k_m > 1$, the front is always concave and has a depression away from the object. While for $k_p/k_m < 1$, three curvatures are feasible corresponding to concave, concave-convex, and convex. The domain of concave-convex geometry is limited to higher γ regions while it reduces to a confined zone when k_p/k_m is close to 1 and $\gamma < 10^{-1}$. We could not investigate this region as it requires either the use of minute objects ($R < 5\,\mu m$) or the application of a small temperature gradient ($G < 10^2\,K \cdot m^{-1}$), other parameters being constant for the particle-in-water system. While using minute objects is inconceivable as the interfacial curvature would be below the optical spatial resolution, using a smaller temperature gradient would render a planar front thermodynamically unstable owing to the supercooling [30].

The deflection of the horizontal solid-liquid front instigated by the presence of a foreign object is shown in Fig.2.4B. The values on the plot represent the maximum deflection from the bulk melting-temperature isotherm (T_m), where positive values denote a concave depression and negative values denote a convex bump. Ideally, the absolute value(s) of deflection should increase with a decreasing thermal conductivity ratio for convex curvatures and *vice-versa* for concave fronts, as predicted previously [6]. However, we report no change in deflection magnitude (for a given front shape) with the thermal conductivity ratio k_p/k_m, as demonstrated in Fig.2.4B. This might be explained by the dominant role of solid-liquid interfacial tension (included in γ) near the base of the objects, which tends to flatten the curvature, in contrast to the thermal conductivity effects [14]. Moreover, this contradiction can also originate from the use of theoretical models which ignore the effect of latent heat and assume equal thermal conductivities of the melt and the solid [21].

Interestingly, there seems to be no conspicuous digression in the dynamics of objects with $k_p/k_m < 1$ or $k_p/k_m > 1$ (Fig.2.3C), which depict similar behaviour as can be seen in the time-lapse figure (Fig. 2.3A). We do not observe repulsion of neither the soft objects (oil droplet and air bubble) nor the thermally insulating rigid particles in the system investigated, which rather tend to be engulfed instantaneously. This trend is contrary to the previous studies [6, 16], where a convex front is assumed to increase the critical engulfment velocity (V_c) and thereby facilitate repulsion of the object through a reduction of lubrication drag forces in the gap between the particle and the front [14]. The engulfment of thermally insulating ZrO_2 particles in Aluminum matrix ($k_p/k_m < 1$) has been reported previously by Sen *et al.* [21]. However, their study reports the observation of a concave trough as the object approaches the solidification front, irrespective of the particle to melt thermal conductivity ratio. We did not observe the formation of such a concave trough while a thermally insulating particle encountered the ice-water front, as shown in Fig.2.3A,B.

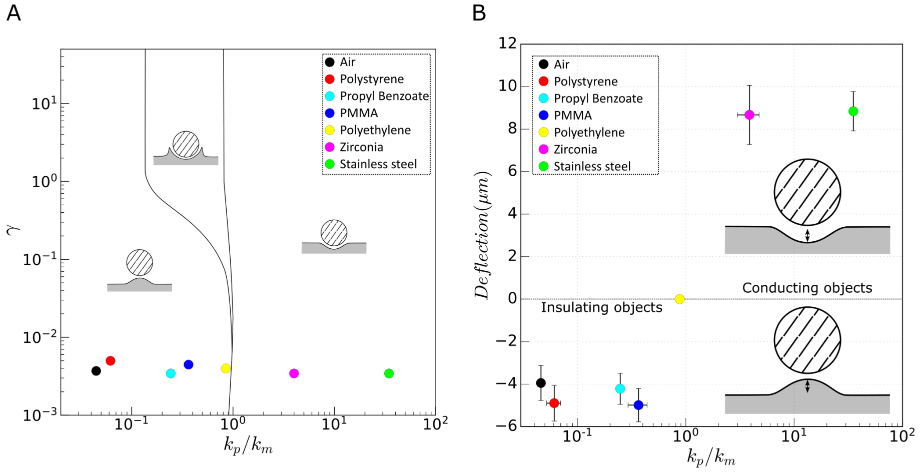

Figure 2.4: Deflection of interfacial curvature with increasing thermal conductivity ratio (k_p/k_m). (A) Three distinct curvatures of the solidification front in the thermal conductivity ratio (k_p/k_m) versus γ plane for a spherical particle, adapted from Park *et al.* [14]. (B) Plot of front deflection versus (k_p/k_m) for solidification of spherical objects in absence or at low concentration of solute. © (2020) S. Tyagi *et al.* (10.6084/m9.figshare.12046560) CC BY 4.0 license https://creativecommons.org/licenses/by/4.0/.

All these predictions and results were obtained so far in pure systems. However, almost all real melt systems consist of solutes in some form or the other, be it desired (for imparting better mechanical and/or physical properties) or undesired (such as impurities, inclusions etc...). It has been shown recently that the dynamics of interaction of an object with a solidification front and the critical role of solutes have been highly underestimated in the studies so far [31]. We cannot use the existing models as they consider a dominant role of thermomolecular forces, which are effective only at very short distances ($\sim 10^{-10}$ m) [9, 15, 24, 32], while solute fields are long range($\sim 10^{-4}$ m) [1, 31]. We therefore investigate how solute impacts the interfacial curvature.

2.3.2 Solute effects override thermal conductivity effects

We carried out freezing experiments with the same set of objects (oil droplets, gas bubbles, and particles) in the presence of $1\,wt.\%$ TWEEN80 (acting as a model solute) added to the aqueous phase. This surfactant, needed to stabilize the bubbles and drops, is used primarily as a model solute as it decreases colligatively the freezing point in all systems. We assume the magnitude of thermal conductivity ratio of the objects to melt (k_p/k_m) as shown in Fig. 2.3C remains unmodified. Thermal conductivity is a material property that depends primarily on temperature, and thus, we expect no significant changes to its value while adding small amounts of solute to water. We observed a convex interfacial curvature in the absence of solute with $k_p/k_m < 1$ (see Fig. 2.3B,C), however, in the presence of solute, solely concave curvatures are observed (Fig. 2.5A,B). In the presence of thermally conducting objects ($k_p/k_m > 1$, see Fig. 2.5B), the front exhibits a much more pronounced concave depression as compared to the geometry observed in the absence of solutes (Fig. 2.6) [22]. Thus, the solute tends to play a dominant role and renders the solidification front concave regardless of the thermal conductivity ratio, as predicted previously in theory [9, 15, 22, 23, 24].

As an insoluble object approaches a solidification front, it obstructs the diffusion field, and leads to a build-up of solutes (rejected by ice) at the front [15]. Since growth from solutions depends on the concentration gradient of solutes at the front, the liquidus temperature of the melt differs from the melting temperature of the bulk composition. The change in liquid composition alters its transformation temperature, referred to as constitutional supercooling [33]. Therefore, the solute-rich region colligatively depresses the freezing point of the aqueous phase. This distortion of the isotherm away from the horizontal manifests itself as the concave depression of the solidification front [9, 10, 15, 23, 24]. The presence of solute might lead to a variation of the ice-water interfacial tension (σ_{sl}), which is complex to evaluate experimentally. However, we believe that the influence of solute, by instigating constitutional supercooling, dominates over the interfacial energy and controls the front curvature, as stated in the past studies [9, 15, 22, 23, 24].

The resulting thick film, visible in the high fluorescence crescent (Fig. 2.7) between the object and the growing ice, is driven by the tendency to reduce the interfacial free energy and known as a premelted film [34, 35, 36]. The films are thermodynamically stable below their bulk melting temperature and are extremely sensitive to the presence of solutes (known as solute premelting). The

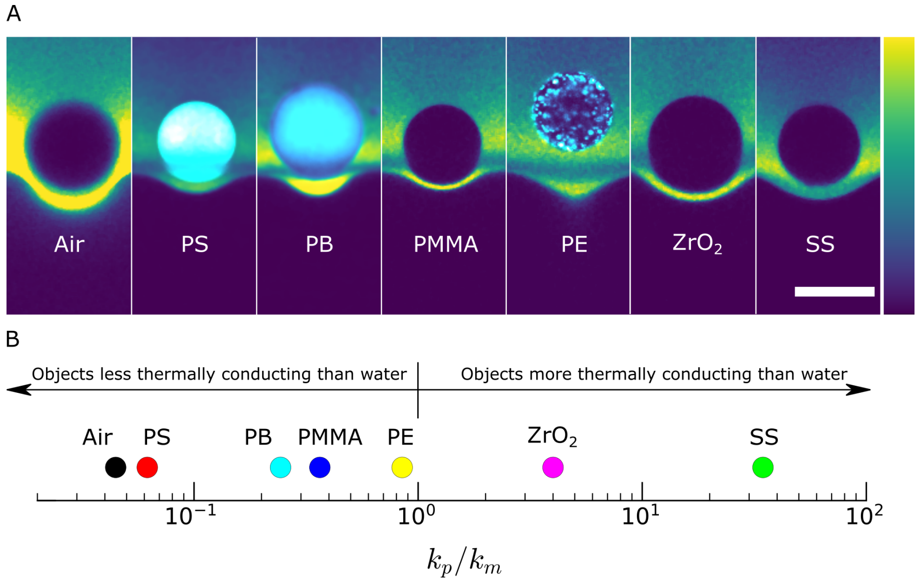

Figure 2.5: Impact of solute on the front curvature. (A) Concave depression of the solidification front with air bubble, polystyrene (PS), propyl benzoate (PB), poly(methyl methacrylate) (PMMA), polyethylene (PE), zirconia (ZrO_2), and stainless steel (SS) particles. PS, PB, and PE are in cyan, water in colormap viridis (fluorescence bar) while ice, air, PMMA, zirconia, and stainless steel are in black. Scale bar = $50\,\mu m$. (B) Range (log scale) representing thermal conductivity ratio of particle to melt (k_p/k_m) used in the experiments remains unmodified on addition of $1\,wt.\%$ solute to the aqueous phase. © (2020) S. Tyagi *et al.* (10.6084/m9.figshare.12046560) CC BY 4.0 license https://creativecommons.org/licenses/by/4.0/.

solute premelted films are quite evident in these experiments (Fig. 2.7), however, we do not observe any interfacial premelting in the absence or at low concentrations of solute (Fig. 2.3A). The concave curvature of the front facilitates lateral solute diffusion causing the front to accelerate, while engulfing the object with a solute-rich premelted film around it [22, 32].

These results depart from the behaviour predicted in the analytical models incorporating solute effects [9, 10, 15, 24]. In these studies, solute fields are expected to affect the curvature of the solidification front and hence the particle behaviour. The models certainly utilise the concave curvature of the front to calculate the modified force equilibrium but still consider a dominant role of inter-molecular forces ($d < 10\,nm$). In our experiments, a thick premelted film ($\approx 5\,\mu m$) prevents the contact of the object with the growing crystal during engulfment, suggesting an absence of repulsive short-range van der Waals forces. The

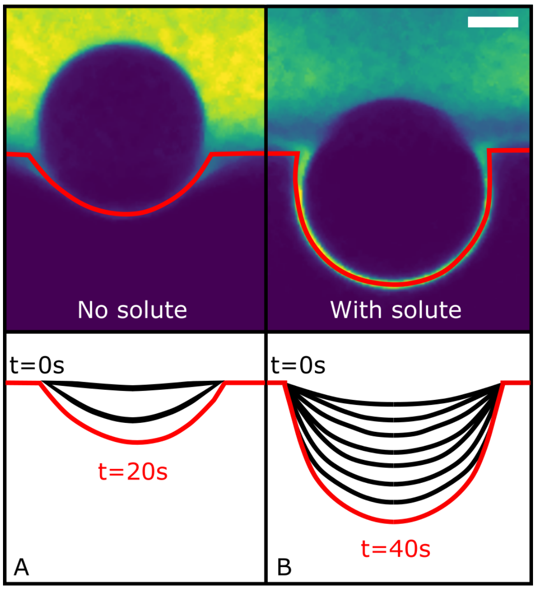

Figure 2.6: Maximum interfacial curvature depression with time observed before engulfment. In absence (A) and presence (B) of solute; $1\,wt.\%$ TWEEN80, for a zirconia particle with a higher thermal conductivity than water ($k_p/k_m > 1$). Scale bar = $20\,\mu m$. © (2020) S. Tyagi *et al.* (10.6084/m9.figshare.12046560) CC BY 4.0 license https://creativecommons.org/licenses/by/4.0/.

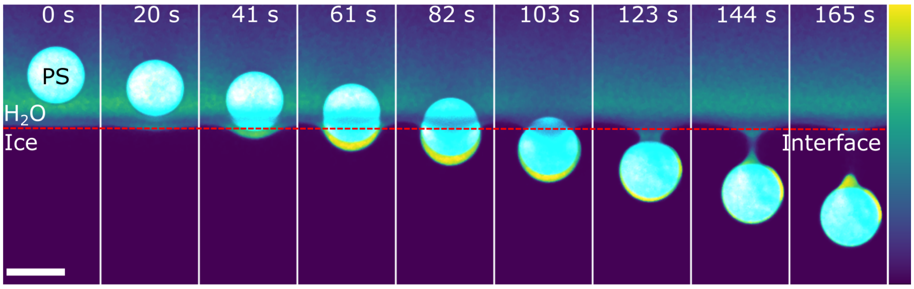

Figure 2.7: Thick premelted film at the solid-liquid front in presence of solute. Typical time-lapse for a freezing particle-in-water suspension, with a PS particle, in the presence of solute: $1\,wt.\%$ TWEEN 80. The solidification front bends away from the solid ($t \approx 41\,s$) and eventually heals leaving a premelted film around the engulfed particle. PS is in cyan, water in colormap viridis (fluorescence bar) while ice is in black. Scale bar = $50\,\mu m$. © (2020) S. Tyagi *et al.* (10.6084/m9.figshare.12046560) CC BY 4.0 license https://creativecommons.org/licenses/by/4.0/.

presence of a thick premelted film is universal and manifests itself in all systems investigated including oil-in-water droplet, air-in-water bubble, and rigid solid particles as shown in Fig. 2.5A.

We believe the long-range solute field interactions (with a length scale of $\sim D/V_{sl}$, where D is the diffusion coefficient of the solute and V_{sl} the solidification front velocity) dominate over the short-range thermomolecular forces. This enforces the importance of purely diffusive (solute) effects during solidification as they not only alter the interfacial curvature but also the nature and equilibrium of forces on the particle. Solutes impact the premelted film thickness [35], viscosity, undercooling [13], and can induce phoresis of suspended objects [31, 37] during freezing. Therefore, the prediction of the object behaviour when it encounters a solidification front is not trivial. We suggest that the thermal conductivity ratio (k_p/k_m) does not affect neither the front morphology nor the particle-front interactions in presence of solute as opposed to pure materials. The diffusion of solute tends to override and dominate the particle-front interaction in impure materials. Hence, the formulation of models, for concluding whether an object will undergo engulfment or rejection, needs to be modified to account for long-range solute field interactions. However, modelling of the solute effects is beyond the scope of this study.

2.3.3 Solute and thermal conductivity effects in cellular growth

We have discussed so far the interfacial geometry for an ideal planar front morphology preceding particle engulfment. We will now focus on the breakdown of the planar front and the subsequent impact of thermal conductivity mismatch (between object, melt and solid), when a particle is engulfed. Most realistic systems present a scenario where a planar shape is thermodynamically not stable [30]. This can be attributed to a high freezing velocity, constitutional supercooling, and the complete rejection of solutes from the solid phase, which produces a severe concentration gradient at the front [33, 38]. The resulting perturbations destabilise a *steady-state* planar front into regularly spaced cells through the propagation of Mullins-Sekerka instability [39]. Although these instabilities have been investigated for a long time, few numerical simulation models [23, 40, 41, 42] and experimental evidence [32] describing the capture of isolated particles by a non-planar (cellular or dendritic) front morphology exist. Furthermore, these studies discuss the nature and equilibrium of forces pertaining to the induced front curvature before engulfment or entrapment. However, we report on the interplay between thermal conductivity mismatch (of object and matrix) and solute effects before, during, and after engulfment with three different spherical objects.

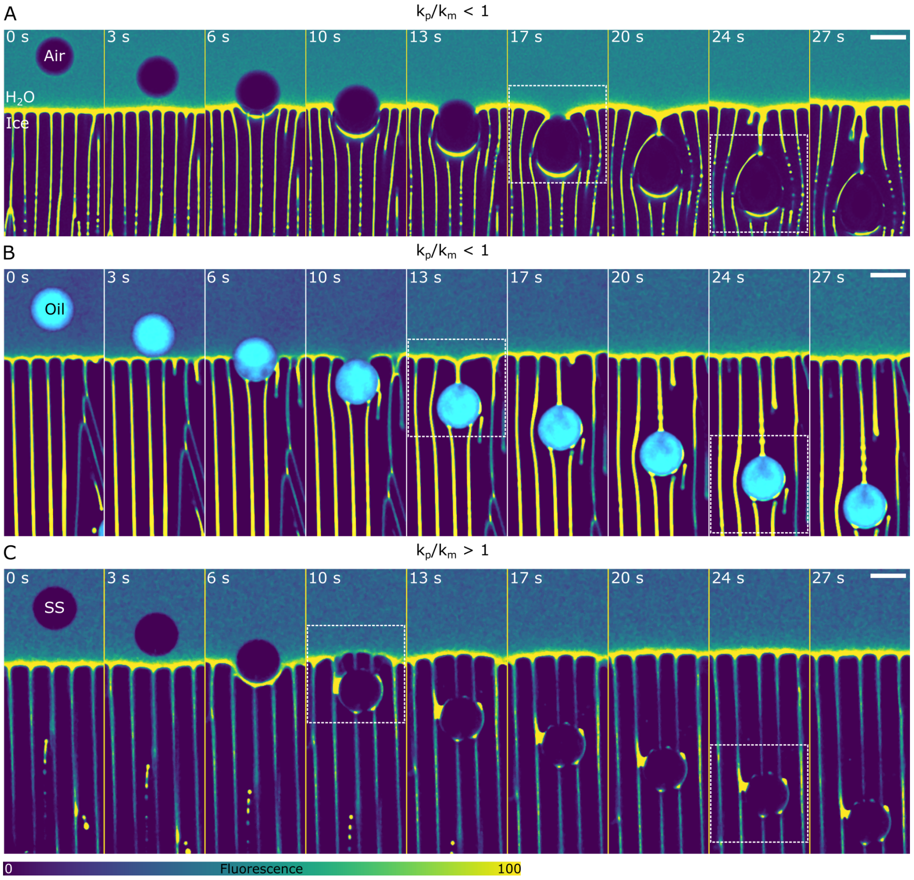

Figure 2.8: Deformation of the cell boundaries and blunting of the ice tip radius at the solidification front during object engulfment. (A, B, and C) Time-lapse of oil-in-water emulsion (A) with $G = 10\,K \cdot mm^{-1}$, air-in-water foam (B) with $G = 15\,K \cdot mm^{-1}$, and stainless steel particle (SS) (C) with $G = 10\,K \cdot mm^{-1}$, at $V_{sl} = 10 \times 10^{-6}\,m \cdot s^{-1}$. Oil is in cyan, water in colormap viridis (fluorescence bar) and ice, air, and SS are in black. Scale bar = $50\,\mu m$. © (2020) S. Tyagi *et al.* (10.6084/m9.figshare.12046560) CC BY 4.0 license https://creativecommons.org/licenses/by/4.0/.

At high solidification velocity ($V_{sl} = 10 \times 10^{-6}\,m \cdot s^{-1}$) with $1\,wt.\%$ TWEEN80 in the aqueous phase, we obtain a cellular front morphology with solute-rich cells boundaries (Fig. 2.8). For bubbles (Fig. 2.8A), the front tends to be moderately convex ($t \approx 3\,s$) with a deflection away from the horizontal, owing to the extremely low thermal conductivity of air, while it transforms into a concave depression in the proximity of the bubble ($t > 3\,s$). For the oil-in-water emulsion (Fig. 2.8B), the solidification front stays at the same ordinate before the droplet impingement

($t < 3\,s$), contrary to the depression in planar morphology (Fig. 2.5A). The stainless steel particle (Fig. 2.8C), having a higher thermal conductivity than water, induces a concave cusping of the front ($t \approx 3\,s$), which is further enhanced by the constitutional supercooling ($t \approx 6\,s$).

The solutes are partially segregated into the cell boundaries and hence, the effective concentration gradient at the ice-water front is considerably reduced compared to the previous planar front situations. Cellular fronts redistributes the rejected solutes parallel to the temperature gradient. This diminishes the extent of constitutional supercooling, thereby averting an extensive cusping of the front and preventing a dominant role of solutes before engulfment [22]. Thus, the effective distance between the object and the ice at which solutes modify the interfacial geometry of a cellular front is considerably smaller compared to a planar front morphology [32].

After engulfment, the insulating particles ($k_p/k_m < 1$)(Fig. 2.8A,B) deform the cell boundaries in their vicinity ($t > 10\,s$, inset box) and alter the ice tip radius. We believe the thinning of the cells around these particles is essentially related to the local temperature gradients originating from the difference in thermal conductivity between the particle and the encircling crystal. The engulfed objects remain at relatively higher temperatures, in contrast to the surrounding ice crystals, for sufficient amount of time to modify the solidified microstructure. Indeed, the cells boundaries do not undergo geometrical modifications (Fig. 2.8C) with a stainless steel particle, as it is highly thermally conductive ($k_p/k_m > 1$), and therefore, homogenises its temperature with the surrounding ice instantaneously [19].

The rapid cryo-confocal microscopy enables us to follow *in situ* the evolution of the microstructure. The front eventually heals and recovers its original cellular spacing, which is a function of temperature gradient, solidification velocity, and solute concentration gradient [33, 39]. The freezing of suspensions with a cellular front is an attractive route for processing porous ceramics, metals, and even composites [43]. An improved understanding of the critical parameters is thus desired to regulate the front morphology and the resulting material properties [44]. The size and spacing of cells is an indispensable attribute controlling the mechanical properties of a polycrystalline material (*Hall-Petch relationship*) [45, 46]. Consequently, the heterogeneous microstructure can be detrimental to an otherwise homogeneous finished product. For example, the object-melt thermal mismatch can lead to a variation in the inter-lamellar spacing around the particle during solidification of particle reinforced alloys [5]. Thus, solutes play a key role in solidification and an in-depth understanding of their redistribution mechanism is required.

2.4 Conclusions

Cryo-confocal microscopy [31] exhibits great promise for the *in situ* analysis of solidification mechanisms with foreign objects. We have demonstrated the role of a thermal conductivity mismatch of the object and the melt on the distortion of solidification fronts in the absence of solutes. The use of laser fluorescence enabled us to visualize the front geometry and thereby quantify the maximum solid-liquid front deflection induced by the presence of foreign objects. Furthermore, we have discussed the solidification dynamics of an extensive range of insulating and thermally conducting objects, comprising air bubbles, oil droplets, and solid particles. In the presence of solute, the long-range solute field interactions play a critical role on the front curvature and the evolution of the solidification microstructure. We have suggested that the solutes impact not only the front geometry but also the nature and magnitude of forces acting on the objects. With cellular front morphology, we have depicted that the persistent local temperature gradients around the engulfed particles (with $k_p/k_m < 1$) distort the cell boundaries and can induce a variation of the cell spacing. Our study opens new pathways for the quantification of theoretical parameters which were difficult to measure previously. Finally, we hope our extensive research with ceramic, metal, and polymer objects serves for the formulation of a robust physical model with the incorporation of long-range solute effects.

Acknowledgements

The research leading to these results has received funding from the ANRT and Saint-Gobain through a CIFRE fellowship ($N°$ 2017/0774). H.H.'s internship was funded by Saint-Gobain.

Author contributions

S.D. and C.M. designed and supervised the project, S.D, C.M. and S.T. designed the experiments, S.T. and H.H. carried out the confocal microscopy, S.T. wrote the code to analyze the data, S.T., C.M. and S.D. analyzed the data. All authors discussed the results and implications. S.T., C.M. and S.D. wrote the manuscript.

Conflict of interest

The authors declare no conflict of interest.

Citation

This chapter can be cited as Tyagi, S., Huynh, H., Monteux, C. & Deville, S. Objects interacting with solidification fronts: Thermal and solute effects. Materialia 12, 2020 https://doi.org/10.1016/j.mtla.2020.100802.

Bibliography

[1] R. Asthana and S. N. Tewari. The engulfment of foreign particles by a freezing interface. *Journal of Materials Science*, 28(20):5414–5425, 1993.

[2] Arturo E Corte. Vertical migration of particles in front of a moving freezing plane. *Journal of Geophysical Research*, 67(3):1085–1090, 1962.

[3] D. R. Uhlmann, B. Chalmers, and K. A. Jackson. Interaction between particles and a solid-liquid interface. *Journal of Applied Physics*, 35(10):2986–2993, 1964.

[4] Ch Körber, G. Rau, M. D. Cosman, and E. G. Cravalho. Interaction of particles and a moving ice-liquid interface. *Journal of Crystal Growth*, 72(3):649–662, 1985.

[5] Doru M. Stefanescu, B. K. Dhindaw, S. A. Kacar, and A. Moitra. Behavior of ceramic particles at the solid- liquid metal interface in metal matrix composites. *Metallurgical Transactions A*, 19(11):2847–2855, 1988.

[6] D. Shangguan, S. Ahuja, and D. M. Stefanescu. An analytical model for the interaction between an insoluble particle and an advancing solid/liquid interface. *Metallurgical Transactions A*, 23(2):669–680, 1992.

[7] AA Chernov, DE Temkin, and AM Mel'Nikova. Theory of the capture of solid inclusions during the growth of crystals from the melt. *Sov. Phys. Crystallogr*, 21(4):369–373, 1976.

[8] AA Chernov, DE Temkin, and AM Mel'Nikova. The influence of the thermal conductivity of a macroparticle on its capture by a crystal growing from a melt. *Sov. Phys. Crystallogr*, 22(6):656–658, 1977.

[9] Jürgen Pötschke and Volker Rogge. On the behaviour of foreign particles at an advancing solid-liquid interface. *Journal of Crystal Growth*, 94(3):726–738, 1989.

[10] R. Sasikumar and T. R. Ramamohan. Distortion of the temperature and solute concentration fields due to the presence of particles at the solidification front-effects on particle pushing. *Acta Metallurgica et Materialia*, 39(4):517–522, 1991.

[11] Layachi Hadji. The drag force on a particle approaching a solidifying interface. *Metallurgical and Materials Transactions A*, 37(12):3677–3683, 2006.

[12] A. W. Rempel and M. G. Worster. Interaction between a particle and an advancing solidification front. *Journal of Crystal Growth*, 205(3):427–440, 1999.

[13] A. W. Rempel and M. G. Worster. Particle trapping at an advancing solidification front with interfacial-curvature effects. *Journal of Crystal Growth*, 223(3):420–432, 2001.

[14] Min S. Park, Alexander A. Golovin, and Stephen H. Davis. The encapsulation of particles and bubbles by an advancing solidification front. *Journal of Fluid Mechanics*, 560:415, 2006.

[15] J. K. Kim and P. K. Rohatgi. The effect of the diffusion of solute between the particle and the interface on the particle pushing phenomena. *Acta Materialia*, 46(4):1115–1123, 1998.

[16] AM Zubko, VG Lobanov, and V V_ Nikonova. Reaction of foreign particles with a crystallization front. *Sov. Phys. Crystallogr.*, 18(2):239–241, 1973.

[17] MK Surappa and PK Rohatgi. Heat diffusivity criterion for the entrapment of particles by a moving solid-liquid interface. *Journal of Materials Science*, 16(2):562–564, 1981.

[18] S. N. Omenyi and A. W. Neumann. Thermodynamic aspects of particle engulfment by solidifying melts. *Journal of Applied Physics*, 47(9):3956–3962, 1976.

[19] M. Yemmou, M. A. Azouni, P. Casses, and G. Pétré. Thermal aspects of particle engulfment by a solidifying front. *Journal of Crystal Growth*, 128(1-4 part 2):1130–1136, 1993.

[20] Doru M. Stefanescu, Rajesh V. Phalnikar, Hantong Pang, Sanjay Ahuja, and Brij K. Dhindaw. A Coupled Force Field-Thermal Field Analytical Model for the Evaluation of the Critical Velocity for Particle Engulfment. *ISIJ International*, 35(6):700–707, 1995.

[21] S. Sen, W. F. Kaukler, P. Curreri, and D. M. Stefanescu. Dynamics of solid/liquid interface shape evolution near an insoluble particle - An X-ray transmission microscopy investigation. *Metallurgical and Materials*

Transactions A: Physical Metallurgy and Materials Science, 28(10):2129–2135, 1997.

[22] Adrian V. Catalina, Subhayu Sen, Doru M. Stefanescu, and William F. Kaukler. Interaction of porosity with a planar solid/liquid interface. *Metallurgical and Materials Transactions A*, 35(5):1525–1538, 2004.

[23] Yi Yang, J. W. Garvin, and H. S. Udaykumar. Sharp interface numerical simulation of directional solidification of binary alloy in the presence of a ceramic particle. *International Journal of Heat and Mass Transfer*, 51(1-2):155–168, 2008.

[24] Justin C. T. Kao and Alexander A. Golovin. Particle capture in binary solidification. *Journal of Fluid Mechanics*, 625(September 2008):299, 2009.

[25] T Gaillard, M Roché, C Honorez, M Jumeau, A Balan, C Jedrzejczyk, and W Drenckhan. Controlled foam generation using cyclic diphasic flows through a constriction. *International Journal of Multiphase Flow*, 96:173–187, 2017.

[26] Zenaida Briceño-Ahumada and Dominique Langevin. On the influence of surfactant on the coarsening of aqueous foams. *Advances in Colloid and Interface Science*, 244:124–131, 2017.

[27] Dmytro Dedovets, Cécile Monteux, and Sylvain Deville. A temperature-controlled stage for laser scanning confocal microscopy and case studies in materials science. *Ultramicroscopy*, 195(August):1–11, 2018.

[28] Moreno Marcellini, Cecile Noirjean, Dmytro Dedovets, Juliette Maria, and Sylvain Deville. Time-Lapse, in Situ Imaging of Ice Crystal Growth Using Confocal Microscopy. *ACS Omega*, 1(5):1019–1026, 2016.

[29] Johannes Schindelin, Ignacio Arganda-Carreras, Erwin Frise, Verena Kaynig, Mark Longair, Tobias Pietzsch, Stephan Preibisch, Curtis Rueden, Stephan Saalfeld, Benjamin Schmid, et al. Fiji: an open-source platform for biological-image analysis. *Nature Methods*, 9(7):676, 2012.

[30] C Körber. Phenomena at the advancing ice-liquid interface: solutes, particles and biological cells. *Quarterly Reviews of Biophysics*, 21:229–298, 1988.

[31] Dmytro Dedovets, Cécile Monteux, and Sylvain Deville. Five-dimensional imaging of freezing emulsions with solute effects. *Science*, 360(6386):303–306, 2018.

[32] J. A. Sekhar and R. Trivedi. Solidification microstructure evolution in the presence of inert particles. *Materials Science and Engineering A*, 147(1):9–21, 1991.

[33] WA Tiller, KA Jackson, JW Rutter, and B Chalmers. The redistribution of solute atoms during the solidification of metals. *Acta Metallurgica*, 1(4):428–437, 1953.

[34] J. W. Cahn, J. G. Dash, and Haiying Fu. Theory of ice premelting in monosized powders. *Journal of Crystal Growth*, 123(1-2):101–108, 1992.

[35] J. Wettlaufer. Impurity Effects in the Premelting of Ice. *Physical Review Letters*, 82(12):2516–2519, 1999.

[36] A. W. Rempel, J. S. Wettlaufer, and M. G. Worster. Interfacial Premelting and the Thermomolecular Force: Thermodynamic Buoyancy. *Physical Review Letters*, 87(8):088501, 2001.

[37] John L Anderson. Colloid transport by interfacial forces. *Annual Review of Fluid Mechanics*, 21(1):61–99, 1989.

[38] M. G. O'Callaghan, E. G. Cravalho, and C. E. Huggins. Instability of the planar freeze front during solidification of an aqueous binary solution. *Journal of Heat Transfer*, 102(4):673–677, 1980.

[39] W. W. Mullins and R. F. Sekerka. Stability of a planar interface during solidification of a dilute binary alloy. *Journal of Applied Physics*, 35(2):444–451, 1964.

[40] B. Dutta and M. K. Surappa. Directional dendritic solidification of a composite slurry: Part I. Dendrite morphology. *Metallurgical and Materials Transactions A: Physical Metallurgy and Materials Science*, 29(4):1319–1327, 1998.

[41] B. Dutta and M. K. Surappa. Directional dendritic solidification of a composite slurry: Part II. Particle distribution. *Metallurgical and Materials Transactions A: Physical Metallurgy and Materials Science*, 29(4):1329–1339, 1998.

[42] Anthony Chang, Jonathan A. Dantzig, Brian T. Darr, and Allison Hubel. Modeling the interaction of biological cells with a solidifying interface. *Journal of Computational Physics*, 226(2):1808–1829, 2007.

[43] Sylvain Deville. Ice-Templated Materials: Polymers, Ceramics, Metals and Their Composites. In *Freez. Colloids Obs. Princ. Control. Use*, chapter 4, pages 253–350. Springer International Publishing, Cham, 2017.

[44] Sylvain Deville, Eric Maire, Guillaume Bernard-Granger, Audrey Lasalle, Agnès Bogner, Catherine Gauthier, Jérôme Leloup, and Christian Guizard. Metastable and unstable cellular solidification of colloidal suspensions. *Nature Materials*, 8(12):966, 2009.

[45] EO Hall. The deformation and ageing of mild steel: iii discussion of results. *Proceedings of the Physical Society. Section B*, 64(9):747, 1951.

[46] NJ Petch. The cleavage strength of polycrystals. *Journal of the Iron and Steel Institute*, 174:25–28, 1953.

Chapter 3

Solute effects on dynamics and deformation of freezing droplets

Abstract

Soft or rigid objects, suspended in a liquid melt, interact with an advancing solidification front in various industrial and natural processes, such as fabrication of particle-reinforced-composites, growth of crystals, cryopreservation, frost heave, and growth of sea ice. The object-front interaction can have diverse outcomes depending on the solidification parameters and the physical characteristics of the object-melt-solid system. The approaching front can engulf the object immediately, push the object indefinitely in the remaining liquid ahead of itself, or repel the object for some time before capturing it in the growing solid. Hence, the object dynamics relative to the front determine the microstructure as well as the functional properties of the solidified material. The previous studies have extensively investigated the interaction of foreign objects with a moving solid-liquid interface in pure melts. However, in most real-life systems, the probability of encountering a pure melt is rare and solutes (or impurities) are almost always present. Here we show experimentally the interaction of spherical oil droplets with a moving planar ice-water interface, while systematically increasing the solute concentration in the bulk liquid, using *in situ* cryo-confocal microscopy. We demonstrate that a small amount of solute in the bulk liquid can instigate long-range droplet repulsion, extending over a length scale of 40 to 100 μm, in contrast to the short-range predicted previously (< 1 μm). We report on the droplet deformation, while they are in contact with the ice-water interface, as a function of the bulk solute concentration, the droplet size, and the crystal growth rate. Furthermore, we depict the dynamic evolution of solute-enriched premelted films ($\approx 5\ \mu m$) and the role of solute in instigating the crushing of droplets captured in the growing ice crystal. Our results demonstrate how an increasing concentration of solute in the bulk and its subsequent segregation during solidification can dramatically alter the predicted nature of object-front interactions and the solidification microstructures. We anticipate that our experimental study can serve for the development of theoretical models incorporating solute effects. Finally, we suggest that the freezing of oil-in-water emulsions may serve as an analogue for studying the *in situ* interaction of foreign objects with an advancing solid-liquid interface in the presence of solute effects.

Keywords: solidification, solute, droplets, deformation, dynamics

3.1 Introduction

The interaction of objects with an approaching solid-liquid interface is of special relevance in nature, like frost heave, glacial motion [1], and in engineering sciences, such as food freeze-thaw stability [2], cryopreservation [3, 4], metallurgy [5], and crystal growth [6]. This dynamic problem consists of objects, soft or hard, dispersed in a liquid melt interacting with a solid-liquid interface. The objects can be biological cells in cryopreservation [3, 4], colloids in freeze-casting [7], droplets in food preservation [8], gas bubbles in growth of single crystals [6, 9] and metallurgy [5], or reinforcing particles in material-matrix-composites [10]. The outcome of the object-interface confrontation determines the solidified microstructure and hence, the functional properties of the solidified material. Thus, it is essential to understand the underlying mechanisms of solidification (or freezing) to forge the required material microstructure. The object can interact with an advancing solidification interface with diverse outcomes; the object can be engulfed instantaneously upon contact, the object can be pushed ahead in the remaining liquid by the interface indefinitely, or the object may undergo engulfment after being pushed over a certain distance [11].

The dynamics of interaction and spatial distribution of objects are essential features in several material fabrication routes. In particle-reinforced-composites, an instantaneous engulfment in solid phase is desired as it facilitates a homogeneous distribution of the suspended objects [10]. In metallurgy and crystal growth, a continuous repulsion of the impurities by the interface is required to obtain impurity-free-solids [5]. In freeze-casting, a segregation of the colloidal particles by the growing solid enables a porous material structure [7]. The shape of the object (deformed or undeformed) becomes an equally important processing criterion in applications where soft deformable objects (droplets or bubbles) encounter a moving solid-liquid interface. In cryobiology, utmost care should be taken to avoid physical injury inflicted to the cells from the growing ice crystals [12]. In food preservation, freezing is conducted to conserve the size, shape, and distribution of the dispersed droplets, thereby preserving the original taste and appearance [8]. Thus, numerous interaction scenarios, still poorly understood, can exist during solidification.

The role and concentration of solute in the solidifying liquid is often significant and a dominating factor in determining, amongst others, the shape of the solid-liquid interface in the vicinity of the suspended objects [13, 14, 15]. Solutes, render the interfacial curvature concave, thereby promoting engulfment of objects at growth rates lower than those predicted for planar curvatures [16, 17]. The solutes can be either desired, like additives (e.g. cryoprotectant used in preservation of biological cells), or be present as an undesired impurity, such as dissolved gases (H_2) in liquid metals. The segregation of solutes at the interface is instigated by their relatively low solubility in the solid phase and enhanced further by the approaching objects obstructing their diffusion field [13]. This local solute enrichment is of particular importance in understanding the nucleation and growth of macroporosity in solidifying melts [14], studying the constitutional supercooling with formation of premelted films [18, 19], and in determining the osmotic stresses acting on a freezing biological cell [4, 12] to give a few examples. Moreover, the morphology of a solid-liquid interface (planar, columnar, or dendritic), determined by the magnitude of solute concentration gradient build-up ahead of the growing solid, plays a major role on the final microstructure [13, 20].

The study of solidification mechanisms such as the object dynamics, object shape evolution, and the local solute concentration are complex and require *in situ* investigations. The major problem associated with studying solidification *in situ* arises from the need of high space and temporal resolution in conjunction with elevated temperatures especially for metals. For the object dynamics, past studies have formulated a plethora of analytical and numerical models expressing the outcome (engulfment or rejection) of objects interacting at close distances ($< 10\ nm$) with the solid-liquid interface [16, 21, 22, 23, 24]. The models vary in the mathematical formulation of the features taken into account (e.g. the inclusion of object-melt thermal conductivity mismatch, solute effects etc. . .), while using a similar approach (balance of repulsive and attractive forces between the object and front) to describe the interaction [11]. The study of object deformation has been of particular interest in the prediction of pore shape evolution during directional solidification of crystals to avoid or control porosity defects. Much of the progress in this domain has been achieved through numerical simulations and post-solidification analysis [25, 26]. *In situ* experimental evidence of solidification dynamics (repulsion or engulfment) and shape modification have been facilitated using transparent analogs (e.g. succinonitrile-acetone) with optical microscopes at ambient temperatures [20, 27] and X-ray transmission microscope at elevated temperatures [14, 28]. However, the volume investigated along with the temporal resolution is limited, while the local solute segregation cannot be visualized. Hence, the tracking of microstructures where objects interact with a solid-liquid interface in the presence of solute effects remains challenging.

In light of these uncertainties, we analyse the interaction of spherical oil droplets with an advancing ice-water interface using *in situ* cryo-confocal microscopy. The objective of our study is to perform directional solidification experiments to comprehend the mechanisms responsible for the development of a solidification microstructure in the presence of foreign objects. Our custom solidification setup enables a small temporal resolution (1.7 *s*) and high spatial resolution (1024 × 1024 pixels)with laser induced fluorescence to distinguish the rejected solutes and hence, visualize the local solute segregation. To regulate the bulk solute concentration, we prepare oil-in-water emulsions using microfluidics with a varying amount of surfactant Tween 80 (acting as a model solute) in the aqueous phase. We further characterise and report on the *in situ* droplet dynamics, droplet deformation, and the role of solute in modifying the expected droplet behaviour.

We investigate the impact and consequences of an increasing bulk solute concentration on the mechanisms involved at three different stages: droplets in water (water) far from the solidification front, droplets in contact with an approaching solid-liquid interface, and droplets captured in the growing solid (here ice). For the object-front interaction dynamics, we depict the distinct behaviours of the oil droplets such as instantaneous engulfment and repulsion-engulfment transition. For the object shape evolution while confronting a solid-liquid interface, we correlate the deformation of the oil droplets to the imposed growth rate and the bulk solute concentration. Furthermore, we show the impact of solute on the ice-water meniscus and the evolution of premelted films surrounding the oil droplets in ice. Finally, we depict that the three interaction stages are crucial in determining the object spatial distribution, object shape evolution, and hence, the solidification microstructure. Thus, we suggest that the freezing of oil-in-water emulsions with solute effects can be a versatile approach towards developing an analogue for objects interacting with an advancing solidification front.

3.2 Methods

3.2.1 Materials

We purchased the oil (propyl benzoate), surfactant (Tween 80), oil fluorophore (Difluoro2-[1-(3,5-dimethyl-2H-pyrrol-2-ylidene-N)ethyl]-3,5-dimethyl-1H-pyrro lato-Nboron), and aqueous fluorophore (Sulforhodamine B) from Sigma-Aldrich. The fluorophores are referred to as BODIPY (incorporated in oil) and SRhB (incorporated in water) in the study. We cycled the deionized water through 0.45 μm Nylon membrane filters (VWR International) to remove traces of impurities and ensure purity of the emulsions prepared. The solidification experiments were conducted to study the interaction of dispersed phase with the ice-water interface. Hence, we prepared oil-in-water emulsions to ensure the dispersed phase remained liquid, while the continuous phase underwent solidification. Thus, we chose propyl benzoate owing to its low melting temperature ($T_m = -51.6° \ C$), low solubility in water (0.035 $g/100 \ g$), and similar density to water ($\rho_{oil} = 1.023 \ g \cdot cm^{-3}$).

3.2.2 Sample Preparation

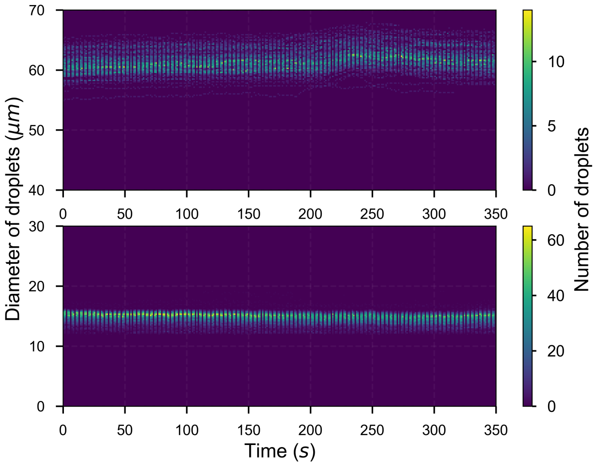

Figure 3.1: Diameter of monodisperse droplets with radii (R_1, R_2) of $7.2 \pm 0.4 \ \mu m$ and $30.9 \pm 1.2 \ \mu m$ respectively, generated using microfluidics. The size of droplets remained stable during the experimental time-scale, which varied from 15 min to 4 h.

We prepared the oil-in-water emulsions using a microfluidic setup, as explained in our previous study [15]. The monodisperse droplets have radii (R_1, R_2) of either $7.2 \pm 0.4 \ \mu m$ or $30.9 \pm 1.2 \ \mu m$, as shown in Fig.3.1. The oil phase consisted of propyl benzoate with $10^{-4} \ M$ BODIPY to obtain clear imaging of dispersed droplets at 1% laser power. For the aqueous phase, we used $10^{-5} \ M$ SRhB solution, as self-quenching was reported at concentrations above $2 \times 10^{-4} \ M$ [29]. We added Tween 80 ($HLB = 15$ [30]), a non-ionic surfactant, to the aqueous phase to stabilise the oil droplets. The surfactant Tween 80 ($cmc = 13-15\ mg \cdot l^{-1}$ [31]) also acts as a model solute since it colligatively depresses the freezing point of solutions, when its concentration increases locally [15]. We prepared three aqueous solutions with 0.01, 0.1, and 1 $wt.\%$ Tween 80 to study the impact of solute on the solidification dynamics and behaviour of oil droplets dispersed in an aqueous phase. The surfactant is added as $wt.\%$ of the aqueous solution to have an equal concentration in all the solutions prepared.

The concentration of surfactants in the bulk solution at which micelles start forming is known as the *cmc*. All additional surfactant added above the *cmc* should form micelles. Individual surfactant molecules that are in the system but are not part of a micelle are called monomers [32]. At 1 $wt.\%$ of Tween 80 in aqueous solution we are $\approx 600\times$ *cmc*. Hence, ideally we should have an excess of surfactant at the three concentrations used in the experiments. We assume (as is generally accepted) that the concentration of surfactant added below the *cmc* remains as dissociated monomers, while the concentration above the *cmc* results in micelles. The oil-in-water emulsion with the surfactant added in excess to the aqueous phase is represented schematically in Fig.3.2. The presence of micelles at the given concentration was confirmed by dynamic light scattering (DLS) analysis. A typical micelle size of 9 nm with a corresponding diffusion coefficient of 30 $\mu m^2 \cdot s^{-1}$ at 273 K was obtained from the DLS analysis. The prepared emulsions were filled through capillarity and solidified in a rectangular Hele-Shaw cell (height =100 μm and volume =100 μl). We fabricated the Hele-Shaw cell using two glass slides (Menzel, $24 \times 60\ mm$, thickness $0.13-0.16\ mm$), and sealed it with nail-polish at one end to prevent evaporation and leakage.

3.2.3 Imaging & Analysis

We used a Leica TCS SP8 confocal laser scanning microscope (Leica Microsystemes SAS, Germany) equipped with 488 nm (blue), 552 nm (green) lasers and two photodetectors (PMT) for image acquisition. The images were captured for the emission spectra of BODIPY (oil phase) and SRhB (aqueous phase), using a non-immersive objective (Leica HCX PL APO CS 20×) with a working distance of 590 μm. Ice does not fluoresce and hence, we can simultaneously detect three phases (oil droplets, unfrozen aqueous phase, and ice) with two photodetectors. In *2D*, we used the microscope at a scanning speed of 600 Hz, with 1024×1024 $pixels$ for imaging $775 \times 775\ \mu m$, resulting in 1.7 s per frame. We used Fiji [33] for image thresholding in conjunction with Python [34] for image

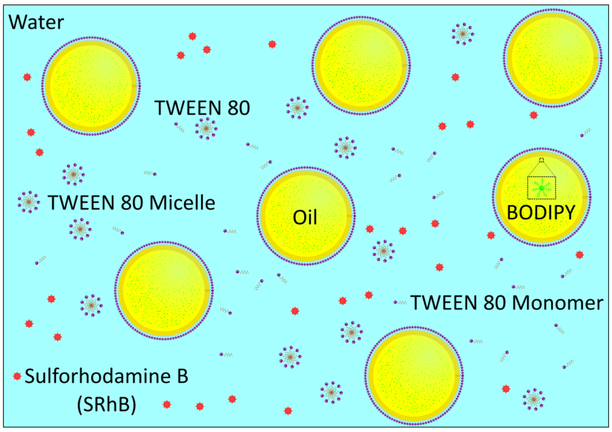

Figure 3.2: Schematic depicting a monodisperse oil-in-water emulsion with the surfactant Tween 80 and fluorophore SRhB added to the aqueous phase (not to scale). Oil phase is incorporated with the fluorophore BODIPY. The concentration of surfactant below *cmc* remains as monomers, while the concentration above the *cmc* forms micelles.

and data analysis.

3.2.4 Freezing Stage

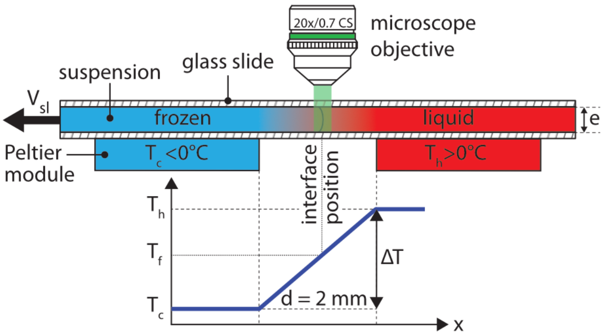

Figure 3.3: Cryo-confocal microscope setup to perform *in situ* solidification experiments. A Hele-Shaw cell containing an oil-in-water emulsion is pulled at a constant velocity (V_{sl}) through a constant linear temperature gradient (G), established by two Peltier elements. In *steady-state*, the solidification interface is at a constant position under the microscope objective. In the sample frame, the interface is moving at a solidification velocity of V_{sl}, imposed by the motor.

We conducted unidirectional solidification experiments, translating the sample cell at a constant velocity (V_{sl}) along a constant linear temperature gradient (G) of $10^4\ K \cdot m^{-1}$, using the cryo-confocal stage described in detail previously [35]. We imposed the temperature with two Peltier modules, and controlled it with high precision ($< 0.01\ °C$) using TEC-1122 Dual Thermo Electric Cooling Temperature Controller from Meerstetter Engineering, Switzerland. The Peltier elements were separated by a distance of $2\ mm$ to establish a linear temperature gradient along $\vec{x}$. The *in situ* observation of objects interacting with the solid-liquid interface was achieved using a confocal microscope mounted vertically over the gap ($2\ mm$) between the two Peltier modules, as shown in Fig.3.3. The solidification interface tends to appear immobile in the frame of observation, however, in the sample frame, a solidifying front at the velocity V_{sl} is advancing in the sample (along $\vec{x}$). We utilised the VT-80 translation stage (Micos Pollux Drive PI, USA) to impose the rate at the which the sample cell is pulled through the temperature gradient. The rate of translation was verified to be in agreement with the measured solidification velocity (V_{sl}), using posterior image analysis ($error < 1\ \%$). Thus, we can decouple and control independently the solidification velocity (V_{sl}) and the thermal gradient (G) in our system.

We performed the solidification experiments in the velocity range of $1.0 \leq V_{sl} \leq 10.0\ \mu m \cdot s^{-1}$. We wait for $20-30\ mins$ to ensure a *steady-state* diffusion controlled regime before starting the acquisition at a given solidification velocity. The time needed for a steady-state to establish scales as $2D/V_{sl}^2 \approx 60\ s$, where D is the solute diffusion coefficient. We do not expect forced convection in our experiments as they are performed in a closed Hele-Shaw cell of small thickness ($100\ \mu m$) and at low solidification velocity with a steady linear temperature gradient. The solid-liquid interface is stable over extended time periods ($\approx 4-5\ hours$) and the interface does not accelerate or decelerate during the solidification experiments. In addition, we do not observe a transient unsteady regime and the interface morphology is stable for the given experimental parameters.

3.3 Results & Discussions

We performed horizontal solidification experiments by displacing a Hele-Shaw cell, containing an oil-in-water emulsion, in a custom cryo-confocal stage, as shown in Fig.3.3. A typical *2D* confocal image of a freezing emulsion with the distinct features observed is shown in Fig.3.4A. The confocal image enables us to distinguish three phases; oil phase in cyan (fluorophore BODIPY), water in colormap viridis (fluorophore SRhB), and a dark ice phase. The solid-liquid phases are delimited by an interface advancing, at a growth rate V_{sl}, under the influence of a linear temperature gradient $G = \nabla T$ of 10^4 $K \cdot m^{-1}$ (see Fig.3.4A). As solidification progresses, the growing ice phase rejects the dissolved solutes owing to its low solubility ($K_0 << 1$, where K_0 is the partition coefficient) and hence, appears black. A representation of the rejected solute field in *steady-state* planar growth is shown in Fig.3.4A. We also depict the presence of premelted films, which can remain liquid at temperature below the equilibrium melting temperature ($T < T_m$) and increase in thickness owing to the presence of dissolved solutes [1]. In Fig.3.4A, we can observe the premelted films between two ice surfaces with different grain orientation as well as around the oil droplets captured in the ice phase.

A typical time-lapse evolution of an isolated oil droplet interacting with the ice-water interface is shown in Fig.3.4B. The images in Fig.3.4A and Fig.3.4B are representative of the freezing of an oil-in-water emulsion with $1\,wt.\%$ Tween 80 (solute) in the aqueous phase. In this study, we discuss the consequences of the interaction of oil droplets with the solid-liquid interface at three different stages, as described in Fig.3.4B, while systematically varying the concentration of solute. First, we investigate the solidification mechanisms at play when the oil droplets are far from the advancing interface. The aim is to study the role of an increasing bulk solute concentration and the different solidification parameters (growth rate, object size) on the droplet dynamics in water ($t < 44$ s in Fig.3.4B). Subsequently, we look into the impact of the approaching solid-liquid interface on the droplet shape upon their mutual contact ($44 \le t \le 57$ s in Fig.3.4B). The objective here is to comprehend the object shape evolution in the presence (or not) of solute effects and the corresponding impact of increasing the object size and growth rate. Finally, we analyse the droplets captured in ice and report on the evolution of premelted films with the associated ice-water meniscus ($99 \le t \le 111$ s in Fig.3.4B).

3.3.1 Droplets in water

The ice-water interface is stationary in the frame of observation, while in the sample frame it is in motion at a velocity of V_{sl} along $\vec{x}$ (see Fig.3.4A). We calculate the isolated droplet velocity U_r, when the ice-water interface is close and

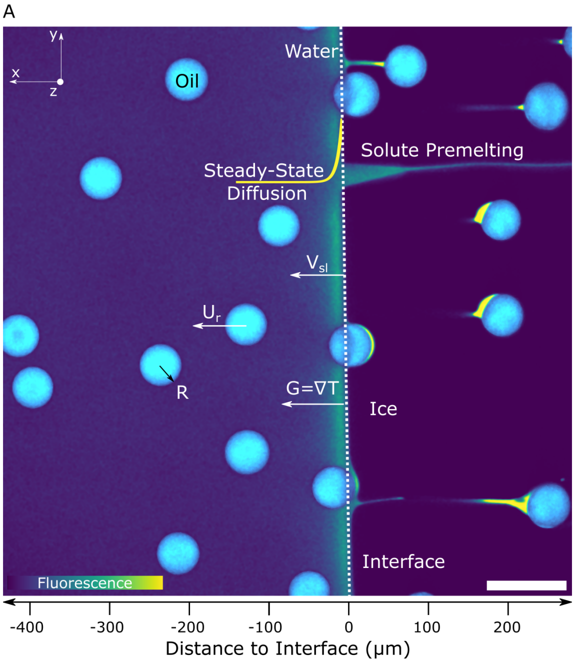

Figure 3.4: *2D* cryo-confocal image of freezing an oil-in-water emulsion in the presence of $1 wt.\%$ Tween 80 in the aqueous phase. (A) Typical features observed for a planar growth at $V_{sl} = 2\ \mu m \cdot s^{-1}$ (B) Time-lapse evolution of an oil droplet encountering an approaching solid-liquid interface with three distinct regimes of interaction at $V_{sl} = 2\ \mu m \cdot s^{-1}$. Ice is in black, oil droplets in cyan, and the aqueous phase is in colormap viridis (fluorescence bar). Scale bar = $100\ \mu m$**.**

investigate how the droplet speed, relative to the front, depends on the solidification parameters. Our Hele-Shaw cell of length $4\ cm$ facilitates an acquisition of $50--400$ isolated droplet velocities in the vicinity of an advancing solidification front and hence, we can deduce the mean droplet velocity as $\overline{U} = \langle U_r \rangle$. A positive magnitude of $\overline{U}$ implies that the droplet is repelled or pushed by the moving ice-water interface towards the remaining liquid. A detailed description of the analysis performed along with the python script employed can be found in a previous study [19] and in the supplementary data (Fig.3.14, Fig.3.15).

In Fig.3.5, we present the mean droplet velocity, $\overline{U}$, with the distance to interface for the trajectories investigated at a growth rate V_{sl} of $3\ \mu m \cdot s^{-1}$. We define the distance to interface as $0\ \mu m$ when the front edge of the droplet comes in contact with the absolute detected position of the ice-water interface.

The droplets in water are unperturbed at distances of $\leq -100\ \mu m$ and start

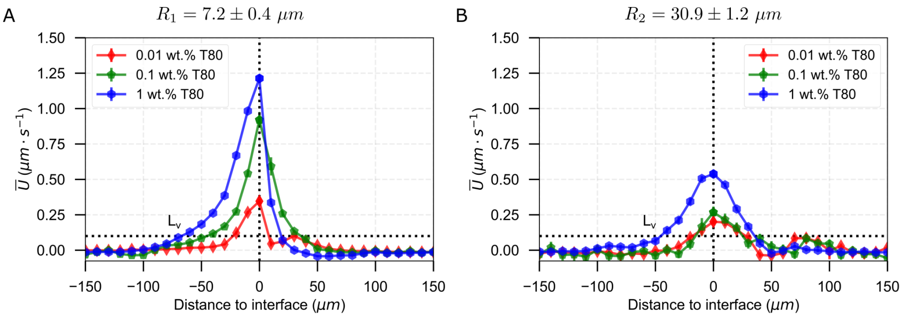

Figure 3.5: Droplet dynamics in presence of 0.01, 0.1, and $1\,wt.\%$ solute in solution, deduced from the droplet trajectories at $V_{sl} = 3\ \mu m \cdot s^{-1}$. Mean droplet velocity versus distance to interface for (A) $R_1 = 7.2 \pm 0.4\ \mu m$ and (B) $R_2 = 30.9 \pm 1.2\ \mu m$. The droplets accelerate as the solidification front approaches, and decelerate as they are engulfed into the ice.

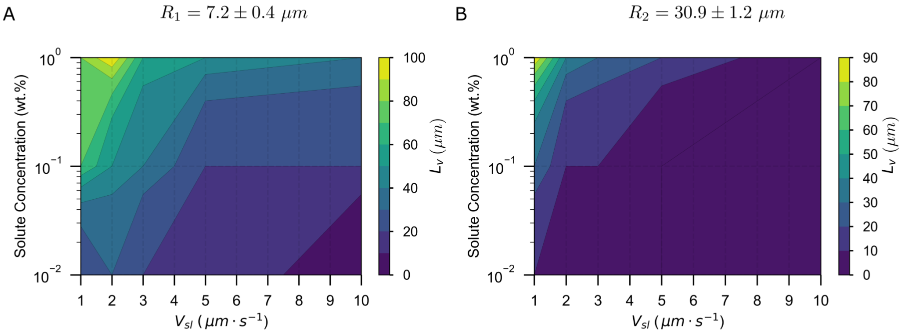

Figure 3.6: Characteristic length scale L_v in the plane of Solute Concentration ($wt.\%$) versus Solidification Velocity (V_{sl}). Contour plots denoting the magnitude of L_v for (A) $R_1 = 7.2 \pm 0.4\ \mu m$ and (B) $R_2 = 30.9 \pm 1.2\ \mu m$. Each contour line denotes a constant magnitude of L_v equivalent to the value shown on the calibration bar. The distance L_v, where droplets in water start getting repelled by the interface, increases significantly with the solute concentration, while it decreases with an increasing growth rate.

getting repelled at the approach of the solid-liquid interface. The mean droplet velocity ($\overline{U}$) increases and exhibits a maximum (U_{max}), when the leading edge of the droplets coincides with the initial position of the growing crystal. As the droplets are captured in ice, their velocity returns to zero. We distinguish the influence of the bulk solute concentration, the droplet size R and the growth rate V_{sl} on the mean droplet velocity $\overline{U}$ during freezing. $\overline{U}$ decreases with an increasing growth rate and larger droplet size, while it increases with an increasing amount of bulk solute concentration.

We define a characteristic length scale, L_v, distance from the interface at which the droplets attain a mean velocity ($\overline{U}$) of 0.1 $\mu m \cdot s^{-1}$, as shown in Fig.3.6. We find that the droplets get repelled over distances ranging between 10 and 100 μm, often larger than their diameter, especially for the largest solute concentrations. Smaller droplets with radius R_1 are repelled at greater distances from the interface as compared to the larger R_2 droplets. An increase in the solute concentration leads to higher values of L_v, however, increasing the growth rate decreases the characteristic distance L_v.

In Fig.3.7, we report on the evolution of U_{max} with the solute concentration, the droplet size, and the growth rate. Similar to $\overline{U}$ and L_v, we observe an increase of U_{max} owing to the strong influence of an increasing solute concentration. In contrast, an increasing growth rate leads to a decrease of the U_{max}. The smaller R_1 droplets get pushed away from the growing solid at higher velocities as compared to the larger R_2 droplets.

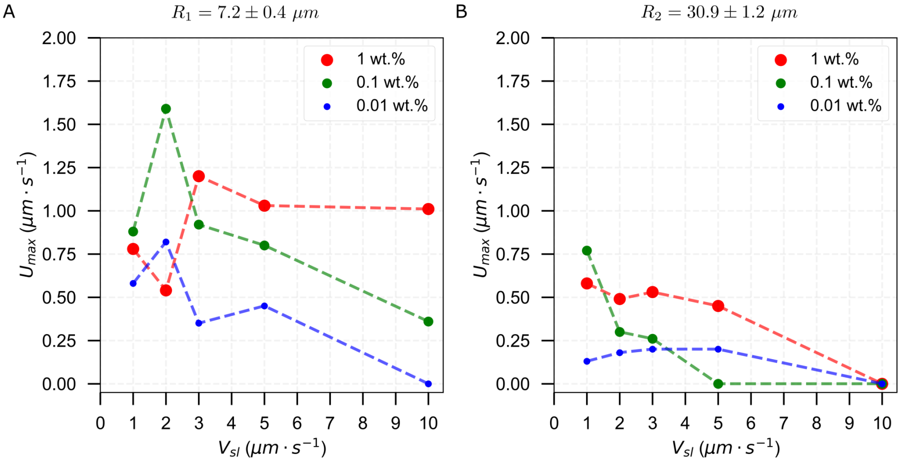

Figure 3.7: Maximum mean droplet velocity (U_{max}) when the droplet front edge coincides with the ice-water interface (distance to interface = 0 μm) for (A) $R_1 = 7.2 \pm 0.4\ \mu m$ and (B) $R_2 = 30.9 \pm 1.2\ \mu m$. In general, the magnitude of U_{max} is greater for higher solute concentrations and smaller droplet sizes. An increasing growth rate as well as droplet radius promote a smaller magnitude of U_{max}. The dotted lines are for visualization and do no represent an extrapolation of the results denoted by the circular markers.

To understand the impact of various solidification parameters on the droplet dynamics in water, we depict the interaction time (see Fig.3.14). This term includes the complete duration where the droplets in water interact with the solid-liquid interface, as shown in Fig.3.8. In general, we notice that the interaction time diminishes with an increasing solidification velocity (V_{sl}) and reduces to zero at higher growth rates ($V_{sl} \geq 5\ \mu m \cdot s^{-1}$), independent of the solute concentration. An interaction time of 0 s implies that the droplets get engulfed into the ice instantaneously and hence, do not interact with the advancing solid-liquid interface. In contrast, the interaction time increases strongly with the solute concentration at relatively lower growth rates ($V_{sl} \leq 3\ \mu m \cdot s^{-1}$). Consequently, the droplets undergo considerable horizontal displacement from their expected position in the presence of high solute concentration and at low solidification velocities. We demonstrate the droplet displacement owing to their interaction with an approaching ice-water interface in Fig.3.9. The droplet displacement, in other words, represents the distance moved by the droplets during the interaction time. We observe that the solute concentration and the imposed growth rate are the two most important criteria for determining the interaction time as well the displacement of a droplet in the presence of an approaching ice-water interface.

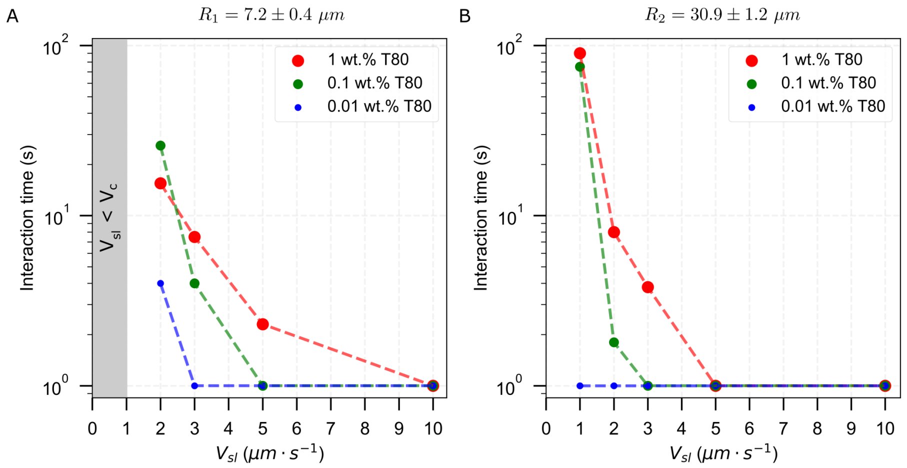

Figure 3.8: Interaction time for oil droplets dispersed in water at three distinct solute concentrations. Plot of characteristic interaction time for (A) $R_1 = 7.2 \pm 0.4\ \mu m$ **and (B)** $R_2 = 30.9 \pm 1.2\ \mu m$**. Droplets tend to interact or feel the presence of an approaching ice-water interface during** 10 **to** 100 s **at high solute concentrations** ($\geq 0.1\ wt.\%$) **and low growth rates** ($\leq 5\ \mu m \cdot s^{-1}$)**. The dotted lines are for visualization and do no represent an extrapolation of the results denoted by the circular markers.**

The results deduced so far emphasize that an increasing amount of solute induces large displacements and repulsion of the droplets over tens of microns away from the interface. Before characterizing the solute concentration profile close to the solidifying front and its influence on the droplet dynamics, let us

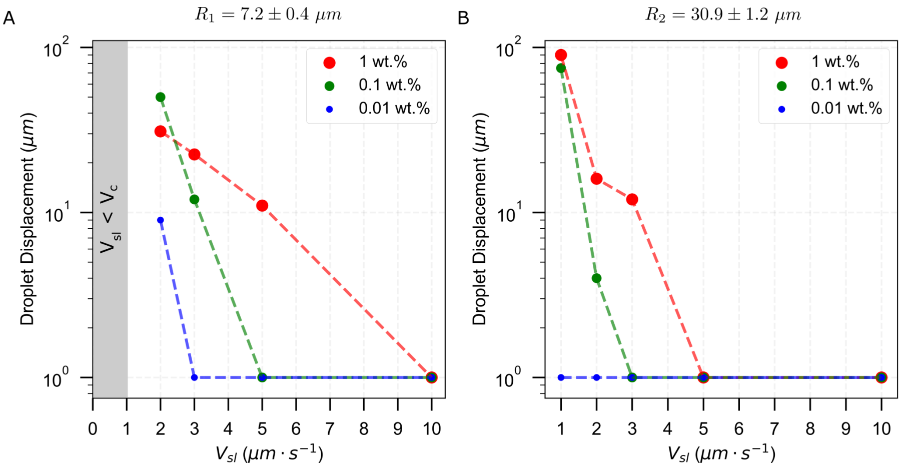

Figure 3.9: Displacement of oil droplets dispersed in water at three distinct solute concentrations, while interacting with the ice-water interface. Plot of droplet displacement for (A) $R_1 = 7.2 \pm 0.4\ \mu m$ and (B) $R_2 = 30.9 \pm 1.2\ \mu m$. The interaction of droplets with an advancing ice-water interface can displace them by increasing distances ($\geq 10\ \mu m$) owing to a high amount of solute ($\geq 0.1\ wt.\%$) in the bulk solution. The dotted lines are for visualization and do no represent an extrapolation of the results denoted by the circular markers.

comment on the previous literature models describing the interaction of a solidification front with particles. Most of these models did not include the influence of solute on the engulfment process. The initial studies performed by Chernov *et al.* [36, 37] laid the foundation for the thermomolecular force equilibrium approach for deriving a critical engulfment velocity (V_c), which is now generally accepted. The particle behaviour in vicinity of a solid-liquid interface is governed by the interplay between repulsive van der Waals and attractive viscous drag forces [36, 37]. Rempel *et al.* [23] developed further on this approach and deduced an analytical model to predict whether an isolated object will be engulfed ($V_{sl} < V_c$) or rejected ($V_{sl} > V_c$), by a moving solid-liquid interface. The value of V_c is given in table 3.1 for our experimental parameters using the model from Rempel *et al.*; $V_c = (\sigma_{sl} A_{ow}^2 / 6^5 \pi^2 \eta^3 R^4)^{1/3}$, where $\sigma_{sl} = 3 \times 10^{-2}$ ($J \cdot m^{-2}$) is the ice-water interfacial tension, $A_{ow} = 1 \times 10^{-20}$ (J) is the oil-water Hamaker constant, and $\eta = 1.8 \times 10^{-3}$ ($Pa \cdot s^{-1}$) is the dynamical viscosity of water.

In accordance with the model from Rempel *et al.* [23], isolated R_1 (7.2 ± 0.4) droplets at low solute concentration ($0.01\ wt.\%$) exhibit repulsion close to the interface at V_{sl} of 1 $\mu m \cdot s^{-1}$ and get engulfed at higher velocities $V_{sl} \geq 2\ \mu m \cdot s^{-1}$.

R (μm)	V_c ($\mu m \cdot s^{-1}$)
7.2 ± 0.4	1.35 ± 0.11
30.9 ± 1.2	0.19 ± 0.01

Table 3.1: Typical critical velocity for an isolated object encountering an ice-water interface, derived from Rempel *et al.* [23].

However, this theoretical model cannot account for the long-range repulsion between the droplets and the solidification front, observed in our experiments, at high solute concentrations (≥ 0.01 $wt.$%) for the two droplet sizes investigated.

The results presented so far underline that the droplet dynamics is influenced by the bulk solute concentration, the growth rate and the droplet size. These three parameters control the local gradient of solute concentration close to the solidification front. Indeed solutes present in the melt are rejected by the solid during freezing. The solid phase (here ice) has a low partition coefficient (K_0) in contrast to the liquid phase (here water) and hence, the solutes rejected by the solid segregate at the solid-liquid interface, as shown in Fig.3.10A. In a closed system, the solute concentration close to the solid-liquid interface is therefore higher as compared to the bulk solute concentration far from the interface. We also expect that the local gradient of solute concentration spans over a typical distance $L_d = D/V_{sl}$ in the *steady-state* regime [38].

An increasing growth rate (V_{sl}) will decrease the distance at which the solute field can be perceived by the droplets and can potentially explain the decreasing values of L_v measured (see Fig.3.6) at high growth rates ($V_{sl} \geq 5$ $\mu m \cdot s^{-1}$). Furthermore, we expect that the size of the droplets, which obstructs the solute diffusion close to the front, will also influence the gradient of solute concentration between the droplets and the front. As already explained in a previous article [19], we suggest that the displacement of the droplets is caused by solute concentration gradients close to the ice-water interface, possibly through a phenomenon called diffusiophoresis [39], according to which solute concentration gradients lead to displacement velocities of the order of microns per seconds, comparable to the droplet velocities that we measure in our study.

To further study the influence of the solute on the droplet dynamics, it would be useful to measure *in situ* the solute concentration close to the front. However, the solute employed in our experiments, Tween 80, does not fluoresce. Therefore, it is impossible to measure its concentration profile *in situ*. For *steady-state* planar growth, the concentration field of rejected solutes in the remaining liquid

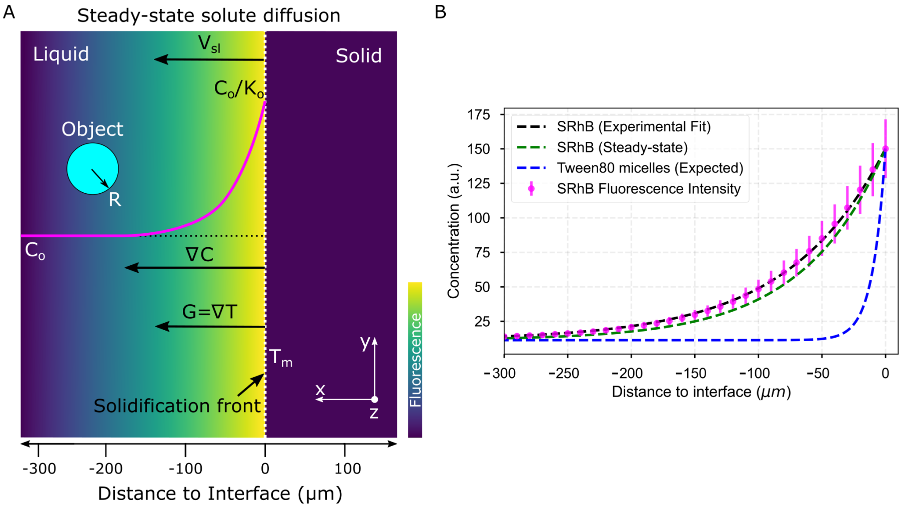

Figure 3.10: Solute rejected by the growing solid phase and segregated at the solid-liquid interface during *steady-state* directional solidification. (A) Model sketch depicting the concentration profile evolution of a solute (in magenta) in the remaining liquid, rejected by a solidification front advancing at V_{sl}, during *steady-state* planar growth. (B) Mean fluorescence intensity (magenta) of SRhB, acquired using a confocal microscope, is fit with a theoretical diffusion-type exponential (black line). The predicted *steady-state* diffusion of SRhB (green line), using the model from Tiller *et al.* [38], corresponds closely to the experimental data fit. A *steady-state* planar growth is thus verified. The corresponding *steady-state* diffusion profile of Tween 80 micelles (blue) shows a significant difference in length scales over which the two molecules (SRhB and Tween 80) diffuse. All data presented was recorded for a growth rate of $3\ \mu m \cdot s^{-1}$.

is given as

$$C_L = C_0 + C_0 \left(\frac{1 - K_0}{K_0} \right) exp \left[\frac{-V_{sl}}{D} x \right] \tag{3.1}$$

where C_L is the concentration, C_0 is the bulk solute concentration in the liquid far from the interface, D is the solute diffusion coefficient, and x is the distance from the interface [38]. To verify whether our experiments are performed in *steady-state* conditions, we record the fluorescence intensity of the dye, SRhB, which can be obtained easily with the confocal microscope (see Fig.3.10A). The concentration profile of SRhB rejected by the ice-water interface, deduced from the fluorescence intensity profile for a growth rate of $3\ \mu m \cdot s^{-1}$ is given in Fig.3.10B. At $3\ \mu m \cdot s^{-1}$, the concentration profile obtained is in agreement with the *steady-*

state diffusion profile predicted from Eq.3.1 (see Fig.3.10B). We note that the *steady-state* approximation is not valid at higher velocities (not shown) probably because constitutional undercooling modifies the local temperature of the front hence the diffusion coefficient of the dye.

Interestingly, at 3 $\mu m \cdot s^{-1}$, the distance at which the dye concentration profile starts increasing significantly is of the order of 150 μm. This value is much higher than the typical distance L_v over which both the large and small droplets get repelled from the interface. In Fig.3.6, the values of L_v range between 40 and 80 μm depending on the solute concentration and the droplet size. Although the solute monomer and the dye have the same diffusion coefficient, it is difficult to know whether the solute monomers behave as the dye, as we are above the *cmc* of the solutes in all cases and the excess of solute rejected by the ice may incorporate into the micelles rapidly.

An alternative possibility could be that the droplet dynamics is controlled by the concentration gradient of solute micelles instead of the concentration gradient of solute monomers. We measured the diffusion coefficient of the micelles and calculated the corresponding concentration profile using Eq.3.1. As shown in Fig.3.10B, at a growth rate of 3 $\mu m \cdot s^{-1}$, we obtain a typical distance L_d of 30 μm, which is slightly lower than the distance L_v measured experimentally at this growth rate.

3.3.2 Droplets at the interface

We now focus on understanding the behaviour of droplets when they come in contact (distance to interface = 0 μm) with the solid-liquid interface. We observe three typical behaviours of oil droplets as they encounter an approaching front, as shown in Fig.3.11. The droplets can elongate permanently as they get engulfed in the growing ice (Fig.3.11A), the droplets may deform transiently ($t = 13\ s$) at the ice-water interface and subsequently relax to their original spherical shape as they move further into the ice phase (Fig.3.11B), or the droplets can remain mostly spherical during their engulfment by the growing crystal (Fig.3.11C). We notice that the deformation behaviour depends on the droplet size R, the imposed growth rate V_{sl}, and the bulk solute concentration. Therefore, we need to systematically study the effect of these solidification parameters to understand the different types of deformation observed.

In light of the situation, the droplet deformation was estimated from the analysis of *2D* shape elongation, as shown in the schematic in Fig.3.11A, taking

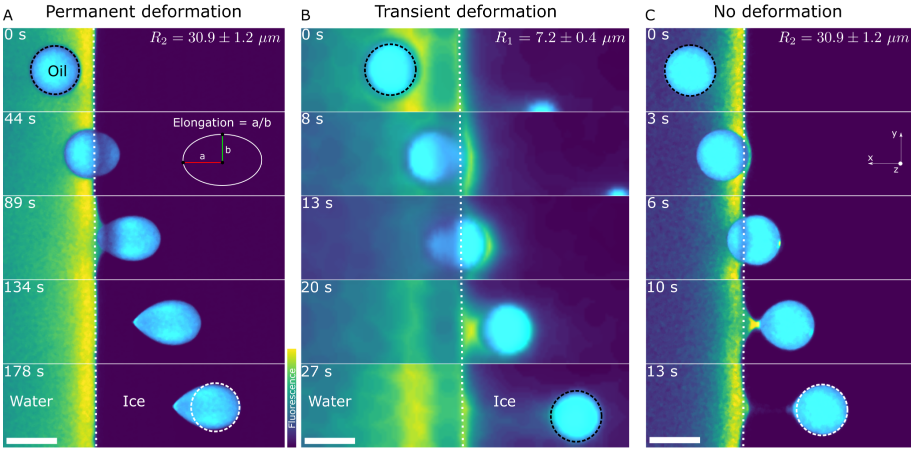

V_{sl} = 1 μm/s, 0.01 wt.% solute

V_{sl} = 3 μm/s, 1 wt.% solute

V_{sl} = 10 μm/s, 0.01 wt.% solute

Figure 3.11: Typical time-lapse montage depicting the three types of deformation behaviour of oil droplets while undergoing directional planar front solidification. (A) The droplets elongate at the ice-water interface and remain deformed in the ice phase, scale bar = $50\ \mu m$ **(B) The droplets deform in a transient manner (**$t = 13\ s$**) at the ice-water interface and recover their shape as they are captured by the growing ice phase, scale bar =** $10\ \mu m$ **(C) The droplets do not undergo deformation and preserve their shape during their interaction and further engulfment in the growing crystal, scale bar =** $50\ \mu m$**. Oil is in cyan, water is in colormap viridis (fluorescence bar), and ice is in black.**

the ratio of droplet diameters along $\vec{x}$ and $\vec{y}$. In Fig.3.12, we depict the mean elongation profiles calculated for 50 to 400 (depending on R and V_{sl}) droplet interactions in 0.01 $wt.\%$ and 1 $wt.\%$ solute solution at varying growth rates for two different droplet sizes (R_1, R_2).

We observe from Fig.3.12A and Fig.3.12B that the droplets undergo permanent elongation for the two droplet sizes (R_1, R_2), when the bulk solute concentration is 0.01 $wt.\%$. The elongation is ≈ 1.0, representing a circle, when the droplets are in the remaining liquid far from the interface. The droplets start getting elongated as their front edge touches the interface (distance = 0 μm) and their shape transforms into an ellipse (elongation > 1.0). The droplet deformation evolves further and reaches a constant magnitude when the front edge is located at a distance of $2R \times Elongation$. Once the droplets are completely engulfed in the ice, their shape does not evolve any more (Fig.3.12A,B). Interestingly, we notice that the elongation reduces with an increasing growth rate for both the droplet sizes investigated. However, the maximum elongation for the smaller R_1 droplets is lower as compared to the larger R_2 droplets at the given 0.01 $wt.\%$

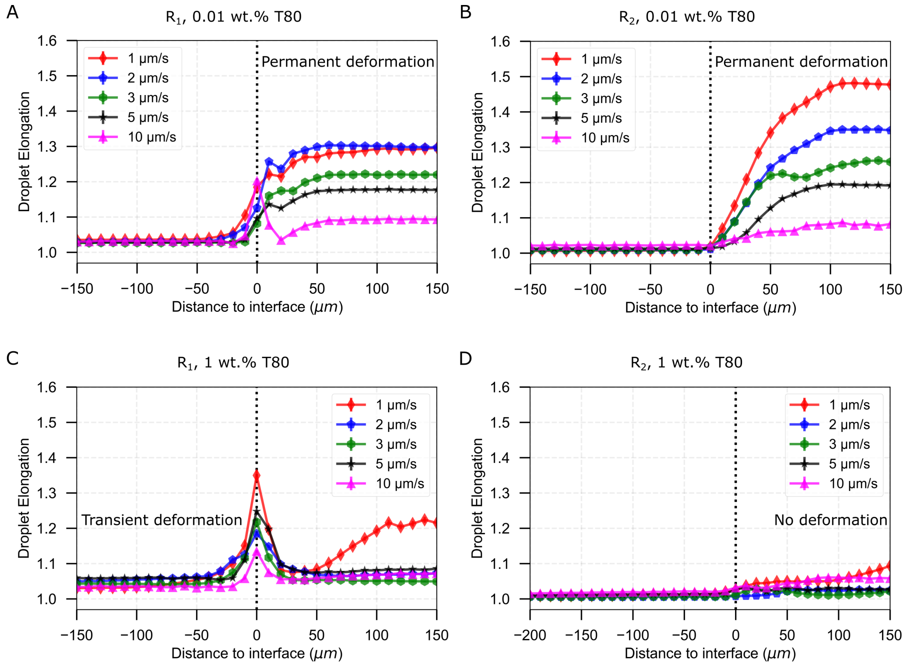

Figure 3.12: Mean elongation profiles for oil droplets encountering an approaching ice-water interface. Planar solidification front induced permanent deformation of oil droplets dispersed in a solution with (A,B) 0.01 $wt.\%$ **solute concentration having a size of (A)** $R_1 = 7.2 \pm 0.4\ \mu m$ **(B)** $R_2 = 30.9 \pm 1.2\ \mu m$**. The transient and no deformation regimes for droplets in (C,D)** 1 $wt.\%$ **solute concentration having a size of (C)** $R_1 = 7.2 \pm 0.4\ \mu m$ **(D)** $R_2 = 30.9 \pm 1.2\ \mu m$**.**

solute concentration.

In Fig.3.12C, we report the transient deformation of the oil droplets as they confront the ice-water interface with 1 $wt.\%$ bulk solute concentration. Here, the oil droplets undergo elongation at the interface (distance =0 μm) but eventually recover their shape as they are completely engulfed in the ice. In contrast, from Fig.3.12D we notice that the larger R_2 droplets do not undergo any type of deformation at the same solute concentration of 1 $wt.\%$. Hence, the elongation profile of R_2 droplets remains unmodified during the droplet-interface confrontation.

We deduce from these observations that the droplets confronting an approaching interface have distinct behaviours depending on the concentration of solute in the bulk solution. In particular, an increasing solute concentration tends to decrease the droplet elongation significantly. According to the *steady-state* diffusion model (see Eq.3.1), an increasing bulk solute concentration (C_0) implies a higher concentration of the solute segregated (C_0/K_0) at the solid-liquid interface (see Fig.3.10). The segregation of solute is further enhanced owing to an obstruction of their diffusion field by the foreign objects in the vicinity of the solid-liquid interface [13, 40]. The segregated solute, trapped in the layer between the droplet and the interface, induces solute premelting [41, 42], as shown in Fig.3.4B at $t = 44$ s, in Fig.3.11B at $t = 8$ s, and in Fig.3.11C at $t = 3$ s. The solute premelting is a colligative effect and occurs as a bulk phenomenon, whereby the equilibrium melting temperature of water is lowered by the presence of another component in the mixture, the solute Tween 80 in our case [38]. The driving force for the premelted films is a lowering of the surface free energy of the system [43].

The premelted films are stable below the solid's bulk melting temperature, T_m, and at sufficiently large solute concentrations, the thickness of the premelted films is dominated by the colligative effects [18, 41]. Thus, an increase in the thickness of the premelted films should also be instigated by an increasing growth rate owing to the reduced time available for solute diffusion. In our experiments, we observe that the droplet elongation decreases both with an increasing growth rate (see Fig.3.12A,B) and for higher bulk solute concentrations (see Fig.3.12C,D). In consequence, an increase in these two solidification parameters (C_0 and V_{sl}) also favors the formation of a thick solute segregation enhanced premelted film (see Fig.3.4B and Fig.3.11B,C). Hence, we suggest that the deformation of the droplets depends on the thickness of the solute invoked premelted films.

When a liquid droplet is in contact with another fluid, a curvature of the interface generates a Laplace pressure (ΔP), the pressure in the droplet being higher than in the surrounding bulk liquid phase. The lower the radius of curvature the higher the Laplace pressure. In the absence of any external force, the radius of curvature is constant and equal to the radius of the droplets leading to a spherical shape, thereby minimizing the surface energy of the system. In the presence of an external force, such as shear forces, the shape of a droplet is dictated by the balance between Laplace pressure and such external stress. The presence of a liquid-liquid interface between the droplet and the premelted film probably enables the recovery of a spherical shape which is driven by the Laplace pressure of the drop. Indeed the stress generated during the contact of the solid-liquid interface seems to induce the deformation of the premelted film rather than of the droplet. For example, in Fig.3.11C we observe that the premelted film-ice interface forms a highly curved neck during the droplet engulfment ($t = 10$ s), while the premelted film-droplet interface depicts a small curvature in comparison. In the absence of a thick premelted film around the droplet, the stress generated during the droplet-interface interactions are balanced by the large Laplace pressure corresponding to a higher elongation and curvature of the droplets (see Fig.3.11A). Furthermore, we believe the size effect in elongation for the same solidification parameters (C_0 and V_{sl}) arises from a difference in the associated Laplace pressure ($\Delta P \propto R^{-1}$) of the oil droplets. In Fig.3.12A versus Fig.3.12B, the smaller R_1 droplets manifest lower elongation owing to their relatively greater Laplace pressure in contrast to the larger R_2 droplets.

3.3.3 Droplets in ice

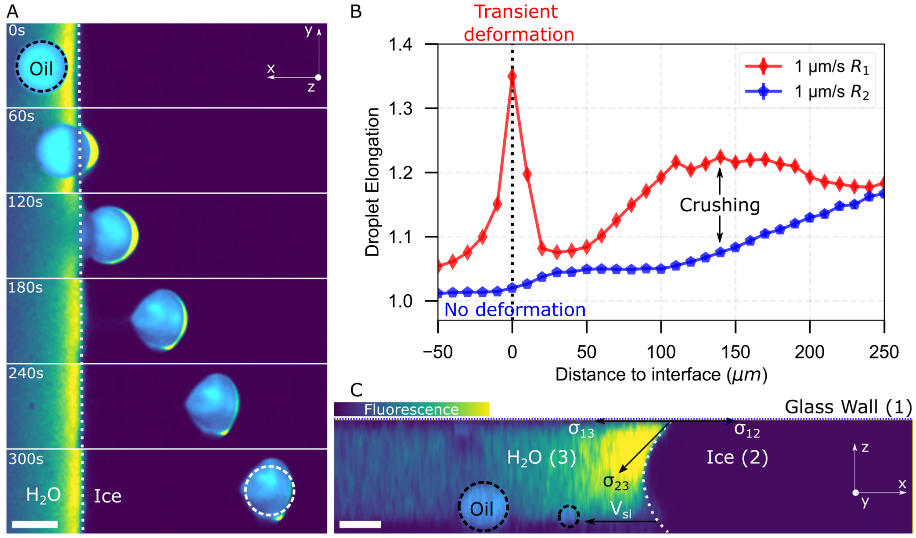

Figure 3.13: Crushing of oil droplets during their engulfment in ice at a growth rate of $1\ \mu m{\cdot}s^{-1}$ with $1\ wt\%$ solute in solution. (A) Typical time-lapse montage depicting the crushing of an oil droplet, scale bar = $50\ \mu m$ (B) Mean elongation profiles of R_1 and R_2 droplets increases monotonically with distance to interface proceeding their capture in ice (C) Orthogonal view (invariant along $\vec{y}$) of the ice-water meniscus at the given solidification parameters, scale bar = $20\ \mu m$.

We have discussed so far the dynamics and consequences of oil droplets interacting with an approaching ice-water interface. In the last section, we investigate the fate of objects and premelted films after their engulfment by the ice front. Previous results [19] have shown how the premelted films at the cells boundaries can destabilize into droplets. Here we focus on two additional behaviours: the crushing of the engulfed oil droplets, and their possible movement by regelation.

We first focus on the shape evolution of the oil droplets after they pass the water/ice interface. At 1 $wt.\%$ solute in the aqueous solution, we observe a distinct deformation behaviour of the droplets, which is different from the elongation reported previously. Here, the droplets undergo a monotonically increasing elongation, whereby the corresponding radii (along $\vec{x}$ and $\vec{y}$) are stretched in magnitude as the droplets progress further in ice. We depict this phenomenon of *crushing* with a time-lapse montage, highlighting the deformation debut at $t > 120\ s$, in Fig.3.13A. Interestingly, we observe this phenomenon with both $R_1 = 7.2 \pm 0.4\ \mu m$ and $R_2 = 30.9 \pm 1.2\ \mu m$ droplets, only at a growth rate of 1 $\mu m \cdot s^{-1}$ in the presence of 1 $wt.\%$ bulk solute concentration. Crushing can thus occur independently of how the droplets interact (no deformation or transient deformation) with the moving ice/water interface.

The mean elongation profiles of the two droplet colonies in Fig.3.13B emphasizes the monotonic nature of the deformation. This implies that the elongation continues to increase as the droplet moves further into the ice phase. We investigated the nature of the growing ice-water meniscus to understand the origin of the *crushing* phenomenon. To determine the exact three dimensional shape of ice inside the Hele-Shaw cell, we looked at the orthogonal projections (with $\vec{y}$ as an invariant) along the sample depth $\vec{z}$ (see Fig.3.13C). We can see from the orthogonal view along the vertical cross-section of a 3D image that the ice-water interface is curved.

The *crushing* phenomenon seems to be instigated by the curved morphology of the advancing ice-water interface. Ideally, one would expect to observe a concave ice-water meniscus owing to the interfacial excess energies between the solid, liquid, and the wall in a glass micro-capillary. The theoretical work of Acker *et al.* [44] and the experimental study from Liu *et al.* [45] have highlighted the role of solutes, in addition to the interfacial forces, in modifying the confined freezing behaviour. The sample cell used in our experiments has a depth of 100 μm and hence, we can expect a role of interfacial energies and solutes to be at the origin of the observed ice-water curvature. The solute rejected by the ice gets segregated at the interface and can diffuse over a length of 30 μm at the imposed growth rate. The increase in fluorescence intensity from the rejected die molecules ahead of the interface helps us to visualize the expected diffusion regime (see 3.13C). The aqueous solution in the vicinity is thereby enriched with the solutes and exhibits a varying osmotic pressure relative to the pure ice phase ($K_0 << 1$). Thus, we believe that the osmotic pressure gradient in conjunction with the differing interfacial energies (ice, water, and glass) might induce the observed ice-water concave meniscus. The curvature results in an excess of Laplace pressure in the ice phase, which could be at the origin of the observed *crushing* phenomenon.

Finally, regelation can occur, leading to a displacement of objects engulfed into the ice [46]. The droplets engulfed in ice with 1 wt% solute in solution (see Fig.3.4B, Fig.3.13A) are surrounded with a solute-rich premelted film forming a comet-tail segregation [19]. The liquid layer disjoins the droplet from the growing solid and decreases in thickness as the droplets move along the temperature gradient in ice towards an increasing undercooling ($\Delta T = T_m - T$, where T is the temperature of the substrate) [1]. The thermal fluctuations of the premelted layer are known to be at the origin of *regelation* of particles engulfed in a solid [47]. The thermal or pressure induced *regelation* can cause migration of particles through ice, whereby the particles translate towards the warmer side of the underlying ∇T, owing to a thermomolecular pressure gradient [42]. However, limited experimental data are available on regelation. Here, we do not observe *regelation* of the oil droplets at our experimental time-scales, probably owing to their large diameters. The objects known to exhibit significant regelation are micron-size or smaller. In our scenario, the droplets trapped in ice do not manifest any motion relative to the ice, as depicted in Fig.3.5. Additional work will be required to investigate in depth the possible regelation of oil droplets. More specifically, the use of smaller droplets (difficult to stabilize) will be required, as well as longer experiments with an immobile ice/water interface, more suitable to detect slow migration velocities.

3.4 Conclusions

In the first section, we have investigated the role of solutes on the dynamics of freezing oil droplets using *in situ* cryo-confocal microscopy. We have reported on the significant magnitude of droplet-front interaction time and the resulting droplet displacement owing to the solute effects. We believe this can be an important criterion for controlling the spatial distribution of objects, especially in multiple object scenarios. The control of the material microstructure has been a topic of interest in alloy solidification (especially in particle-reinforced-composites) and for impurity control in castings and single crystal growth. The object dynamics and impact of solute (or impurity) are still complex to quantify as the observation of solidification *in situ* remains challenging. We have tried to advance towards an *in situ* quantification of the solute mechanisms at play and further work is required to correlate the dye fluorescence intensity to the absolute solute concentration gradient. The latter can be useful in predicting thermal convection and non *steady-state* solidification regimes.

In the second section, we have shown that the deformation of droplets at the ice-water interface depends strongly on the growth rate (V_{sl}) and the corresponding bulk solute concentration (C_0). Furthermore, the addition of solute increases the thickness of the observable premelted films, which appears to act as a protection mechanism against the interface initiated droplet deformation. The local solute environment and deformation are two important criterion for cryopreservation in particular. In cryobiology, the excess of solute causes severe osmotic stresses that can instigate cell membrane rupture and hence, cryoinjury to cells and tissues [4, 12]. In food engineering, alterations to the continuous phase concentration or to the shape and size of dispersed droplets is detrimental to the freeze-thaw stability of consumable emulsions [8]. Hence, a complete understanding of the solute redistribution mechanisms along with the associated object deformation at the corresponding freezing conditions is desired. Our multi-dimensional approach highlights the importance of different solidification parameters and the ubiquitous role of solute in dominating the various aspects of object deformation behaviour. Further work is required to accurately estimate the direction and magnitude of forces at the origin of the observed deformation.

In the last section, we have demonstrated the crushing of droplets in the ice phase, when the ice-water meniscus is curved, owing to a low growth rate and high solute concentration. We have also reported an absence of thermal *regelation* for the oil droplets captured in the ice phase. The study of particle migration in ice is an important topic of research to understand frost heave, glacier motion, and ice-core dating among other technological applications [1]. Recent studies suggest that the presence of impurities or solutes tend to accelerate the *regelation* of trapped particles in ice. Typical migration velocities of 0.1 $\mu m \cdot s^{-1}$ at ΔT of 1 K have been reported for micron sized particles in the presence of impurities [48]. Another recent study highlights the major impact of impurities on the rapid displacement (0.5 cm) over small time scales (120 s) of 1 μm silicon particles trapped in ice [49]. The use of cryo-confocal microscopy with the ability to image the solute segregation has a promising prospect for investigating such mechanisms. We believe the high space and temporal resolution can be used effectively to resolve the dynamics of individual colloidal particles to gain further insight into *regelation*.

In conclusion, we report that the oil droplets undergoing directional solidification feel the impact of solute at every stage, from being in the liquid phase to getting captured by the growing ice-water interface. The solute plays an important role in determining the droplet shape (deformed or not), droplet behaviour (engulfment or rejection), and eventually the droplet spatial distribution. To predict the solidified microstructure, an understanding of the several in-situ mechanisms at play is therefore indispensable. The use of rapid cryo-confocal microscopy facilitates an *in situ* investigation and quantification of solidification mechanisms with visualization of the local solute segregation. To represent the observations in real-life systems, we need to explore models incorporating interaction dynamics and object behaviour with solute effects. Current theories do not encompass all the factors required for explaining the long-range solute effects on the objects during solidification. We hope our experimental data can serve to improve the existing theoretical models. Finally, we suggest that the freezing of oil-in-water emulsions may serve as an analogue for studying the *in situ* interaction of foreign objects with an advancing solid-liquid interface in the presence of solute effects.

3.5 Supplementary Information

We analysed the trajectories of all the oil droplets to obtain their apparent velocity (U') with varying distance from the interface, using the observation frame of reference. Time and distance 0 correspond to the moment and position where the front edge of each droplet hits the solidification front. In the observation frame, the solidification front is at a constant position, while the droplets move along the x-axis. The sample length of 4 cm corresponds to between 50 to 400 complete droplet trajectories depending on R and V_{sl} as shown in Fig.3.14. To transpose the data in the sample frame, we averaged the acquired droplet trajectories and performed the analysis as follows; $U_r = V_{sl} - U'$ as shown in Fig.3.15.

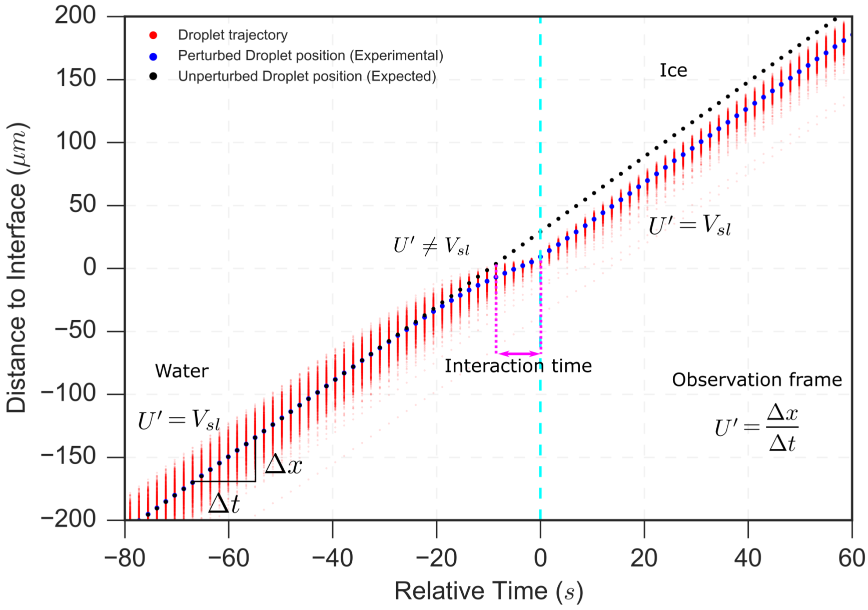

Figure 3.14: Measurement of interaction time and apparent droplet velocity U' in the observation frame. In the observation frame, far from the solid-liquid interface in water the droplet moves at the imposed growth rate $U' = V_{sl}$, as the droplet approaches the interface it gets repelled $U' \neq V_{sl}$, and as the droplet is engulfed in the ice it doesn't get repelled anymore, thereby recovering $U' = V_{sl}$. The interaction time is the total duration over which a droplet gets repelled by the solidification interface. Relative time is zero when the front edge of the droplet hits the solidification front. Experimental conditions for which the curve was recorded: $V_{sl} = 3\ \mu m \cdot s^{-1}$, $G = \nabla T = 10^4\ K \cdot m^{-1}$, Droplet size $R_1 = 7.2 \pm 0.4\ \mu m$.

The trends in our data for interaction time seem to be more statistically significant for the solute effects in contrast to the values of U_{max}. This is depicted also in Fig.3.15, where we distinctly underestimate the value of U_{max}.

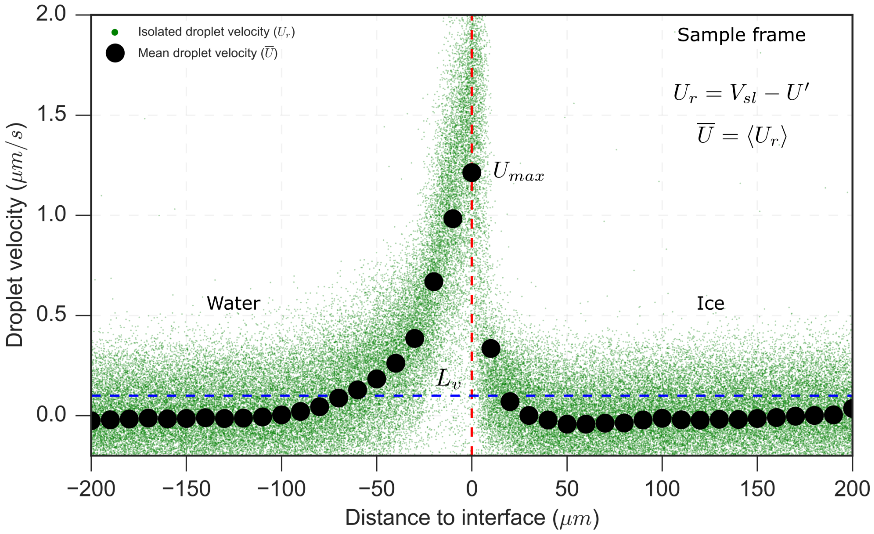

Figure 3.15: Deducing the isolated droplet velocity U_r and the mean droplet velocity $\overline{U}$ in the sample frame. In the sample frame, the isolated droplet velocity U_r is zero far from the interface, it increases and reaches a maximum when the droplet gets repelled by the interface and subsequently, reduces to zero as the droplet is engulfed in the ice. Experimental conditions for which the curve was recorded: $V_{sl} = 3\ \mu m \cdot s^{-1}$, $G = \nabla T = 10^4\ K \cdot m^{-1}$, Droplet size $R_1 = 7.2 \pm 0.4\ \mu m$.

Bibliography

[1] J. G. Dash, A. W. Rempel, and J. S. Wettlaufer. The physics of premelted ice and its geophysical consequences. *Reviews of Modern Physics*, 78(3):695–741, 2006.

[2] M Shafiur Rahman. *Handbook of food preservation*. CRC press, 2007.

[3] VL Bronstein, YA Itkin, and GS Ishkov. Rejection and capture of cells by ice crystals on freezing aqueous solutions. *Journal of Crystal Growth*, 52:345–349, 1981.

[4] C Körber. Phenomena at the advancing ice-liquid interface: solutes, particles and biological cells. *Quarterly reviews of biophysics*, 21:229–298, 1988.

[5] Lifeng Zhang. Nucleation, growth, transport, and entrapment of inclusions during steel casting. *Jom*, 65(9):1138–1144, 2013.

[6] H Li, EA Ghezal, A Nehari, G Alombert-Goget, A Brenier, and K Lebbou. Bubbles defects distribution in sapphire bulk crystals grown by czochralski technique. *Optical Materials*, 35(5):1071–1076, 2013.

[7] Sylvain Deville. Freeze-casting of porous ceramics: a review of current achievements and issues. *Advanced Engineering Materials*, 10(3):155–169, 2008.

[8] Supratim Ghosh and John N Coupland. Factors affecting the freeze–thaw stability of emulsions. *Food Hydrocolloids*, 22(1):105–111, 2008.

[9] OM Bunoiu, Th Duffar, and I Nicoara. Gas bubbles in shaped sapphire. *Progress in crystal growth and characterization of materials*, 56(3-4):123–145, 2010.

[10] D. Shangguan, S. Ahuja, and D. M. Stefanescu. An analytical model for the interaction between an insoluble particle and an advancing solid/liquid interface. *Metallurgical Transactions A*, 23(2):669–680, 1992.

[11] R. Asthana and S. N. Tewari. The engulfment of foreign particles by a freezing interface. *Journal of Materials Science*, 28(20):5414–5425, 1993.

[12] Gregory M. Fahy. The relevance of cryoprotectant "toxicity" to cryobiology. *Cryobiology*, 23(1):1–13, 1986.

[13] J. K. Kim and P. K. Rohatgi. The effect of the diffusion of solute between the particle and the interface on the particle pushing phenomena. *Acta Materialia*, 46(4):1115–1123, 1998.

[14] Adrian V. Catalina, Subhayu Sen, Doru M. Stefanescu, and William F. Kaukler. Interaction of porosity with a planar solid/liquid interface. *Metallurgical and Materials Transactions A*, 35(5):1525–1538, 2004.

[15] Sidhanth Tyagi, Hélène Huynh, Cécile Monteux, and Sylvain Deville. Objects interacting with solidification fronts: Thermal and solute effects. *Materialia*, 12(April):100802, 2020.

[16] Justin C. T. Kao and Alexander A. Golovin. Particle capture in binary solidification. *Journal of Fluid Mechanics*, 625(September 2008):299, 2009.

[17] Yi Yang, JW Garvin, and HS Udaykumar. Sharp interface numerical simulation of directional solidification of binary alloy in the presence of a ceramic particle. *International journal of heat and mass transfer*, 51(1-2):155–168, 2008.

[18] JS Wettlaufer and M Grae Worster. Premelting dynamics. *Annu. Rev. Fluid Mech.*, 38:427–452, 2006.

[19] Dmytro Dedovets, Cécile Monteux, and Sylvain Deville. Five-dimensional imaging of freezing emulsions with solute effects. *Science*, 360(6386):303–306, 2018.

[20] J. A. Sekhar and R. Trivedi. Solidification microstructure evolution in the presence of inert particles. *Materials Science and Engineering A*, 147(1):9–21, 1991.

[21] Jürgen Pötschke and Volker Rogge. On the behaviour of foreign particles at an advancing solid-liquid interface. *Journal of Crystal Growth*, 94(3):726–738, 1989.

[22] A. W. Rempel and M. G. Worster. Interaction between a particle and an advancing solidification front. *Journal of Crystal Growth*, 205(3):427–440, 1999.

[23] A. W. Rempel and M. G. Worster. Particle trapping at an advancing solidification front with interfacial-curvature effects. *Journal of Crystal Growth*, 223(3):420–432, 2001.

[24] Min S. Park, Alexander A. Golovin, and Stephen H. Davis. The encapsulation of particles and bubbles by an advancing solidification front. *Journal of Fluid Mechanics*, 560:415–436, 2006.

[25] P. S. Wei and S. Y. Hsiao. Pore shape development from a bubble captured by a solidification front. *International Journal of Heat and Mass Transfer*, 55(25-26):8129–8138, 2012.

[26] E. A. Ghezal, H. Li, A. Nehari, G. Alombert-Goget, A. Brenier, K. Lebbou, M. F. Joubert, and M. T. Soltani. Effect of pulling rate on bubbles distribution in sapphire crystals grown by the micropulling down (μ-PD) technique. *Crystal Growth and Design*, 12(8):4098–4103, 2012.

[27] H. Jamgotchian, R. Trivedi, and B. Billia. Interface dynamics and coupled growth in directional solidification in presence of bubbles. *Journal of Crystal Growth*, 134(3-4):181–195, 1993.

[28] S. Sen, W. F. Kaukler, P. Curreri, and D. M. Stefanescu. Dynamics of solid/liquid interface shape evolution near an insoluble particle - An X-ray transmission microscopy investigation. *Metallurgical and Materials Transactions A: Physical Metallurgy and Materials Science*, 28(10):2129–2135, 1997.

[29] F López Arbeloa, P Ruiz Ojeda, and I López Arbeloa. Flourescence self-quenching of the molecular forms of rhodamine b in aqueous and ethanolic solutions. *Journal of luminescence*, 44(1-2):105–112, 1989.

[30] Rex Malcolm Chaplin Dawson, Daphne C Elliott, William H Elliott, and Kenneth M Jones. *Data for biochemical research*, volume 3. Clarendon Press, 2002.

[31] Eleanor LV Harris, S Angal, and Simon Roe. *Protein purification applications: a practical approach*, volume 71. IRL press Oxford, 1990.

[32] Alan D McNaught, Andrew Wilkinson, et al. *Compendium of chemical terminology*, volume 1669. Blackwell Science Oxford, 1997.

[33] Johannes Schindelin, Ignacio Arganda-Carreras, Erwin Frise, Verena Kaynig, Mark Longair, Tobias Pietzsch, Stephan Preibisch, Curtis Rueden, Stephan Saalfeld, Benjamin Schmid, et al. Fiji: an open-source platform for biological-image analysis. *Nature methods*, 9(7):676, 2012.

[34] Stéfan van der Walt, Johannes L. Schönberger, Juan Nunez-Iglesias, François Boulogne, Joshua D. Warner, Neil Yager, Emmanuelle Gouillart, Tony Yu, and the scikit-image contributors. scikit-image: image processing in Python. *PeerJ*, 2:e453, 6 2014.

[35] Dmytro Dedovets, Cécile Monteux, and Sylvain Deville. A temperature-controlled stage for laser scanning confocal microscopy and case studies in materials science. *Ultramicroscopy*, 195(August):1–11, 2018.

[36] AA Chernov, DE Temkin, and AM Mel'Nikova. Theory of the capture of solid inclusions during the growth of crystals from the melt. *Sov. Phys. Crystallogr*, 21(4):369–373, 1976.

[37] AA Chernov, DE Temkin, and AM Mel'Nikova. The influence of the thermal conductivity of a macroparticle on its capture by a crystal growing from a melt. *Sov. Phys. Crystallogr*, 22(6):656–658, 1977.

[38] W. A. Tiller, K. A. Jackson, J. W. Rutter, and B. Chalmers. The redistribution of solute atoms during the solidification of metals. *Acta Metallurgica*, 1(4):428–437, 1953.

[39] JL Anderson, ME Lowell, and DC Prieve. Motion of a particle generated by chemical gradients. part 1. non-electrolytes. *J. Fluid Mech*, 117(1):107–121, 1982.

[40] R. Sasikumar and T. R. Ramamohan. Distortion of the temperature and solute concentration fields due to the presence of particles at the solidification front-effects on particle pushing. *Acta Metallurgica Et Materialia*, 39(4):517–522, 1991.

[41] J. Wettlaufer. Impurity Effects in the Premelting of Ice. *Physical Review Letters*, 82(12):2516–2519, 1999.

[42] A. W. Rempel, J. S. Wettlaufer, and M. G. Worster. Interfacial Premelting and the Thermomolecular Force: Thermodynamic Buoyancy. *Physical Review Letters*, 87(8):088501, 2001.

[43] JG Dash, Haiying Fu, and JS Wettlaufer. The premelting of ice and its environmental consequences. *Reports on Progress in Physics*, 58(1):115, 1995.

[44] Jason P. Acker, Janet A.W. Elliott, and Locksley E. McGann. Intercellular ice propagation: Experimental evidence for ice growth through membrane pores. *Biophysical Journal*, 81(3):1389–1397, 2001.

[45] Zhihong Liu, Ken Muldrew, Richard G. Wan, and Janet A.W. Elliott. Measurement of freezing point depression of water in glass capillaries and the associated ice front shape. *Physical Review E - Statistical Physics, Plasmas, Fluids, and Related Interdisciplinary Topics*, 67(6):9, 2003.

[46] M.J.M Römkens and R.D Miller. Migration of mineral particles in ice with a temperature gradient. *J. Colloid Interface Sci.*, 42(1):103–111, jan 1973.

[47] Gregory A Zielinski and Grant R Mershon. Paleoenvironmental implications of the insoluble microparticle record in the gisp2 (greenland) ice core during the rapidly changing climate of the pleistocene–holocene transition. *Geological Society of America Bulletin*, 109(5):547–559, 1997.

[48] Julia Schollick. *Real space study of pattern formation in freezing colloidal suspensions.* PhD thesis, University of Oxford, 2012.

[49] Navaneeth K. Marath and J. S. Wettlaufer. Impurity effects in thermal regelation. *Soft Matter*, 16(25):5886–5891, 2020.

Chapter 4

Multiple objects interacting with a solidification front

Abstract

The interaction of foreign objects suspended in a liquid melt with an advancing solidification front is of special interest in nature (e.g. frost heave) and engineering sciences (e.g. crystal growth). The front can engulf the object, trapping it into the growing crystal, or the front can repel the object, pushing it ahead of itself. Therefore, the object-front confrontation can have a strong influence on the properties of the solidified material. In particular, the spatial distribution of the objects in the resulting microstructure determines the material's structural and functional properties. The past theoretical models and experimental studies have mostly investigated the interaction of isolated, spherical, and hard objects in pure melts. However, the outcome of object-front interactions in complex (more realistic) systems, where multiple objects and solutes are present, is still poorly understood. Here we show the interaction of multiple oil droplets with an ice-water front in the absence and presence of solute effects using *in situ* cryo-confocal microscopy. We observe the formation of a compact agglomerated layer resulting in a force equilibrium different from the isolated object approach. We elucidate the role of solute during the evolution of a material microstructure in the presence of foreign objects. We report on how the object size, number of objects, and bulk solute concentration influence the front morphology and the subsequent object spatial distribution. Our results depict how the presence of multiple objects with varying solute concentration can modify the object-front interactions and hence, can lead to the formation of complex microstructures, difficult to predict theoretically. We suggest that the volume fraction of objects suspended in a liquid melt in conjunction with the amount of bulk solute concentration are two important criteria to be incorporated in the development of object-front interaction models. Furthermore, our simplified approach of using oil-in-water emulsions can serve as a good analogue for studying the development of material microstructure in presence of foreign objects.

Keywords: solidification, solute, inter-particle interactions, heterogeneous systems

4.1 Introduction

The interaction of objects (soft or hard) with a moving solidification front is a ubiquitous phenomenon with diverse natural and technical occurrences. In nature, the formation and growth of sea ice, frost heave in cold regions [1, 2], while the technological incidences include cryobiology [3, 4], food engineering [5], metallurgy [6], growth of single crystals [7, 8], and freeze-casting [9]. At the core of these physical processes are objects (particle, droplet, or bubble) encountering an approaching solid-liquid front. A major goal in understanding these systems is to elucidate the outcome of this interaction and predict not only the object behaviour (engulfment or rejection) but also the spatial distribution of objects after solidification. The solidification microstructures obtained owing to this object-front confrontation are vital as they govern the mechanical and functional properties of the solidified material. In metal-matrix-composites, a homogeneous distribution of reinforcing particles improves the structural properties, while a particle segregation along the grain-boundaries is detrimental to their performance [10]. In contrast, an *in situ* evolution and trapping of gas bubbles in metals and single crystals can lead to their catastrophic failure and hence, a total rejection of bubbles is desired [11].

The first systematic measurements of particle interaction with an advancing ice-water front were conducted by Corte [12]. The objective of his experiments was to study the influence of an increasing growth rate (V_{sl}) on particle capture by the growing solid. Studies performed subsequently on the interaction of a single isolated object with a solidification front, deduced a critical velocity (V_c), the growth rate below which an object is pushed ($V_{sl} < V_c$), while the object is engulfed by the growing solid above it ($V_{sl} > V_c$) [13, 14]. The previous studies report that the precise value of V_c depends on several factors, comprising of the particle radius R, the temperature gradient G, and the physical characteristics of the particle-melt-crystal system [15, 16, 17]. In general, $V_c \propto R^{-\alpha}$ where α varies ($1 \leq \alpha \leq \frac{3}{2}$) owing to an interplay between the viscous drag forces (F_η), which promote capture, and the thermomolecular forces (F_σ), which favor repulsion of the object through a premelted film [16, 17, 18, 19].

A plethora of work has been performed to determine theoretically the magnitude of these opposing forces, which have a major dependence on the shape of the solidification front [10, 20, 21]. The studies only differ in the theoretical approximations used (e.g. boundary conditions) and mainly deal with an isolated, smooth, spherical, and rigid particle of radius R moving ahead of a planar front in *steady-state* (i.e. $F_\eta = F_\sigma$) directional solidification [15]. The *in situ* experimental correlations of these analytical and numerical models are, however, still scarce owing to the numerous complexities associated with solidification, such as multiplicity of space- and timescales [4, 11, 15, 22, 23, 24, 25]. Furthermore, the idealistic assumptions of the theoretical models such as the non-retarded van der Waals forces, absence of solute segregation, and a *steady-state* planar front interaction are difficult to achieve practically [26]. The advent of accurate finite element models also clearly highlights the disparities in approximations to solidification front shapes and the accuracy of the simulated particle behaviours [27].

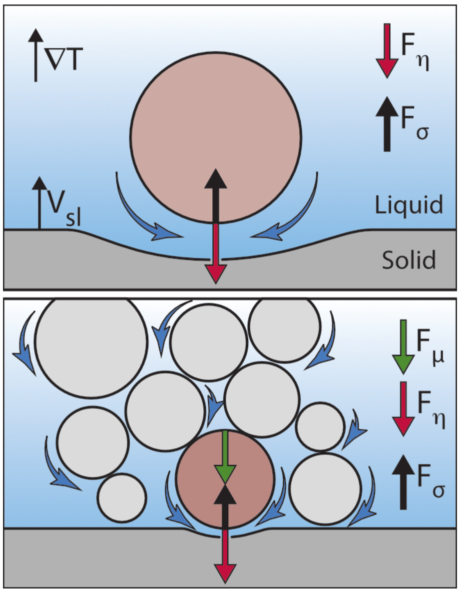

Figure 4.1: Force equilibrium to predict engulfment or rejection of objects in the presence of multiple particles. The particle-particle interactions during solidification can result in the formation of a compact layer, which acts as a porous medium. The subsequent resistance offered to the flow of fluid (blue arrows) towards the growing solid results in an additional frictional force F_μ, which favors object engulfment. The modified force equilibrium is hence given as $F_\eta + F_\mu = F_\sigma$, where F_η is an attractive viscous drag force and F_σ is a repulsive interfacial force. $\nabla T = G$ is the applied temperature gradient and V_{sl} is the imposed growth rate.

The existing theories and experimental evidences have been primarily derived for isolated, hard, and smooth spherical objects, whereas most real-life applications involve multiple particles with arbitrary shapes and surface roughness. This reinforces the importance of investigating the role of particle size distribution, particle-particle interactions and hence, the formation of agglomerates. Progress in studying the spatial distribution, when thousands of particles interact with a solid-liquid front, has been brought about by modern advanced *in situ* imaging techniques, such as X-ray imaging [28], confocal microscopy [29], or the development of numerical modelling techniques, such as molecular dynamics [30, 31]. Recently, Saint-Michel *et al.* [32] proposed a mechanical model on the effects of multiple particle interactions on particle trapping by solidification fronts as depicted in Fig.4.1. Their study highlighted the major differences in force equilibrium when considering a multi-particle approach. The model suggested that the presence of multiple particles can lead to an accumulated particle layer ahead of the solidification front at small growth rates ($V_{sl} < V_c$). This particle layer further acts as a porous medium and offers resistance to the fluid flow resulting in an additional frictional force (F_μ), which facilitates particle engulfment. Hence, the modified force equilibrium for multiple-particles can be given as $F_\eta + F_\mu = F_\sigma$. Although, these studies help us to bridge the gap between the single particle models and real-life multi-particle systems, yet the underlying questions concerning the evolution of solidified microstructure with the associated complex front morphology remain unresolved.

The presence of solutes, desired or as impurities, impacts the solidification front shape and induces long-range effects ($\approx D/V_{sl}$, where D is the solute diffusion coefficient), which override the short-range thermomolecular forces ($\leq 10\,nm$). The existing models, incorporating the role of solute, study their influence on the solid-liquid front shape deformation but not on the nature and equilibrium of the repulsive forces [19, 21, 33, 34, 35]. In general, the solubility of a solute is less in the solid phase than in the liquid phase. As solidification progresses, the solute is rejected by the growing crystal, thereby corresponding to an increasing concentration of solute in the remaining liquid [36]. In the presence of foreign objects, the segregation of solutes at the front is enhanced further by the approaching objects obstructing their diffusion field [21]. This local solute enrichment influences the object environment (viscosity, undercooling, and phoresis) and is of particular importance in understanding several mechanisms that can occur at the solid-liquid front. The rejection of additives during the freezing of biological cells can inflict membrane rupture (or cryoinjury) owing to the high osmotic stress gradient from the local solute concentration [3, 4]. The nucleation and growth of bubbles leading to macroporosity defects is instigated when the concentration of gases rejected (like solutes) by the growing solid exceeds a certain value [11, 37].

The objective of our study is to investigate experimentally the solidification dynamics and spatial distribution of objects in multiple particle regimes. We compare our experimental observations with previous theoretical models to comprehend the critical correlations and disparities in the presence of multiple particles. We perform directional solidification experiments with independently regulated solidification velocity (V_{sl}) and a linear temperature gradient (G). The use of freezing emulsions as model system for solidification has been promising [38] and we develop further on this approach using *in situ* cryo-confocal microscopy. We utilise mono-disperse, bimodal emulsions, and subsequently progress towards realistic poly-disperse systems. We demonstrate several important aspects of multiple particle interactions and its consequences on particle redistribution in the solidified microstructure. We increase the complexity by adding solute to the liquid phase, and examine the effects of increasing polydispersity in conjunction with the overriding solute effects. Finally, we illustrate how the systematic approach facilitates to decouple the process parameters impacting the behaviour of an object, while it interacts with a solid-liquid front.

4.2 Experimental Methods

4.2.1 Materials

We purchased propyl benzoate, TWEEN 80, Difluoro2-[1-(3,5-dimethyl-2H-pyrrol-2-ylidene-N)ethyl]-3,5-dimethyl-1H-pyrrolato-Nboron (BODIPY), and Sulforhodamine B (SRhB) from Sigma-Aldrich. We utilised 0.45 μm Nylon membrane filters (VWR International) for filtering traces of impurities in the deionized water used for the aqueous phase. We chose propyl benzoate for the oil phase as it has a low melting temperature ($T_m = -51.6° C$), low solubility in water ($0.035\, g/100\, g$), and similar density to water ($\rho_{oil} = 1.023\, g \cdot cm^{-3}$).

4.2.2 Sample Preparation

We prepared oil-in-water emulsions using a microfluidic setup (microfluidic starter kit, Micronit Microfluidics, Netherlands) with pressure controlled flow pumps (Fluigent LineUP Flow EZ). We used uncoated focused flow droplet generator chips (FF_DROP, Micronit) with nozzle diameter of $10\, \mu m$ and $50\, \mu m$. These microfluidic chips facilitated the preparation of highly monodisperse droplets with radii of $8\,\mu m$ (R_1) and $28\,\mu m$ (R_2), respectively. We ensured a uniform flow rate of oil and aqueous phases using Fluigent Flow Unit S ($0-7\,\mu L/min$) combined with in-line impurity filters (PEEK $2\,\mu m$,VWR International). The oil phase consisted of propyl benzoate with $10^{-4}\,M$ BODIPY to obtain clear imaging of dispersed droplets at 1% laser power. For the aqueous phase, we used $10^{-5}\,M$ SRhB solution, as self-quenching was reported at concentrations above $2\times10^{-4}\,M$ [39]. We added TWEEN 80 ($HLB = 15$ [40]), a non-ionic surfactant, to the aqueous phase for stabilising the oil-in-water emulsions. TWEEN 80 (Critical Micellar Concentration = $13-15\,mg\cdot l^{-1}$ [41]), acted as a model solute as it depresses the freezing point of solutions alike (colligative property). The bimodal emulsions were synthesized by independently mixing the monodisperse emulsions ($R_1 + R_2$). The polydisperse emulsion was obtained through hand-shaking the aqueous suspension in a $1.5\,ml$ eppendorf vial with $2\,vol.\%$ oil phase. The prepared emulsions were filled through capillarity and solidified in a rectangular Hele-Shaw cell (h=$100\,\mu m$ and V=$100\,\mu l$). The cell was fabricated using two glass slides (Menzel, $24\times60\,mm$, thickness $0.13-0.16\,mm$), and sealed with nail-polish at one end to prevent evaporation.

4.2.3 Imaging & Analysis

We used Leica TCS SP8 confocal laser scanning microscope (Leica Microsystemes SAS, Germany), equipped with $488\,nm$ (blue) and $552\,nm$ (green) lasers, for image acquisition. In *2D*, we utilised the microscope at a scanning speed of $600\,Hz$, with $1024\times1024\,pixels$ for imaging $775\times775\,\mu m$, resulting in $1.7\,s$ per frame. In *3D*, we used a fast resonant mode with $512\times512\,pixels$ for a scanning rate of $0.047\,s$ per frame. We used two photodetectors (PMT) to simultaneously image three phases :

1. BODIPY (λ_{ex} $493\,nm$; λ_{em} $504\,nm$), fluorophore incorporated into the oil droplets.

2. SRhB (λ_{ex} $565\,nm$; λ_{em} $586\,nm$), fluorophore dissolved in water, to image the aqueous phase and the grain boundaries in ice.

3. Ice, does not fluoresce, as it has very low solubility for solutes [42] and hence, appears black.

The emission spectra of the excited fluorophores was captured using a non-immersive objective (Leica HCX PL APO CS 20×). The objective working distance of 590 μm along with an insulating foam cladding facilitates the minimization of thermal perturbations on the freezing substrate. We used Fiji [43] for image thresholding in conjunction with Python [44] for image and data analysis.

4.2.4 Freezing Stage

We conducted unidirectional solidification experiments, translating the sample cell along a constant linear temperature gradient (G), using the cryo-confocal stage described in detail previously [29]. We imposed the temperature with two Peltier modules, and controlled it with high precision ($< 0.01\,°C$) using TEC-1122 Dual Thermo Electric Cooling Temperature Controller from Meerstetter Engineering, Switzerland. The Peltier elements were separated by a distance ($2\,mm$) to establish a linear temperature gradient along $\vec{x}$. We utilised the VT-80 translation stage (Micos Pollux Drive PI, USA) to impose the rate at the which the sample cell is pulled (V_{sl}). The rate of translation was verified to be in agreement with the measured solidification velocity using posterior image analysis ($error < 1\,\%$). Thus, we can control independently the solidification velocity (V_{sl}) and the thermal gradient (G) in our system. We carried out the experiments in the velocity range of $1 \le V_{sl} \le 10\,\mu m \cdot s^{-1}$, with sufficient waiting time to establish thermal equilibrium along the sample depth ($\vec{z}$). The *in situ* observation of object interaction with the solid-liquid front was captured using a confocal microscope placed vertically over the gap ($2\,mm$) between the two Peltier modules. Hence, the solidification front tends to appear immobile in the frame of observation, however, in the sample frame, it is the ice solidifying (along $\vec{x}$) at the velocity imposed by the pulling rate of the motor.

4.3 Results

4.3.1 Front Morphology

We study the directional solidification of oil-in-water emulsions, translated at a velocity V_{sl} along a linear temperature gradient G, using a confocal microscope, as shown in Fig.4.2. A typical confocal image, as shown in Fig.4.3, enables us to distinguish the dark solid phase (ice) from the bright aqueous phase (H_2O). Ice, like most solids, has extremely low solubility for dissolved solutes and rejects

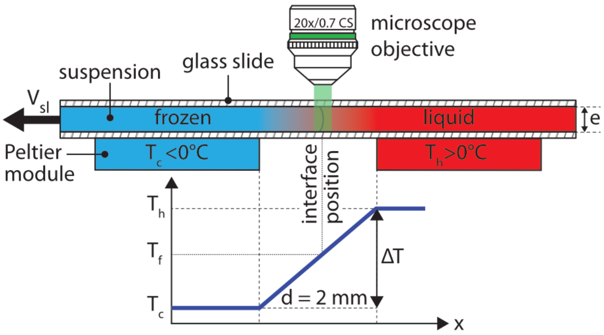

Figure 4.2: Experimental setup for *in situ* solidification experiments. A thin Hele-Shaw cell containing the droplets in suspension is pulled at a constant velocity (V_{sl}) through a constant temperature gradient (G) established by Peltier elements. In steady state, the solidification front is thus at a constant position under the microscope objective.© (2020) S. Tyagi *et al.* (10.6084/m9.figshare.12046560) CC BY 4.0 license https://creativecommons.org/licenses/by/4.0/.

them in the remaining liquid as solidification progresses [42]. The coexisting solid-liquid phases are delimited by the solidification front, corresponding macroscopically to an isotherm at bulk melting temperature T_m.

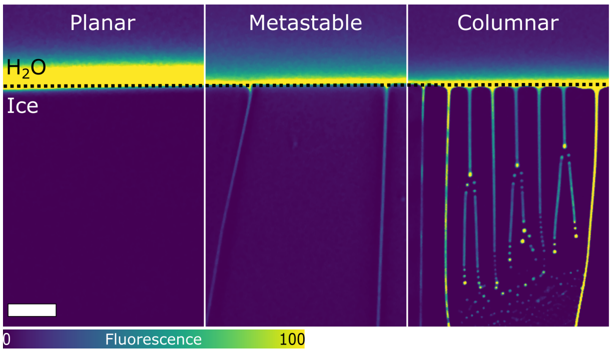

Figure 4.3: Typical confocal images of directional solidification depicting different front morphologies; planar, metastable, and columnar. Confocal image enables us to distinguish the dark solid phase (ice) from the bright aqueous phase (H_2O). Water is in colormap viridis (fluorescence bar) while ice is in black. Scale bar = 100 μm**.**

In directional solidification, the advancing solid-liquid front can have predominantly three morphologies; planar, cellular (or columnar), and dendritic (Fig.4.3). The stability and morphology of a front are essentially controlled by the growth rate, the underlying temperature gradient, and the solute concentration in the melt. The major advantage of our system is that we can independently regulate and accurately maintain a constant solidification velocity (V_{sl}) as well as temperature gradient (G) over the experimental time-scales. This ensures a *steady-state* solidification front under a constant cooling rate with the absence of thermal destabilisation.

To establish the domains of different front morphology, we performed experiments using a constant thermal gradient G of $10^4\,K \cdot m^{-1}$, as shown in Fig.4.4. We observe three distinct front morphology (Fig.4.3,C), in the absence of suspended objects, while solidifying the aqueous phase in a velocity range of $1 \leq V_{sl} \leq 10\,\mu m \cdot s^{-1}$, with varying concentrations of solute. In Fig.4.4, the *steady-state* planar front is thermodynamically favorable at low growth velocities ($V_{sl} \leq 5\,\mu m \cdot s^{-1}$) for small solute concentrations ($\leq 10^{-1}\,wt.\%$). As we increase the front velocity or the solute concentration, the steady state planar front develops local growth instabilities with a few grain boundaries, which remain stable during experimental time scales $\approx 40-60\,min$. At the higher velocities and solute concentrations, the front eventually destabilises into a columnar front morphology. The uniformly spaced lamellae are generated owing to the propagation of a Mullins-Sekerka instability during the solid-liquid phase transformation [45].

The solute rejected by the growing ice front builds up a steep concentration gradient with the bulk solution, over a length scale ($\approx D/V_{sl}$) [21, 23] . Since growth from solutions depends on the concentration gradient of solutes, the liquidus temperature of the melt in the vicinity of the front differs from the liquidus temperature of the bulk liquid far from the front. As the solute segregates, the liquidus temperature further decreases. This change in liquid composition alters its transformation temperature, referred to as constitutional undercooling [36]. This constitutional undercooling is a necessary criterion for the destabilization of a planar front into a metastable or columnar front [45]. Theoretically, for *steady-state* planar front growth the solute concentration gradient in the melt scales as $\nabla C \propto e^{-V_{sl}x/D}$, where x is the distance from the solidification front [36]. Therefore, an increasing growth rate leads to a strong increase of the solute concentration gradient. This explains why the critical bulk solute concentration for the destabilization of a planar front decreases with an increasing growth rate, as reported in Fig.4.4.

The spatial distribution of the objects in the solidified material is determined by the advancing front morphology obtained at the given experimental conditions [23, 46]. In ice-templating, a columnar front is used to segregate the

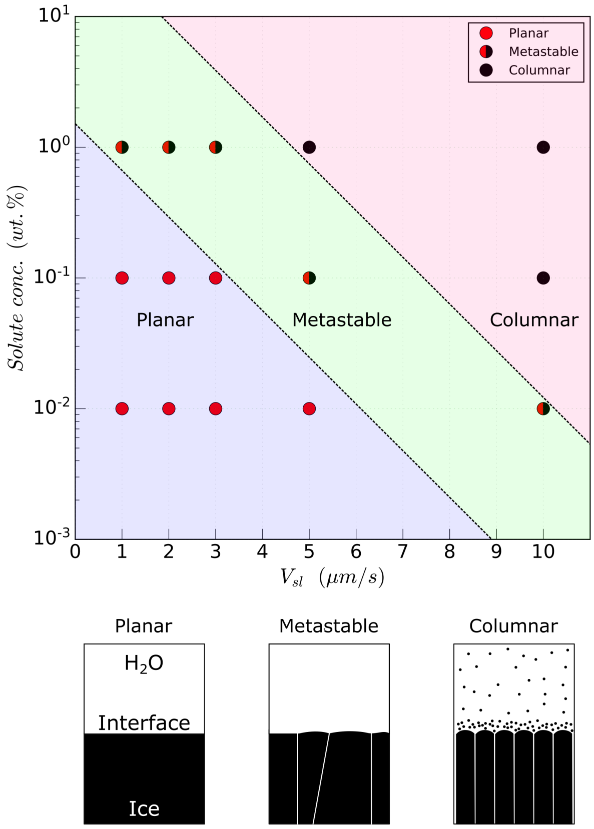

Figure 4.4: Front morphologies obtained during the directional solidification of an ice-water system in the solute concentration versus growth rate (V_{sl}) plane, at a constant thermal gradient of $10^4\,K\,m^{-1}$. A *steady-state* planar front (A) gets destabilised partially, with an increasing growth rate and solute concentration, to a metastable front (B) exhibiting a few grain boundaries, and eventually forms a cellular front (C) for the higher solute concentrations ($\geq 10^{-1}$ wt.%). Broken lines are drawn to differentiate the three zones distinctly and do not imply an extrapolation of the experimental data.

dispersed colloids between the arms of the growing ice crystals [9]. In contrast, the growth of single crystals demands a planar front to ensure a homogeneous structure [7]. We thus feel it is important to investigate the systematic impact of object size, solute concentration, and inter-object interactions on the solidified microstructure with planar and meta-stable fronts. We do not investigate the specific case of columnar and dendritic fronts to avoid comparison, while modifying multiple solidification parameters simultaneously. This implies that we modify only the bulk solute concentration, while keeping a constant growth rate of $1\,\mu m \cdot s^{-1}$ and a constant temperature gradient of $10^4\,K \cdot m^{-1}$ during our experiments.

4.3.2 Interaction of monodisperse objects

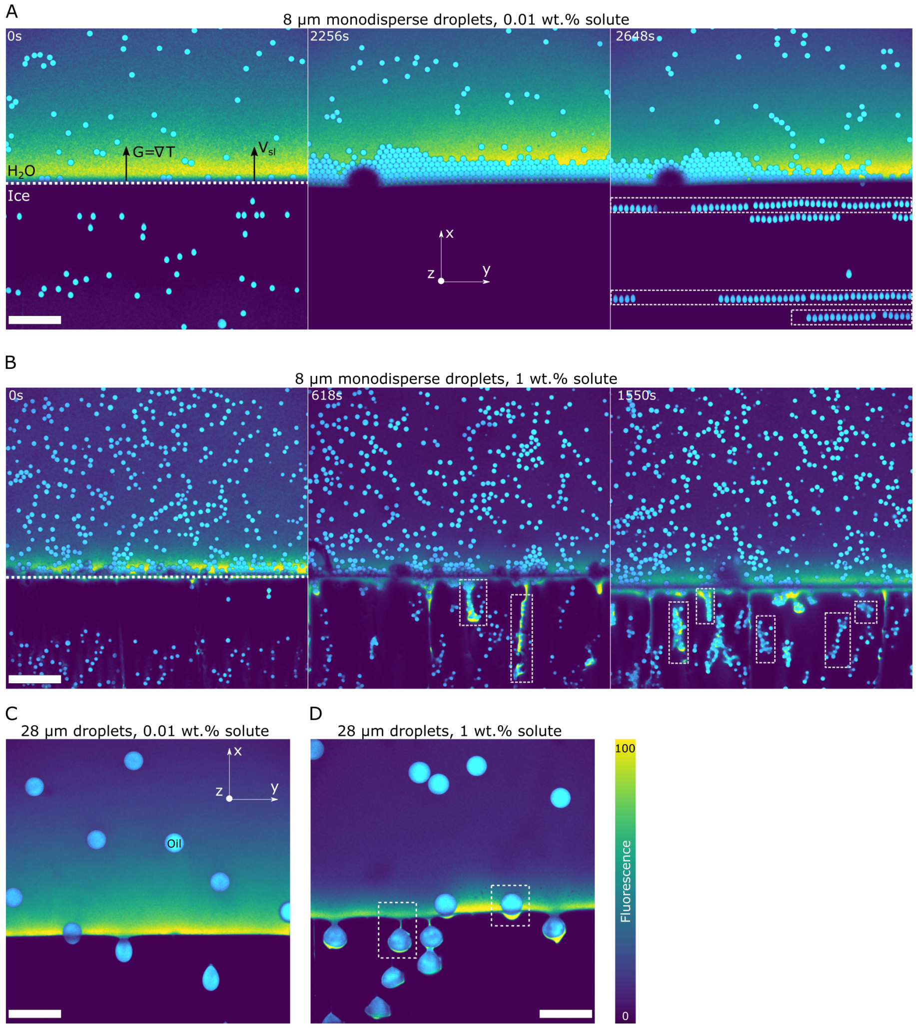

Figure 4.5: Interaction of monodisperse oil-in-water emulsion with an advancing ice-water front. Solidification induced features and spatial distribution of oil droplets depicting (A) Horizontal mono-layers and stable planar front with $8\,\mu m$ (R_1) at $0.01\,wt.\%$ solute, (B) Vertically aligned clusters and local front destabilisation with $8\,\mu m$ (R_1) at $1\,wt.\%$ solute, (C) No clusters and stable planar front with $28\,\mu m$ (R_2) at $0.01\,wt.\%$ solute, and (D) Rejected solute segregation and local front destabilisation from solute premelted films with $28\,\mu m$ (R_2) at $1\,wt.\%$ solute. Oil is in cyan, water in colormap viridis (fluorescence bar) while ice is in black. Scale bar = $100\,\mu m$.

We first examine the interaction of monodisperse oil-in-water emulsions with the solid-liquid front at a growth rate of $V_{sl} = 1\,\mu m.s^{-1}$ and a temperature gradient of $G = 10^4\,K \cdot m^{-1}$, as depicted in Fig.4.5. The corresponding droplet size and bulk solute concentration used for the experiments are given in table 4.1.

Figure 4.5	R (μm)	$Solute\,conc.$ ($wt.\%$)
A	8	0.01
B	8	1.00
C	28	0.01
D	28	1.00

Table 4.1: Droplet radius (R) and bulk solute concentration ($wt.\%$) in the aqueous phase for the monodisperse oil-in-water emulsions.

In Fig.4.5A, we observe that the $8\,\mu m$ (R_1) oil droplets with 0.01 $wt.\%$ solute concentration are continuously repelled by the ice growing from the bulk suspension, forcing them to build-up as a compacted layer. In our experiment, the height of the close-packed layer increases until $\approx 80\,\mu m$ and subsequently, the droplets get engulfed by the growing solid. Interestingly, the droplets are engulfed as single layers and fabricate a texture parallel to the solid-liquid front. The droplets though closely packed in the liquid ahead of the front, get separated as they are captured by the growing ice crystal. We believe the lateral gap ($\vec{y}$) between the engulfed droplets in ice is created owing to the elongation induced during their capture. The increase in diameter parallel to the temperature gradient ($\vec{x}$) is compensated by the decreasing width in the lateral direction ($\vec{y}$) and hence, the close-packed droplets get separated in the frozen solid. In contrast to the smaller R_1 droplets (Fig.4.5A), the engulfment of the larger R_2 ($28\,\mu m$) droplets is instantaneous and we observe no subsequent compact layer formation (Fig.4.5C). The elongation induced owing to the droplet-front interaction is visually prominent during the solidification of the R_2 droplets. The deformation of droplets during solidification will be addressed in a separate communication and is not in the scope of the present study. The *steady-state* planar front remains stable and does not destabilise neither from the formation of the close packed layer nor during the capture of the different size objects (Fig.4.5A,C).

The presence of a similar particle agglomerated layer has been reported previously [32, 47, 48], where its *steady-state* thickness (h) depends primarily on the solidification velocity ($h \propto V_{sl}^{-1}$). Therefore, the complex scenario of multiple particles can be partly understood by building on the single-particle models. At 0.01 $wt.\%$ concentration, the solute does not play a dominating role and hence, we shall compare this system to the previous theoretical models derived for single isolated objects. In general, when an isolated object is relatively close to the solidification front ($< 100\,nm$), non-retarded van der Waals forces are effective and tend to push the object away from the front. This inter-molecular interaction generates the need to maintain a stable liquid film (to prevent contact) between the object and the growing crystal and results in a repulsive disjoining pressure. The viscous drag force (F_η), emanating from the fluid flow in the particle-front gap to satisfy the mass balance, counteracts the inter-molecular force (F_σ) and favours engulfment of the object. Therefore, the object behaviour (engulfment or rejection) in the vicinity of a solidification front, depends on the equilibrium of the attractive viscous and repulsive van der Waals forces ($F_\eta = F_\sigma$) [13, 15, 16, 17, 18, 19].

We consider the Rempel-Worster (RW) model [16] to predict the droplet behaviour as the model has been deduced for objects of radius $R < 10^{-4}\,m$. Using this model, we can estimate the characteristic scale of particle size (R_c), at a given solidification velocity V_{sl}, where particles smaller than R_c are rejected and particles larger than R_c are captured by an advancing front. The characteristic particle size R_c, equated by a balance of non-retarded van der Waals and viscous forces ($F_\eta = F_\sigma$), can be given as

$$R_c = \left(\frac{\sigma_{sl} A_{ow}^2}{6^5 \pi^2 \eta^3 V_{sl}^3} \right)^{1/4} \tag{4.1}$$

where σ_{sl} is the ice-water interfacial tension, A_{ow} is the oil-water Hamaker constant, and η is the dynamical viscosity. We obtain a R_c of $9\,\mu m$ with the typical parameter values (see table 4.2) for an object in the ice-water system. Hence, using the RW model we can account for the initial repulsion of the $8\,\mu m$ droplets ($R_1 < R_c$) and an instantaneous engulfment of the $28\,\mu m$ ($R_2 > R_c$) droplets.

Isolated droplets are rejected at the ice-water front when their size is smaller than the critical size ($R_1 < R_c$). In concentrated systems, the droplets being pushed get accumulated ahead of the front and eventually interact with the other droplets, thereby forming a dense object layer (see Fig.4.1). The thickness of the droplet layer grows until a force equilibrium, similar to isolated systems ($F_\eta = F_\sigma$), is reached. Subsequently, we observe a periodic engulfment of droplet mono-layers, when the layer attains a critical thickness of $\approx 80\,\mu m$. A similar observation of particle repulsion-engulfment transition has been reported by the previous studies [32, 47, 48]. More recently, Saint-Michel *et al.* [32] have deduced a modified force equilibrium for multi-particle systems, given as $F_\eta + F_\mu = F_\sigma$. They have suggested that an additional frictional force F_μ is generated by the flow of fluid, through the compact particle layer, toward the ice-water front. In agreement with this model, we believe that the repulsion-trapping of droplets is owing to the fluid flow generated pressure gradient, which pushes the droplets towards the front and favors their engulfment. Thus, we suggest that this additional frictional force F_μ, which grows with the height of the compact layer, results in the periodic engulfment of droplets for a critical layer thickness of $\approx 80\,\mu m$.

Parameters	Nominal value
G $(K \cdot m^{-1})$	1.0×10^{4}
T$_m$ (K)	273.15
η $(Pa \cdot s^{-1})$	1.8×10^{-3}
σ_{sl} $(J \cdot m^{-2})$	3.0×10^{-2}
V_{sl} $(m \cdot s^{-1})$	1.0×10^{-6}
A_{ow} (J)	1.0×10^{-20}

Table 4.2: Typical solidification parameters for an object in front of an ice-water solidification front. σ_{sl} **adapted from Rempel *et al.* [16].**

We will now discuss the droplet-front interactions with 1 $wt.$% solute in solution. The 8 μm (R_1) droplets in the presence of 1 $wt.$% solute are pushed by the growing ice and subsequently organise into close-packed clusters (Fig.4.5B). The droplet clusters formed are rather non-uniform in their distribution and are heterogeneously scattered over the front in the lateral direction ($\vec{y}$). The droplet clusters are eventually engulfed and incorporate in the growing crystal, while getting textured perpendicular ($\vec{x}$) to the solid-liquid front. This spatial distribution is hence opposite to the parallel mono-layers (along $\vec{y}$) obtained in the presence of 0.01 $wt.$% solute concentration (Fig.4.5A). In contrast, the 28 μm (R_2) droplets get engulfed without repulsion (Fig.4.5D), and represent similar behaviour as the corresponding large droplets at 0.01 $wt.$% solute concentration (Fig.4.5C). We thus observe a distinct variation in the droplet spatial distribution only in the presence of small R_1 droplets.

We believe the formation of these heterogeneous clusters is owing to the local destabilization of the ice front and therefore, instigated by the rejected solute segregation. The presence of multiple droplets further enhances the local solute concentration by obstructing the solute diffusion field in the bulk liquid [13, 21, 33, 34]. Highly fluorescent zones in the vicinity of the droplets can be clearly seen at the front (Fig.4.5B,D). These zones are formed owing to the segregation of the fluorescent dye, which is rejected by the growing ice. We expect that the solute, although not fluorescent yet having a similar diffusion coefficient as the dye, segregates in an identical manner at the front. The solute invokes severe constitutional undercooling in the premelted films behind the droplets, thereby inducing a concave curvature of the front [49].

The extensive concave cusping eventually transforms into a *pocket* with the droplet build-up and results in subsequent entrapment of droplets along the crystal growth direction ($\vec{x}$). Such solute enriched *pockets* have also been reported by Chang *et al.* [50] during the directional freezing of biological cells. The premelted films are highly sensitive to the concentration of solute and surround the droplets engulfed by the ice, while the interface heals and rebounds to the horizontal isotherm (T_m). The presence of solute premelted films with thickness of the order $\approx 5\,\mu m$ leads us to believe that the solute plays a dominating role at such high concentration [51]. In the absence of solute effects, premelted films of thickness $\approx 10\,nm$ have been predicted in the particle-front gap by the past studies [15, 16, 17].

Our results depict that an augmentation of solute does not seem to influence the previously predicted value (RW model) of critical radius R_c for droplet engulfment. Similar to the R_1 droplets in the presence of $0.01\,wt.\%$ solute concentration, we report an initial repulsion of the R_1 droplets with $1\,wt.\%$ solute in solution. A few analytical models [20, 21, 33, 34] and numerical simulations [19, 35, 50] studying the object-front interactions in the presence of solute effects have been derived previously. In theory, the magnitude of van der Waals force, responsible for pushing the particle, is regulated by the particle-front gap. The high concentration of segregated solute increases the particle-front gap by constitutional undercooling and hence, significantly reduces the effect of repulsive van der Waals force. This implies that for a given growth rate, smaller objects can be engulfed much more easily in solutions, in contrast to pure melts ($R_c^{solution} < R_c^{pure melt}$). Thus, the theoretical models predict a critical radius (R_c) of magnitude much smaller for binary solutions as compared to the pure melts, which is not what we observe experimentally (i.e. $R_c^{solution} \approx R_c^{pure melt}$). Therefore, we deduce from our experimental observations that $R_1 < R_c < R_2$ is still a valid criterion with

1 $wt.\%$ solute in solution.

4.3.3 Interaction of bimodal objects

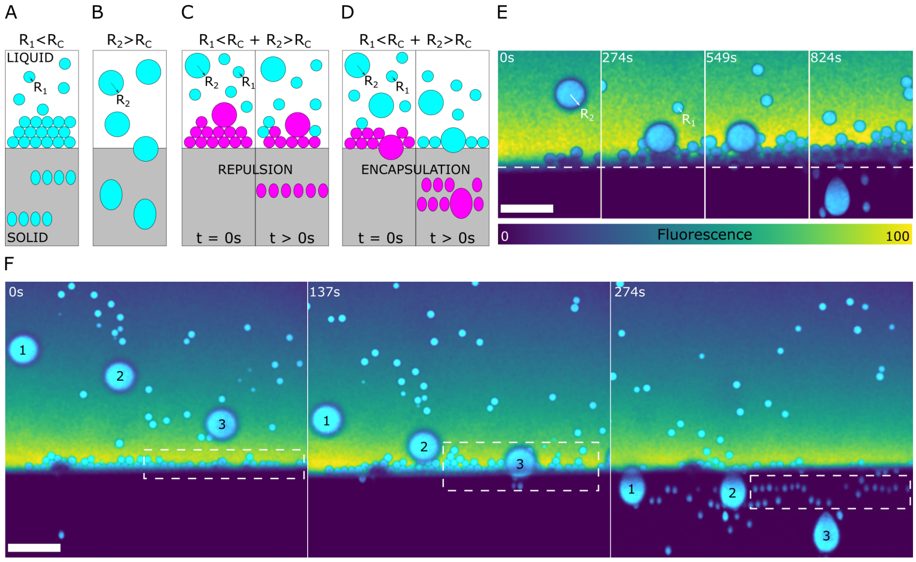

Figure 4.6: Interaction of bimodal oil-in-water emulsion with an advancing ice-water front with 0.01 $wt.\%$ **bulk solute concentration. (A,B) Descriptive sketch representing monodisperse emulsion observation as seen previously with (A)** 8 μm (R_1) **and (B)** 28 μm (R_2) **droplets (C,D) Sketch representing the experimental observations with bimodal emulsion, prepared by mixing the** 8 μm **and** 28 μm **droplets (E,F) Experimental observation of bimodal emulsions depicting (E) Repulsion instigated by droplets $R_1 < R_c$ forming a barrier layer and pushing droplets with $R_2 > R_c$ (F) Engulfment instigated of droplets $R_1 < R_c$ by droplets with $R_2 > R_c$, thereby breaking the compact layer. The droplet 1 is engulfed instantaneously while droplet 2 hits the compact layer and gets repelled before engulfment. Oil is in cyan, water in colormap viridis (fluorescence bar) while ice is in black. Scale bar =**100 μm**.**

We have discussed so far the interaction of monodisperse objects, exhibiting distinct radii (R_1, R_2), with an approaching solid-liquid front. Yet, in many realistic applications, such as fabrication of metal/ceramic matrix composites, we can have a distribution of object sizes. Thus, it is essential in such scenarios to comprehend and predict, the segregation or sorting of particles, during solidification. In light of these uncertainties, we conducted horizontal unidirectional solidification with the same set of droplets (radii $R_1 = 8\,\mu m$ and $R_2 = 28\,\mu m$) composed together, at a solidification velocity V_{sl} of 1 $\mu m \cdot s^{-1}$ and a constant linear temperature gradient G of $10^4\,K \cdot m^{-1}$. To understand the novel scenarios observed, we compare the modes of interactions in bimodal emulsions to the monodisperse regimes at their corresponding solute concentrations $(0.01, 1\,wt.\%)$. We also depict the associated descriptive schemes in absence (Fig.4.6A,B,C,D) and presence (Fig.4.7A,B) of dominating solute effects.

In the presence of $0.01\,wt.\%$ solute (Fig.4.6), we notice two peculiar behaviours of the inter-droplet interaction with the solid-liquid front as follows:

First, as shown in Fig.4.6C,E the small droplets ($R_1 < R_c$) form a compacted layer at the planar front as seen in monodisperse emulsions (Fig.4.6A), which further acts as a barrier layer and provokes the repulsion of a larger droplet (R_2). The latter is pushed ahead for $t \approx 200\,s$ before getting eventually trapped by the growing ice. This suggests that a droplet with a radius greater than the critical value ($R_2 > R_c$) can still be repelled if it does not interact with the solidification front immediately. In contrast, isolated monodisperse large droplets get engulfed instantaneously without undergoing repulsion-trapping, as shown schematically in Fig.4.6B and experimentally in Fig.4.5C.

The second observation (see Fig.4.6D,F) depicts the repulsion-trapping transition of the compacted layer ($R_1 < R_c$), instigated by the presence of 3 large droplets ($R_2 > R_c$), labelled as $1, 2, 3$ in Fig.4.6F. We also notice the relative repulsion of droplet 2 as compared to droplet 1, similar to Fig.4.6C, manifested by the decreasing horizontal distance between $t \approx 0\,s$ and $t \approx 274\,s$. The droplet 2 encounters a compacted layer in the vicinity of the front, while droplet 1 undergoes instant engulfment owing to its large size ($R_2 > R_c$) and an immediate interaction with the solidified crystal. The height (h) of the compacted layer is $\approx 90\,\mu m$ at the instance of the repulsion-trapping transition in the two observations stated above (Fig.4.6E,F). Interestingly, this corresponds closely to the height of $\approx 80\,\mu m$, observed in Fig.4.5A with monodisperse small droplets. The trapping of droplets, for a sufficiently large thickness of the compacted layer, prevents their accumulation and thereby ensures a constant *steady-state* layer thickness [32]. This clearly demonstrates the importance of multiple-particle interactions with a solid-liquid front on the development of a solidified microstructure.

We now investigate the dynamics of bimodal droplet size distribution with $1\,wt.\%$ solute in solution. The large droplet ($R_2 = 28\,\mu m$) as shown in Fig.4.7B,C provokes a concave curvature ($t = 0\,s$), thereby diminishing the crystal growth rate behind it. The *pocket* created in the ice proceeds with the engulfment of the large droplet surrounded by a relatively high concentration of solute ($t = 100\,s$). The

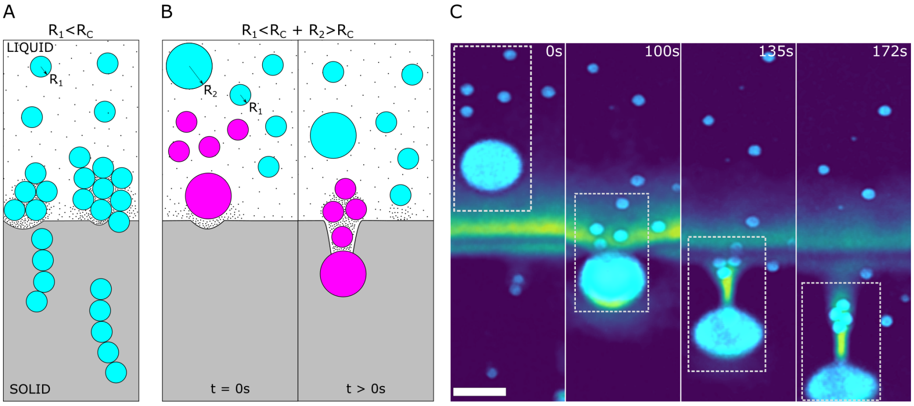

Figure 4.7: Interaction of bimodal oil-in-water emulsion with an advancing ice-water front with $1\,wt.\%$ bulk solute concentration. (A) Model sketch elucidating the previous experimental observations with $8\,\mu m$ monodisperse droplets (R_1) with $1\,wt.\%$ solute in solution (B,C) Concave cusping of the solidification front is induced by the rejected solute segregation in the object-front gap and results in the formation of a solute-rich *pocket*. (B) Schematic depicting the formation of a *pocket* and subsequently induced object clustering with bimodal objects containing R_1+R_2 objects, where $R_1<R_c<R_2$ (C) Experimental observation showing engulfment of $8\,\mu m$ oil droplets in *pockets* initially induced by $28\,\mu m$ droplets. The droplets are far apart in water at $t=0\,s$, get clustered at the fermeture of the solute-rich *pocket* ($t=135\,s$), and at $t=172\,s$ get further close-packed owing to the lateral growth (along $\vec{y}$) of the ice crystals. Oil is in cyan, water in colormap viridis (fluorescence bar) while ice is in black. Scale bar = $100\,\mu m$.

temporary opening, at the solid-liquid front, entices a cluster of smaller droplets ($R_1=8\,\mu m$) behind the large droplet ($t=135\,s$). The droplet cluster, initially isolated, is trapped at the fermeture of the *pocket* and gets textured perpendicular to the front ($\vec{x}$). This orientation is reminiscent of a solidifying monodisperse emulsion depicted schematically in Fig.4.7A. The lateral growth of the ice crystals, transverse to the temperature gradient, pushes the droplets together and results in a close-packed microstructure. Thus, a small increase in the amount of solute added has a drastic impact on the solidification microstructure.

4.3.4 Interaction of polydisperse objects

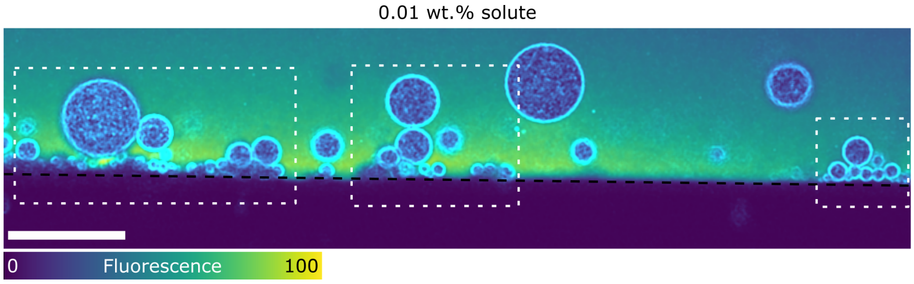

Figure 4.8: Interaction of polydisperse oil-in-water emulsion with an advancing ice-water front at $0.01\ wt.\%$ bulk solute concentration. The droplets with radii smaller than the critical radius ($R_x < R_c$) get pushed by the *steady-state* planar front and lead to the formation of clusters by blocking the arriving droplets ($R_x < R_c < R_y$). Oil is in cyan, water in colormap viridis (fluorescence bar) while ice is in black. Scale bar = $100\,\mu m$.

In the last section, we look at the behaviour of polydisperse oil-in-water emulsions. The low interfacial tension of the oil (propyl benzoate) with water enables us to obtain relatively small polydisperse droplets, varying in size from $5 < R < 30\,\mu m$. We utilize *in situ* cryo-confocal microscopy to acquire 2D and 3D evolution of the microstructure at $V_{sl} = 1\,\mu m \cdot s^{-1}$ and $G = 10^4\,K \cdot m^{-1}$. Previously, we have reported on the monodisperse and bimodal size particle interactions between the growing solid and the droplets, which is considerably different from the nature of interactions between the front and an isolated object. To attain a better understanding of complex (more realistic) systems, we will now investigate the confrontation of polydisperse droplets with an advancing solidification front. The emulsions are prepared with $0.01\ wt.\%$ and $1\ wt.\%$ solute in solution.

When an object interacts with a solid-liquid front it can be engulfed immediately, pushed irreversibly, or repelled for a certain distance and then engulfed [15]. These behaviours are encountered owing to a critical velocity (V_c), inversely proportional to the particle radius ($V_c \propto R^{-\alpha}$), above which an object is engulfed ($V_{sl} > V_c$), while below it the object is pushed by the front ($V_{sl} < V_c$). Conversely, for a given growth rate V_{sl}, there should exist a critical radius R_c, where the objects smaller than the critical size should be pushed and *vice-versa*. Thus, in our experiments with different object sizes one would expect a range of critical velocities or a range of critical radii at the imposed growth rate. Ideally, we expect the engulfment of objects with $R_y > R_c$ and rejection of objects with $R_x < R_c$, where the critical radius is $9\,\mu m$ for our experimental parameters. However, we observe the repulsion of miscellaneous droplets irrespective of their radii ($R_x < R_c < R_y$), as seen in Fig.4.8, in the absence of long-range solute effects. The droplet clusters form at the front with the primary layer occupied by the small droplets ($R_x < R_c$), which further creates a barrier and facilitate the repulsion of relatively larger droplets ($R_y > R_c$).

For planar front solidification in the presence of solute, the previous models [19, 21, 33, 34] deduce a critical engulfment velocity which in most cases is an order below the critical velocity for isolated objects in pure materials. The models suggest either an absence of pushing-engulfment transition, or a destabilisation of the *steady-state* planar front prior to engulfment. In both scenarios, rapid engulfment of the object is suggested as the most favorable outcome, facilitated by an increase in the viscous drag forces. However, the presence of multiple-particle interactions is not incorporated in these models. The experimental evidence are difficult to correlate with owing to varying process parameters and often suggest contradictory results [4, 23, 24, 25]. Körber *et al.* [4] have reported no impact of solute on critical velocity in water-$NaMnO_4$ solution, in contrast to the theoretically expected decrease in V_c (from pure melts) owing to the impurity effects. On the contrary, Sekhar & Trivedi [23] have demonstrated strong impacts of impurity leading to particle trapping in the directional solidification of succinonitrile-acetone system.

In our experiments, we report a pushing-engulfment or repulsion-trapping transition in the presence of dominating solute effects. From Fig.4.9A, we observe the presence of droplet clusters generated both at (inset 1,2,3,4 in Fig.4.9A) and ahead of the front (inset box in Fig.4.9A). The 3D time-lapse evolution depicts the small droplet (inset arrow Fig.4.9A) being pushed by the front for $\approx 400\,s$. Consequently, the droplets (inset 1,2,3,4 in Fig.4.9A) are blocked and form a close-packed cluster, eventually engulfed at $t = 808\,s$. We illustrate this scenario in Fig.4.9B with a model schematic. The morphology of the front does not undergo a transformation in the presence of droplets, as suggested previously [23, 52, 53], and remains as depicted in the absence of objects (Fig.4.4). The formation of the cluster ahead of the front is still not clear but we believe the solute phoretic phenomenon such as diffusiophoresis can be at the genesis of such long-range displacement [38]. Although, we require more experiments to conclude effectively the origin of such close-packed clusters.

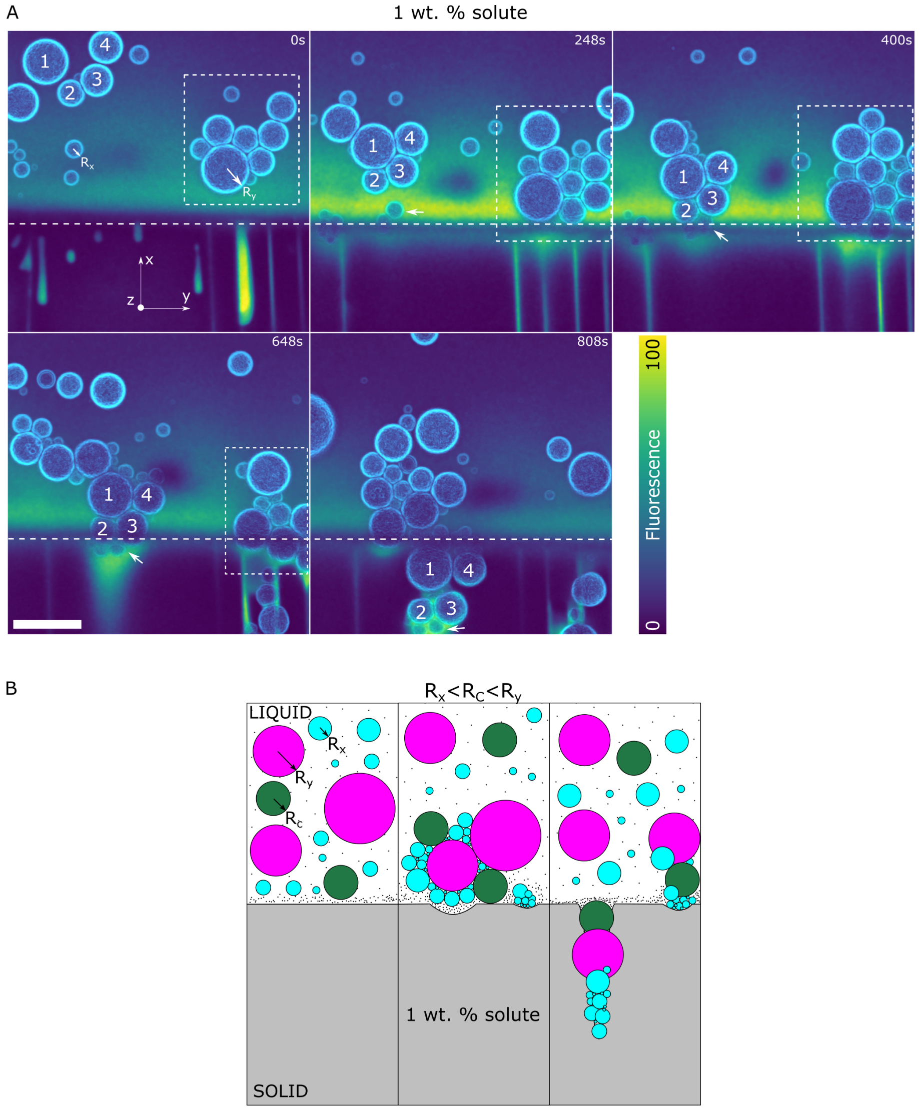

Figure 4.9: Interaction of polydisperse oil-in-water emulsion with an advancing ice-water front at $1\,wt.\%$ bulk solute concentration. (A) Droplets 1,2,3,4 form a cluster at the ice-water front, while the droplets in the insets form a cluster ahead of the front. The agglomerates depict a pushing-engulfment transition with local destabilisation of the ice-water front (B) Schematic depicting the experimental observations in (A), where small droplets ($R_x < R_c$) form a barrier and subsequently form close-packed agglomerates with a combination of droplet sizes ($R_x < R_c < R_y$) before getting captured in the solid. Oil is in cyan, water in colormap viridis (fluorescence bar) while ice is in black. Scale bar = $100\,\mu m$.

4.4 Conclusions

The size, presence of multiple objects, complex front morphology, and high concentration of solute significantly alter the microstructure developed during directional solidification. We performed solidification experiments to study the droplet rearrangement of monodisperse, bimodal, and polydisperse distributions in the solidified matrix. We have tried to highlight the correlations and disparities of multiple-particle regime with previous isolated single object models [16, 19] as well as recent multi-particle models [32], computed both in the absence and presence of solute effects. We have successfully demonstrated in our experiments the distinct behaviour when the size of droplets adheres to the criterion of $R_1 < R_c < R_2$. Furthermore, we have observed no change in critical radius (R_c) in the presence of solute effects contrary to the predictions of the theoretical models. The critical radius (R_c) or critical velocity (V_c) is modified by the presence of inter-droplet interactions. We depict that the presence of multiple objects can lead to the formation of a segregated microstructure, while the initial suspension is homogeneous. We illustrate for the first time a pushing-engulfment or repulsion-trapping transition in the presence of overriding solute effects. We report no change in the morphology of the solidification front owing to the presence of objects in the melt. We suggest that the volume fraction of objects in the melt is an important criterion to be considered for predicting the object distribution in the solidified microstructure. The solidification of controlled oil-in-water emulsions can help us visualize and model a variety of microstructures by utilizing different colonies of droplets in the presence or absence of solute effects.

Acknowledgements

The research leading to these results has received funding from the ANRT and Saint-Gobain through a CIFRE fellowship ($N°$ 2017/0774).

Author contributions

S.D. and C.M. designed and supervised the project, S.D, C.M. and S.T. designed the experiments, S.T. carried out the confocal microscopy, S.T., C.M. and S.D. analyzed the data. All authors discussed the results and implications. S.T., C.M. and S.D. wrote the manuscript.

Conflict of interest

The authors declare no conflict of interest.

Citation

This chapter can be cited as Tyagi, S., Monteux, C. & Deville, S. Multiple objects interacting with a solidification front. Sci Rep 11, 3513 (2021). https://doi.org/10.1038/s41598-021-82713-3

Bibliography

[1] LA Wilen and JG Dash. Frost heave dynamics at a single crystal interface. *Physical Review Letters*, 74(25):5076, 1995.

[2] JS Wettlaufer and M Grae Worster. Premelting dynamics. *Annu. Rev. Fluid Mech.*, 38:427–452, 2006.

[3] VL Bronstein, YA Itkin, and GS Ishkov. Rejection and capture of cells by ice crystals on freezing aqueous solutions. *Journal of Crystal Growth*, 52:345–349, 1981.

[4] C Körber. Phenomena at the advancing ice-liquid interface: solutes, particles and biological cells. *Quarterly reviews of biophysics*, 21:229–298, 1988.

[5] M Shafiur Rahman. *Handbook of food preservation.* CRC press, 2007.

[6] Lifeng Zhang. Nucleation, growth, transport, and entrapment of inclusions during steel casting. *Jom*, 65(9):1138–1144, 2013.

[7] H Li, EA Ghezal, A Nehari, G Alombert-Goget, A Brenier, and K Lebbou. Bubbles defects distribution in sapphire bulk crystals grown by czochralski technique. *Optical Materials*, 35(5):1071–1076, 2013.

[8] OM Bunoiu, Th Duffar, and I Nicoara. Gas bubbles in shaped sapphire. *Progress in crystal growth and characterization of materials*, 56(3-4):123–145, 2010.

[9] Sylvain Deville. Freeze-casting of porous ceramics: a review of current achievements and issues. *Advanced Engineering Materials*, 10(3):155–169, 2008.

[10] D. Shangguan, S. Ahuja, and D. M. Stefanescu. An analytical model for the interaction between an insoluble particle and an advancing solid/liquid interface. *Metallurgical Transactions A*, 23(2):669–680, 1992.

[11] Adrian V. Catalina, Subhayu Sen, Doru M. Stefanescu, and William F. Kaukler. Interaction of porosity with a planar solid/liquid interface. *Metallurgical and Materials Transactions A*, 35(5):1525–1538, 2004.

[12] Arturo E Corte. Vertical migration of particles in front of a moving freezing plane. *Journal of Geophysical Research*, 67(3):1085–1090, 1962.

[13] AA Chernov, DE Temkin, and AM Mel'Nikova. Theory of the capture of solid inclusions during the growth of crystals from the melt. *Sov. Phys. Crystallogr*, 21(4):369–373, 1976.

[14] D. R. Uhlmann, B. Chalmers, and K. A. Jackson. Interaction between particles and a solid-liquid interface. *Journal of Applied Physics*, 35(10):2986–2993, 1964.

[15] R. Asthana and S. N. Tewari. The engulfment of foreign particles by a freezing interface. *Journal of Materials Science*, 28(20):5414–5425, 1993.

[16] A. W. Rempel and M. G. Worster. Particle trapping at an advancing solidification front with interfacial-curvature effects. *Journal of Crystal Growth*, 223(3):420–432, 2001.

[17] Min S. Park, Alexander A. Golovin, and Stephen H. Davis. The encapsulation of particles and bubbles by an advancing solidification front. *Journal of Fluid Mechanics*, 560:415–436, 2006.

[18] A. W. Rempel and M. G. Worster. Interaction between a particle and an advancing solidification front. *Journal of Crystal Growth*, 205(3):427–440, 1999.

[19] Justin C. T. Kao and Alexander A. Golovin. Particle capture in binary solidification. *Journal of Fluid Mechanics*, 625(September 2008):299, 2009.

[20] AA Chernov, DE Temkin, and AM Mel'Nikova. The influence of the thermal conductivity of a macroparticle on its capture by a crystal growing from a melt. *Sov. Phys. Crystallogr*, 22(6):656–658, 1977.

[21] J. K. Kim and P. K. Rohatgi. The effect of the diffusion of solute between the particle and the interface on the particle pushing phenomena. *Acta Materialia*, 46(4):1115–1123, 1998.

[22] AM Zubko, VG Lobanov, and V V_ Nikonova. Reaction of foreign particles with a crystallization front. *Sov. Phys. Crystallogr.*, 18(2):239–241, 1973.

[23] J. A. Sekhar and R. Trivedi. Solidification microstructure evolution in the presence of inert particles. *Materials Science and Engineering A*, 147(1):9–21, 1991.

[24] Stephen J. Mashl, Rolando A. Flores, and Rohit Trivedi. Dynamics of solidification in 2% corn starch-water mixtures: Effect of variations in freezing rate on product homogeneity. *Journal of Food Science*, 61(4):760–765, 1996.

[25] U. Hecht and S. Rex. On the transition from pushing to engulfment during directional solidification of the particle-reinforced aluminum-based metal-matrix composite 2014 + 10 Vol Pct Al2O3. *Metallurgical and Materials Transactions A: Physical Metallurgy and Materials Science*, 28(13):867–874, 1997.

[26] Sylvain Deville. *Freezing colloids: observations, principles, control, and use: applications in materials science, life science, earth science, food science, and engineering*. Springer, 2017.

[27] Yutao Tao, Andrew Yeckel, and Jeffrey J. Derby. Steady-state and dynamic models for particle engulfment during solidification. *Journal of Computational Physics*, 315:238–263, 2016.

[28] Melissa Spannuth, SGJ Mochrie, SSL Peppin, and JS Wettlaufer. Particle-scale structure in frozen colloidal suspensions from small-angle x-ray scattering. *Physical review E*, 83(2):021402, 2011.

[29] Dmytro Dedovets, Cécile Monteux, and Sylvain Deville. A temperature-controlled stage for laser scanning confocal microscopy and case studies in materials science. *Ultramicroscopy*, 195(August):1–11, 2018.

[30] Stephen A Barr and Erik Luijten. Structural properties of materials created through freeze casting. *Acta materialia*, 58(2):709–715, 2010.

[31] Florian Bouville, Eric Maire, and Sylvain Deville. Self-assembly of faceted particles triggered by a moving ice front. *Langmuir*, 30(29):8656–8663, 2014.

[32] Brice Saint-Michel, Marc Georgelin, Sylvain Deville, and Alain Pocheau. Interaction of Multiple Particles with a Solidification Front: From Compacted Particle Layer to Particle Trapping. *Langmuir*, 33(23):5617–5627, 2017.

[33] Jürgen Pötschke and Volker Rogge. On the behaviour of foreign particles at an advancing solid-liquid interface. *Journal of Crystal Growth*, 94(3):726–738, 1989.

[34] R. Sasikumar and T. R. Ramamohan. Distortion of the temperature and solute concentration fields due to the presence of particles at the solidification front-effects on particle pushing. *Acta Metallurgica Et Materialia*, 39(4):517–522, 1991.

[35] Yi Yang, JW Garvin, and HS Udaykumar. Sharp interface numerical simulation of directional solidification of binary alloy in the presence of a ceramic particle. *International journal of heat and mass transfer*, 51(1-2):155–168, 2008.

[36] W. A. Tiller, K. A. Jackson, J. W. Rutter, and B. Chalmers. The redistribution of solute atoms during the solidification of metals. *Acta Metallurgica*, 1(4):428–437, 1953.

[37] Kenji Yoshimura, Takaaki Inada, and Shigeru Koyama. Growth of spherical and cylindrical oxygen bubbles at an ice- water interface. *Crystal Growth and Design*, 8(7):2108–2115, 2008.

[38] Dmytro Dedovets, Cécile Monteux, and Sylvain Deville. Five-dimensional imaging of freezing emulsions with solute effects. *Science*, 360(6386):303–306, 2018.

[39] F López Arbeloa, P Ruiz Ojeda, and I López Arbeloa. Flourescence self-quenching of the molecular forms of rhodamine b in aqueous and ethanolic solutions. *Journal of luminescence*, 44(1-2):105–112, 1989.

[40] Rex Malcolm Chaplin Dawson, Daphne C Elliott, William H Elliott, and Kenneth M Jones. *Data for biochemical research*, volume 3. Clarendon Press, 2002.

[41] Eleanor LV Harris, S Angal, and Simon Roe. *Protein purification applications: a practical approach*, volume 71. IRL press Oxford, 1990.

[42] Moreno Marcellini, Cecile Noirjean, Dmytro Dedovets, Juliette Maria, and Sylvain Deville. Time-Lapse, in Situ Imaging of Ice Crystal Growth Using Confocal Microscopy. *ACS Omega*, 1(5):1019–1026, 2016.

[43] Johannes Schindelin, Ignacio Arganda-Carreras, Erwin Frise, Verena Kaynig, Mark Longair, Tobias Pietzsch, Stephan Preibisch, Curtis Rueden, Stephan Saalfeld, Benjamin Schmid, et al. Fiji: an open-source platform for biological-image analysis. *Nature methods*, 9(7):676, 2012.

[44] Stéfan van der Walt, Johannes L. Schönberger, Juan Nunez-Iglesias, François Boulogne, Joshua D. Warner, Neil Yager, Emmanuelle Gouillart, Tony Yu, and the scikit-image contributors. scikit-image: image processing in Python. *PeerJ*, 2:e453, 6 2014.

[45] W. W. Mullins and R. F. Sekerka. Stability of a planar interface during solidification of a dilute binary alloy. *Journal of Applied Physics*, 35(2):444–451, 1964.

[46] B. Dutta and M. K. Surappa. Directional dendritic solidification of a composite slurry: Part I. Dendrite morphology. *Metallurgical and Materials Transactions A: Physical Metallurgy and Materials Science*, 29(4):1319–1327, 1998.

[47] Anthony M. Anderson and M. Grae Worster. Periodic ice banding in freezing colloidal dispersions. *Langmuir*, 28(48):16512–16523, 2012.

[48] Anthony M. Anderson and M. Grae Worster. Freezing colloidal suspensions: Periodic ice lenses and compaction. *Journal of Fluid Mechanics*, 758:786–808, 2014.

[49] Sidhanth Tyagi, Hélène Huynh, Cécile Monteux, and Sylvain Deville. Objects interacting with solidification fronts: Thermal and solute effects. *Materialia*, 12(April):100802, 2020.

[50] Anthony Chang, Jonathan A. Dantzig, Brian T. Darr, and Allison Hubel. Modeling the interaction of biological cells with a solidifying interface. *Journal of Computational Physics*, 226(2):1808–1829, 2007.

[51] Navaneeth K. Marath and J. S. Wettlaufer. Impurity effects in thermal regelation. *Soft Matter*, 16(25):5886–5891, 2020.

[52] B. Dutta and M. K. Surappa. Directional dendritic solidification of a composite slurry: Part II. Particle distribution. *Metallurgical and Materials Transactions A: Physical Metallurgy and Materials Science*, 29(4):1329–1339, 1998.

[53] L. Hadji. Morphological instability induced by the interaction of a particle with a solid-liquid interface. *European Physical Journal B*, 37(1):85–89, 2004.

Conclusions & Perspectives

We performed this study over a period of three years with the aim of improving our current understanding of the interaction of foreign objects with a moving solidification front. The principal objective was to investigate the mechanisms responsible for the development of a directionally solidified microstructure in the presence of secondary objects with the aide of *in situ* cryo-confocal microscopy. We studied the interaction of isolated hard particles (polymers, ceramics, and metals) and soft objects (droplets and bubbles) with an advancing ice-water interface. To explore the role of solutes, we systematically analysed the interfacial curvature, object dynamics, object shape evolution, and the object spatial distribution, in the presence and absence of solute effects. We then progressed towards more realistic systems by employing a high volume fraction of objects in the liquid melt as compared to the isolated systems. We further compared our experimental observations with the past theoretical models to elucidate the different features and proposed mechanisms for the contrasting phenomena.

We now highlight the main conclusions which can be drawn from each individual study and discuss the opportunities for (hopefully) future work.

Objects interacting with solidification fronts: Thermal conductivity effects

In this study, the primary objective was to analyse the shape of the solidification front experimentally, using objects (soft or hard), having a thermal conductivity mismatch with the liquid melt ($k_p/k_m \neq 1$). The shape of the solidification front is an important parameter defining the magnitude of forces acting on an object and hence, plays a major role on the object-front interactions. The macroscopic geometry of the front is essentially a manifestation of the local isotherms and thus, depends on the uniformity of the temperature field at the solid-liquid interface. The previous studies have investigated the role of object-melt thermal conductivity mismatch but nothing systematic with a complete control over the solidification parameters was performed experimentally. A major part of the previous literature is, therefore, composed of theoretical predictions.

The focus of our study was to explore the solidification front shape over a wide range of thermal conductivity ratio ($0.04 \leq k_p/k_m \leq 35$) by employing polymer, ceramic, metallic rigid particles as well as oil droplets and air bubbles. We first observed and measured the distortion of the ice-water front in the vicinity of the objects with a high spatial resolution owing to our custom cryo-confocal microscopy setup. We noted that for a given curvature (convex or concave), the magnitude of deflection was constant and independent of the nature of the objects. Our observations were consistent with the front curvature predictions of the theoretical model from Park *et al.*, however, the engulfment or repulsion predictions were not in accordance as we noted an engulfment of the objects irrespective of the front curvature.

The next step of our study was to explore the influence of solutes on the front geometry. This was conducted as most real systems consist of solutes (or impurities) and the observation of solute effects *in situ* remains complex. Interestingly, we deduced that the presence of solute segregation between the object and the ice-water interface dominates over the effects of object-melt thermal conductivity mismatch. The solute instigated the formation of a concave front shape (bending away from the objects) with a curvature magnitude considerably higher than that measured in the absence of solute. This has important implications as the nature and magnitude of forces can get modified with the presence of such dominating solute effects.

In the last section, we depicted the ice-water front shape modification for cellular front morphology. We discussed the modification of the distance at which the solute segregation impacts the front geometry in cellular front morphology as compared to the previous planar front investigations. Furthermore, we demonstrated for the first time that objects, with a thermal conductivity less than water, can distort the neighbouring ice crystals post engulfment during directional solidification. Thus, the solidification microstructure, where objects interact with an advancing front, depends on an interplay between the thermal and solute effects.

Moving forward, an important parameter that can be further investigated is the dimensionless surface energy (γ). The role of this parameter, on modifying the front curvature in the vicinity of the objects, can be studied using objects with equal thermal conductivity mismatch (k_p/k_m) with the melt but different radii (R). The nature and magnitude of forces can be explored for objects which have an equal thermal conductivity as the melt ($k_p/k_m = 1$). Here, the shape of the front does not play a role and hence, the force equilibrium can be estimated analytically in the absence of solute effects. The wetting properties of a liquid-particle-solid system can be analysed further as they have not been invoked in the theoretical models. This can be achieved by using hydrophobic and hydrophilic particles, while estimating their critical velocity under similar experimental conditions. The characteristics (thickness, rheology) of premelted films owing to the varying object wetting properties can be interesting to explore.

Solute effects on dynamics and deformation of freezing droplets

This study was performed to comprehend the impact of solute (or impurity) on the interaction of oil droplets with an advancing ice-water interface. We systematically investigated the solute effects at three distinct stages of planar front solidification; droplets in water, droplets at the interface, and droplets captured in ice. The objective was to analyse the modifications instigated by the solute added to the parent liquid, which is subsequently rejected and segregated at the interface, as the ice crystal growth occurs. To perform an in-depth analysis, we used two different droplet sizes and progressively captured the effects of an increasing bulk solute concentration at various growth rates.

Initially, we demonstrated the droplet dynamics far from the ice-water interface i.e. the consequences of the diffusing solute as the front approaches the droplets. We noted that an increasing bulk solute concentration has drastic impacts on the length scale at which it can repel or push the droplets away from the approaching interface. The droplet motion was manifested by a repulsive velocity of 1 $\mu m \cdot s^{-1}$ and initiated at a distance approaching 100 μm for a high solute concentration. The consequences of such long-range effects were reflected by the high interaction-time and instigated droplet displacement of magnitude much greater than the object size. These findings are of interest for studying the development of a material microstructure and predicting the object spatial distribution in alloy solidification. Furthermore, the previous studies have been mostly derived for predicting engulfment or rejection of objects with short-range forces (< 1 μm), while our study provides a complete picture of the mechanisms at play ahead of the solidification front with the quantification of long-range solute (or impurity) effects.

As the solidification front hit the droplets, we further characterised the corresponding *2D* shape deformation observed at the different experimental parameters. We depicted three distinct types of deformation; no elongation, transient elongation at the interface, and permanent elongation in ice. The droplet deformation was found to be strongly dependant on the solute concentration and the droplet size. A high amount of solute instigated solute-enriched premelted films were shown experimentally and believed to be at the origin of the shape recovery mechanism. The evaluation of the object deformation and the surrounding solute environment are topics of research in porosity or void formation during crystal growth and for cryopreservation of food emulsions or biological cells. Our study demonstrated the dynamic nature of object interactions and the evolution of premelted films at the solid-liquid interface. These solidification features remain difficult to visualize experimentally while having drastic impacts on the evolution of the solidification microstructure.

In the last section, we identified the deformation of droplets invoked after their engulfment in the solid ice phase. The use of our custom setup provides a high $2D$ and $3D$ spatial resolution, which permitted us to analyse the droplet behaviour and the surrounding thickness of premelted films at long distances away from the solidification front. The *crushing* phenomenon was suggested to be originating from the meniscus of the ice-water interface. We further looked at the motion of droplets in the solid to investigate the possibility of thermal *regelation*. However, the droplets captured in ice manifested no relative velocity and hence, did not migrate towards the warm side of the underlying temperature gradient. The object migration, premelted films, and particle interaction with the solid phase at low temperatures is investigated especially by geophysicists to understand frost heave, glacier motion, and ice core climate proxies. Thus, we suggest our experimental methodology of using oil-in-water emulsions in the cryo-confocal setup as an analogue for studying such complex phenomena.

In the future, use of a solute exhibiting laser-induced fluorescence can provide further insights into the *in situ* diffusion field. The fluorescence intensity can be acquired and correlated to the local temperature in the vicinity of the solidification front. The diffusion length of such a solute can be compared with the distance at which the objects feel the repulsion to deduce accurately the presence of a thermo-solutal flow (or not). The use of thermo-responsive polymers for which the fluorescence intensity varies with temperature can be envisaged to act as a local temperature probe. The impact of ionic solutes could be investigated to observe additional effects such as the presence of an electrophoresis of colloidal particles. This is interesting as the rejected ions could create *in situ* gradients owing to their differing solubility and migration velocities in the solid-liquid phase. The direction and magnitude of force acting on soft objects instigating their subsequent deformation or those of premelted films can be investigated by the use of stress-responsive polymer mechanophores. These chemical compounds fluoresce under the solicitation of stress and hence, could be helpful in visualizing the crystal growth pressure and direction.

The experimental setup is adapted to study the formation of premelted films at varying solute concentration. Systematic analysis of the premelted film thickness can help in deducing the dominating intermolecular interactions (dispersion or electrostatic) at their origin. The rheology of these premelted films is still largely unknown and we do not know if they behave as Newtonian or non-Newtonian fluids. Measurement of their rheology can be a great stride in the study of object-front solidification systems as well as contribute to the understanding of several geophysical phenomena.

Multiple Objects Interacting with a Solidification Front

We performed this study to try and bridge the gap between isolated object-front interactions and realistic systems where the complexity increases owing to a high concentration of objects. The objective was to elucidate experimentally the development of a real-life microstructure with multiple objects in the presence or absence of solute effects. Most of the previous studies have focused on predicting the behaviour of isolated, hard, spherical, and rigid particles. Much less attention has therefore been paid to particle-particle interactions and the volume fraction of objects dispersed in the liquid. Moreover, the presence of a solute adds to the complexity as it plays a major role on the front morphology. Therefore, we analysed the interaction of multiple oil droplets, acting as a model analogue, with an advancing ice-water interface.

We first demonstrated the interaction of monodisperse oil droplets, and studied the influence of the droplet size and the bulk solute concentration. We depicted the formation of a compact droplet layer and discussed the presence of an additional frictional force similar to that observed in porous media. The force equilibrium modification owing to the particle-particle interactions was invoked and compared to that predicted from the isolated object models. We tried to build upon the previous theoretical studies to explain partly the interaction mechanisms observed in our experiments. We noted a significant impact on the texture of the engulfed droplets with a changing solute concentration and object size.

In the second section, we analysed the interaction of bimodal emulsions, where the droplet radii used in the monodisperse regime were mixed together. We discussed the formation of droplet agglomerates and depicted the repulsion of large droplets owing to the compact layer of smaller droplets being pushed by the solidification front. The addition of a small amount of solute to the bulk liquid resulted in the formation of solute-rich *pockets*. The presence of *pockets* instigated droplet clustering, whereby the oil droplets were forced to close pack into agglomerates.

We finally studied the interaction of polydisperse droplets to imitate the real-life systems with a higher accuracy. We reported the formation of agglomerates at the solidification front in the absence of solute effects, while the clusters were observed well ahead of the front in the presence of solute effects. A pushing-engulfment or repulsion-trapping transition was deduced in contrast to the previous theoretical models, which suggest an instantaneous engulfment of objects in the presence of solute in solution.

Thus, we demonstrated that a small amount of solute in the parent liquid can have a drastic impact on the evolution of the solidification microstructure. Furthermore, we suggested that the evolution of such microstructures, where multiple objects in the presence of solute (or impurity) interact with a front having a complex morphology, remain difficult to predict theoretically.

Further progress in this domain will probably be achieved with the development of robust models that can take into account the solidification behaviour of fronts with complex morphologies while encountering thousands of particles of different sizes. This can be brought forth by numerical modelling techniques such as discrete or finite element modelling. The orientation of particles with arbitrary shapes such as rods or discs could be interesting to visualize when they come in contact with a solidification front. The *in situ* observation of different types of particles (hard or soft) can provide direct observation which can be correlated to improve such predictive models.

Résumé

Nous avons réalisé cette étude sur une période de trois ans dans le but d'améliorer notre compréhension actuelle de l'interaction des objets étrangers avec un front de solidification en mouvement. L'objectif principal était d'étudier les mécanismes responsables du développement d'une microstructure solidifiée directionnellement en présence d'objets secondaires à l'aide de la microscopie cryoconfocale *in situ.* Nous avons étudié l'interaction de particules dures isolées (polymères, céramiques et métaux) et d'objets mous (gouttelettes et bulles) avec une interface glace-eau en progression. Pour explorer le rôle des solutés, nous avons systématiquement analysé la courbure interfaciale, la dynamique des objets, l'évolution de la forme des objets et leur distribution spatiale, en présence et en l'absence d'effets de solutés. Nous avons ensuite progressé vers des systèmes plus réalistes en employant une fraction volumique élevée d'objets dans la masse fondue liquide par rapport aux systèmes isolés. Nous avons ensuite comparé nos observations expérimentales avec les modèles théoriques passés pour élucider les différentes caractéristiques et proposé des mécanismes pour les phénomènes contrastés.

Nous soulignons maintenant les principales conclusions qui peuvent être tirées de chaque étude individuelle et discutons des possibilités de travaux futurs (nous l'espérons).

Objets en interaction avec le front de solidification : Effets de la conductivité thermique

Dans cette étude, l'objectif principal était d'analyser expérimentalement la forme du front de solidification, en utilisant des objets (mous ou durs), ayant un décalage de conductivité thermique avec le liquide en fusion ($k_p/k_m \neq 1$). La forme du front de solidification est un paramètre important qui définit l'ampleur des forces agissant sur un objet et joue donc un rôle majeur dans les interactions entre l'objet et le front. La géométrie du front est essentiellement une manifestation des isothermes locales et dépend donc de l'uniformité du champ de température à l'interface solide-liquide. Les études précédentes ont examiné le rôle de la non-concordance de la conductivité thermique entre l'objet et la liquide, mais rien de systématique avec un contrôle complet des paramètres de solidification n'a été réalisé expérimentalement. Une grande partie de la littérature précédente est donc composée de prédictions théoriques.

L'objectif de notre étude était d'explorer la forme du front de solidification sur une large gamme de rapports de conductivité thermique ($0,04 \leq k_p/k_m \leq 35$) en utilisant des particules polymères, en céramiques, ou métalliques rigides ainsi que des gouttelettes d'huile et des bulles d'air. Nous avons d'abord observé et mesuré la distorsion du front à proximité des objets avec une haute résolution spatiale grâce à notre configuration specifique de microscopie cryo-confocale. Nous avons constaté que pour une courbure donnée (convexe ou concave), l'ampleur de la déflexion était constante et indépendante de la nature de l'objet. Nos observations sont conformes aux prédictions de courbure de l'interface du modèle théorique de Park *et al.*, cependant, les prédictions d'engouffrement ou de répulsion n'étaient pas conformes car nous avons constaté un engouffrement des objets indépendamment de la courbure de l'interface.

L'étape suivante de notre étude a consisté à explorer l'influence des solutés sur la géométrie du front. Cette étude a été menée car la plupart des systèmes réels sont constitués de solutés (ou d'impuretés) et l'observation des effets des solutés *in situ* reste complexe. Il est intéressant de noter que nous avons déduit que la présence d'une ségrégation des solutés entre l'objet et l'interface glace-eau domine sur les effets de la différence de conductivité thermique entre l'objet et la liquid. Le soluté est à l'origine de la formation d'une forme de l'interface concave (qui s'éloigne des objets) avec une amplitude de courbure considérablement plus élevée que celle mesurée en l'absence de soluté. Ceci a des implications importantes car la nature et l'ampleur des forces peuvent être modifiées par la présence d'effets dominants du soluté.

Dans la dernière section, nous avons décrit la modification de la forme du front solid (glace) pour la morphologie du front cellulaire. Nous avons discuté de la modification de la distance à laquelle la ségrégation du soluté affecte la géométrie du front en presence de cellules par rapport aux précédentes études sur le front planaire. De plus, nous avons démontré pour la première fois que les objets, dont la conductivité thermique est inférieure à celle de l'eau, peuvent déformer les cristaux de glace voisins après l'engouffrement lors de la solidification directionnelle. Ainsi, la microstructure de solidification, où les objets interagissent avec un front en progression, dépend d'une interaction entre les effets thermiques et les effets de soluté.

À l'avenir, un paramètre important qui pourrait être étudié plus en profondeur est l'énergie de surface sans dimension (γ). Le rôle de ce paramètre, sur la modification de la courbure de l'interface au voisinage des objets, peut être étudié en utilisant des objets ayant un rapport de conductivité thermique identique par rapport à l'eau (k_p/k_m) mais avec des rayons différents (R). La nature et l'ampleur des forces peuvent être étudiées pour des objets qui ont une conductivité thermique égale à celle de l'eau ($k_p/k_m = 1$). Ici, la forme du front ne joue aucun rôle et donc, l'équilibre des forces peut être estimé analytiquement en l'absence d'effets solutés. Les propriétés de mouillage d'un système liquide-particule-solide peuvent être analysées plus en détail car elles ne sont pas prises en compte dans les modèles théoriques. Cela peut être réalisé en utilisant des particules hydrophobes et hydrophiles, tout en estimant leur vitesse critique dans des conditions expérimentales similaires. Les caractéristiques (épaisseur, rhéologie) des films pré-fondus en raison des différentes propriétés de mouillage des objets peuvent être intéressantes à explorer.

Effets des solutés sur la dynamique et la déformation lors de la congélation des gouttelettes

Cette étude a été réalisée pour comprendre l'impact du soluté (ou de l'impureté) sur l'interaction des gouttelettes d'huile avec une interface glace-eau qui progresse. Nous avons systématiquement étudié les effets du soluté à trois étapes distinctes de la solidification du front planaire : les gouttelettes dans l'eau, les gouttelettes à l'interface et les gouttelettes capturées dans la glace. L'objectif était d'analyser les modifications provoquées par le soluté ajouté au liquide de base, qui est ensuite rejeté et à l'interface, au fur et à mesure de la croissance des cristaux de glace. Pour effectuer une analyse approfondie, nous avons utilisé deux tailles de gouttelettes différentes et avons progressivement capturé les effets d'une concentration croissante de soluté à différents taux de croissance.

Dans un premier temps, nous avons démontré la dynamique des gouttelettes loin de l'interface glace-eau, c'est-à-dire les conséquences de la diffusion du soluté lorsque le front s'approche des gouttelettes. Nous avons noté qu'une concentration croissante de soluté a un impact drastiques sur l'échelle de longueur à laquelle les gouttelettes sont repoussées loin de l'interface qui s'approche. Le mouvement des gouttelettes s'est manifesté par une vitesse de répulsion de 1 $\mu m \cdot s^{-1}$ et a été initié à une distance approchant 100 μm pour une concentration élevée de soluté. Les conséquences de ces effets à longue distance se traduisaient par un temps d'interaction élevé et provoquaient un déplacement des gouttelettes d'une ampleur bien supérieure à la taille de l'objet. Ces résultats sont intéressants pour étudier le développement d'une microstructure de matériau et pour prédire la distribution spatiale des objets lors de la solidification de l'alliage. De plus, les études précédentes ont été principalement dérivées pour la prédiction de l'engouffrement ou du rejet d'objets avec des forces à courte portée ($< 1\ \mu m$), tandis que notre étude fournit une image complète des mécanismes en jeu avant du front de solidification avec la quantification des effets à longue portée des solutés (ou des impuretés).

Lorsque le front de solidification rencontre les gouttelettes, nous avons caractérisé la déformation de forme *2D* correspondante observée aux différents paramètres expérimentaux. Nous avons représenté trois types distincts de déformation : aucun allongement, allongement transitoire à l'interface et allongement permanent dans la glace. La déformation des gouttelettes s'est avérée fortement dépendante de la concentration en soluté et de la taille des gouttelettes. Un film pré-fondu enrichi en soluté a été observé expérimentalement et on pense qu'il est à l'origine du mécanisme de retour à la forme initiale. L'évaluation de la déformation de l'objet et du milieu soluté environnant sont des sujets de recherche sur la porosité pendant la croissance des cristaux et pour la cryopréservation des émulsions alimentaires ou des cellules biologiques. Notre étude a démontré la nature dynamique des interactions entre les objets et l'évolution des films pré-fondus à l'interface solide-liquide. Ces caractéristiques de solidification restent difficiles à visualiser expérimentalement tout en ayant des impacts drastiques sur l'évolution de la microstructure de solidification.

Dans la dernière section, nous avons identifié la déformation des gouttelettes après leur engloutissement dans le solide glace. L'utilisation de notre configuration offre une résolution spatiale élevée en $2D$ et $3D$, ce qui nous a permis d'analyser le comportement des gouttelettes et l'épaisseur environnante des films pré-fondus à de grandes distances du front de solidification. Il a été suggéré que le phénomène d'*écrasement* provenait du ménisque de l'interface glace-eau. Nous avons ensuite examiné le mouvement des gouttelettes dans le solide pour étudier la possibilité d'un effet thermique. Cependant, les gouttelettes capturées dans la glace ne présentaient aucune vitesse relative et, par conséquent, ne migraient pas vers le côté chaud du gradient de température sous-jacent. La migration des objets, les films pré-fondus et l'interaction des particules avec la phase solide à basse température sont étudiés en particulier par les géophysiciens pour comprendre le soulèvement du gel, le mouvement des glaciers et les indicateurs climatiques des noyaux de glace. Ainsi, nous suggérons notre méthodologie expérimentale d'utilisation d'émulsions huile-dans-eau dans le dispositif cryoconfocal comme analogue pour l'étude de phénomènes complexes.

À l'avenir, l'utilisation d'un soluté présentant une fluorescence induite par laser peut fournir des informations supplémentaires sur le champ de diffusion *in situ*. L'intensité de la fluorescence peut être acquise et corrélée à la température locale au voisinage du front de solidification. La longueur de diffusion d'un tel soluté peut être comparée à la distance à laquelle les objets ressentent la répulsion pour déduire avec précision la présence (ou non) d'un flux thermo-solutal. L'utilisation de polymères thermo-sensibles dont l'intensité de la fluorescence varie avec la température peut être envisagée pour servir de sonde de température locale. L'impact des solutés ioniques pourrait être étudié pour observer des effets supplémentaires tels que la présence d'une électrophorèse de particules colloïdales. Ceci est intéressant car les ions rejetés pourraient créer des gradients *in situ* en raison de leur solubilité et de leurs vitesses de migration différentes dans la phase solide-liquide. La direction et l'ampleur de la force agissant sur les objets mous provoquant leur déformation ultérieure ou sur ceux des films pré-fondus peuvent être étudiées par l'utilisation de mécanophores polymères sensibles au stress. Ces composés chimiques sont fluorescents lorsqu'ils sont soumis à un stress et peuvent donc être utiles pour visualiser la pression et la direction de la croissance cristalline.

Le dispositif expérimental est adapté pour étudier la formation de films pré-fondus à différentes concentrations de solutés. L'analyse systématique de l'épaisseur du film pré-fondu peut aider à déduire les interactions intermoléculaires dominantes (dispersion ou électrostatique) à leur origine. La rhéologie de ces films pré-fondus est encore largement inconnue et nous ne savons pas s'ils se comportent comme des fluides newtoniens ou non newtoniens. La mesure de leur rhéologie peut constituer un grand pas en avant dans l'étude des systèmes de solidification du front d'objet et contribuer à la compréhension de plusieurs phénomènes géophysiques.

Des objets multiples qui interagissent avec un front de solidification

Nous avons réalisé cette étude pour essayer de combler le fossé entre les interactions objet isolé et le front et les systèmes réalistes où la complexité augmente en raison d'une forte concentration d'objets. L'objectif était d'élucider expérimentalement le développement d'une microstructure réelle avec de multiples objets en présence ou en l'absence de soluté. La plupart des études précédentes ont porté sur la prédiction du comportement de particules isolées, dures, sphériques et rigides. On s'est donc beaucoup moins intéressé aux interactions entre particules et à la fraction volumique des objets dispersés dans le liquide. De plus, la présence d'un soluté ajoute à la complexité car il joue un rôle majeur sur la morphologie du front. C'est pourquoi nous avons analysé l'interaction de multiples gouttelettes d'huile, agissant comme un modèle analogue, avec une interface glace-eau qui progresse.

Nous avons d'abord démontré l'interaction des gouttelettes d'huile monodispersées, et étudié l'influence de la taille des gouttelettes et de la concentration de soluté. Nous avons décrit la formation d'une couche compacte de gouttelettes et discuté de la présence d'une force de frottement supplémentaire similaire à celle observée dans les milieux poreux. La modification de l'équilibre des forces due aux interactions particules-particules a été invoquée et comparée à celle prédite par les modèles d'objets isolés. Nous avons essayé de nous appuyer sur les études théoriques précédentes pour expliquer en partie les mécanismes d'interaction observés dans nos expériences. Nous avons noté un impact significatif sur la texture des gouttelettes englouties avec une modification de la concentration de soluté et de la taille de l'objet.

Dans la deuxième section, nous avons analysé l'interaction des émulsions bimodales, où les rayons des gouttelettes utilisées dans le régime monodispersé étaient mélangés. Nous avons discuté de la formation d'agglomérats de gouttelettes et avons décrit la répulsion des grosses gouttelettes en raison de la couche compacte de gouttelettes plus petites qui sont poussées par le front de solidification. L'ajout d'une petite quantité de soluté au liquide a entraîné la formation de *poches* riches en soluté. La présence de poches a provoqué l'agglomération des gouttelettes, ce qui a forcé les gouttelettes d'huile à se refermer en agglomérats.

Nous avons finalement étudié l'interaction des gouttelettes polydispersées pour imiter les systèmes réels avec une plus grande précision. Nous avons signalé la formation d'agglomérats au front de solidification en l'absence de soluté, tandis que les amas ont été observés bien avant le front en présence d'effets de soluté. Une transition répulsion-intégration ou répulsion-piégeage a été déduite, contrairement aux modèles théoriques précédents, qui suggèrent un engouffrement instantané des objets en présence de soluté en solution.

Ainsi, nous avons démontré qu'une petite quantité de soluté dans le liquide de base peut avoir un impact drastique sur l'évolution de la microstructure de solidification. En outre, nous avons suggéré que l'évolution de telles microstructures, où de multiples objets en présence de soluté (ou d'impureté) interagissent avec un front ayant une morphologie complexe, reste difficile à prévoir théoriquement.

De nouveaux progrès dans ce domaine seront probablement réalisés avec le développement de modèles robustes qui peuvent prendre en compte le comportement de solidification des fronts ayant des morphologies complexes lors de la rencontre de milliers de particules de tailles différentes. Cela peut être réalisé grâce à des techniques de modélisation numérique telles que la modélisation par éléments discrets ou finis. L'orientation des particules de formes arbitraires telles que des tiges ou des disques pourrait être intéressante à visualiser lorsqu'elles entrent en contact avec un front de solidification. L'observation *in situ* de différents types de particules (rigide ou déformable) peut fournir une observation directe qui peut être corrélée pour améliorer ces modèles prédictifs.

List of Figures

List of Tables

RÉSUMÉ

L'interaction du front de solidification avec des objets (gouttelettes, bulles, particules ou cellules biologiques) est un phénomène courant rencontré dans une multitude de situations, allant des procédés industriels aux événements naturels, tels que la formation de glace de mer, la croissance de monocristaux, la métallurgie, la cryobiologie, l'ingéniérie alimentaire ou la purification de l'eau. Ces processus, pourtant bien identifiés, sont complexes et une compréhension approfondie reste à développer. Les objets (rigide ou déformable) peuvent avoir différents comportements lors de leur rencontre avec un front de solidification en mouvement. Le front peut integrer l'objet, le piégeant dans le cristal en croissance, ou le repousser. Les conséquences de cette interaction ont un impact sur la microstructure finale et déterminent notamment les propriétés structurelles et fonctionnelles du matériau solidifié. En outre, la plupart de ces phénomènes se produisent en présence de solutés (ou d'impuretés), qui peuvent être ségrégés à l'interface lors de la solidification. Dans cette étude, nous analysons l'interaction d'objets sphériques déformable (gouttelettes et bulles) ou de particules rigides avec une front de solidification eau-glace en mouvement. La microscopie cryo-confocale permet une imagerie rapide in situ de la croissance des cristaux de glace, de la phase liquide et de la dynamique des objets qui rencontrent le front de solidification. Nous décrivons l'impact de la concentration des solutés (ou des impuretés) et leur influence sur la géométrie de l'interface, la dynamique des objets et la microstructure de solidification. Nous explorons plusieurs aspects importants des interactions de particules multiples dans des systèmes réalistes et discutons des conséquences de la redistribution des particules par rapport aux systèmes idéaux décrits dans les modèles physiques précédemment développés. Nos résultats montrent comment une concentration croissante de soluté dans le liquide et sa ségrégation lors de la solidification peuvent modifier de façon spectaculaire la nature attendue des interactions entre l'objet et le front et les microstructures de solidification. La congélation des suspensions par microscopie cryo-confocale peut servir d'analogue pour étudier l'interaction in situ d'objets avec une front de solidification en mouvement.

MOTS CLÉS

solidification, interface, soluté, conductivité thermique, microscopie confocale

ABSTRACT

The interaction of solidification fronts with objects (droplets, bubbles, particles, or biological cells) is a common phenomenon encountered in a plethora of situations, ranging from industrial to natural occurrences, such as the formation of sea ice, growth of single crystals, metallurgy, cryobiology, food science, and filtration or water purification. The process, though well-known, is complex and an unambiguous quantification of the mechanisms in situ is yet to be developed. The objects (soft or hard) can have diverse outcomes owing to their confrontation with an advancing solid-liquid interface. The front can engulf the object, trapping it into the growing crystal, or the front can repel the object, pushing it ahead of itself. The consequences of this interaction impacts the final microstructure and hence, determines the structural as well as functional properties of the solidified material. Furthermore, many of these phenomena occur in the presence of solutes (or impurities), which can segregate at the interface during the growth of a solid. In this study, we analyse the interaction of spherical soft objects (droplets and bubbles) and rigid particles with an approaching ice-water interface. Our custom cryo-confocal microscopy setup enables a rapid imaging of the growth of ice crystals, the liquid phase, and the dynamics of objects encountering the solidification front. We depict the impact of solute (or impurity) concentration and their influence on the interface geometry, object dynamics, and the solidified microstructure. We explore several important aspects of multiple particle interactions in realistic systems and discuss the consequences of particle redistribution in comparison to the ideal systems considered by the past physical models. Our results demonstrate how an increasing concentration of solute in the bulk liquid and their subsequent segregation can dramatically alter the predicted nature of object-front interactions and the solidification microstructures. We suggest that the freezing of suspensions using cryo-confocal microscopy may serve as an analogue for studying the in situ interaction of foreign objects with a moving solid-liquid interface.

KEYWORDS

solidification, interfaces, solute, thermal conductivity, confocal microscopy